

Optoelectronic characterization of hot carriers solar cells absorbers

Jean Rodière

▶ **To cite this version:**

Jean Rodière. Optoelectronic characterization of hot carriers solar cells absorbers. Materials Science [cond-mat.mtrl-sci]. Université Pierre et Marie Curie - Paris VI, 2014. English. NNT : 2014PA066703 . tel-01408682

HAL Id: tel-01408682
https://theses.hal.science/tel-01408682

Submitted on 5 Dec 2016

HAL is a multi-disciplinary open access archive for the deposit and dissemination of scientific research documents, whether they are published or not. The documents may come from teaching and research institutions in France or abroad, or from public or private research centers.

L'archive ouverte pluridisciplinaire **HAL**, est destinée au dépôt et à la diffusion de documents scientifiques de niveau recherche, publiés ou non, émanant des établissements d'enseignement et de recherche français ou étrangers, des laboratoires publics ou privés.



École Doctorale Physique et Chimie des Matériaux



Thèse de doctorat

Discipline : Physique des Matériaux

présentée par

Jean Rodière

Optoelectronic characterization of hot carriers solar cells absorbers

---

Soutenue le 29 septembre 2014 devant le jury composé de :

M. Christophe Goupil	ENSICAEN	rapporteur
M. Pierre Renucci	INSA Toulouse	rapporteur
M. Christian Bonhomme	Université Paris V	examinateur
M. Olivier Durand	INSA Rennes	examinateur
M. Jean-François Guillemoles	CNRS	directeur
M. Laurent Lombez	CNRS	encadrant











École Doctorale Physique et Chimie des Matériaux



Thèse de doctorat

Discipline : Physique des Matériaux

présentée par

Jean Rodière

Caractérisation optoélectronique d'absorbeurs pour cellules photovoltaïques à porteurs chauds

---

Soutenue le 29 septembre 2014 devant le jury composé de :

M. Christophe Goupil	ENSICAEN	rapporteur
M. Pierre Renucci	INSA Toulouse	rapporteur
M. Christian Bonhomme	Université Paris V	examinateur
M. Olivier Durand	INSA Rennes	examinateur
M. Jean-François Guillemoles	CNRS	directeur
M. Laurent Lombez	CNRS	encadrant









Institut de Recherche
sur le Développement
de l'Energie Photovoltoïque
6, Quai Watier
78401 Chatou

UPMC
Ecole Doctorale de Physique
et Chimie des Matériaux
4 place Jussieu
75252 Paris Cedex 05

A ma famille, mes proches,
pour leur écoute et leur soutien.

"Écoute, on t'connaît pas, mais laisse
nous t'dire que tu t'prépares
des nuits blanches... des migraines...
des nervous breakdown,
comme on dit de nos jours".
Paul Volfoni, Les tontons flingueurs

"Before I came here I was confused
about this subject. Having listened
to your lecture I am still confused.
But on a higher level"
Enrico Fermi

Acknowledgement

Je tiens à remercier Jean-François Guillemoles, d'une part pour avoir établit ce sujet de thèse "exotique", aux yeux de tous mes collègues, d'autre part de me l'avoir proposé, à la suite de mon stage. Il mène le projet "porteurs chauds" depuis bientôt une décenie avec un pragmatisme et une vision stratégique qui lui sont propres. Je le remercie également de m'avoir fait confiance lors des conférences internationales afin de présenter mes résultats.

Je remercie mon encadrant de thèse, Laurent Lombez, pour sa patience, son ingéniosité, sa diplomatie, son doigté qui, lui permet de manier les lasers mieux que n'importe quel maitre Jedi lambda. Il m'a encouragé sur ce chemin périlleux de la thèse, en suppléant Jean-François à des moments décisifs. Je le remercie également d'avoir pris un temps conséquent à la relecture de ce manuscrit, n'hésitant pas à sacrifier ses soirées, ses week-ends pour des corrections nécéssaires. Alors que le sujet de la thèse ne lui était pas familier, il se l'est approprié, très rapidemment. Telle la brise dissipant la fumée des feux de la Saint-Jean, il effacait les doutes, hypothèses par hypothèses. Au delà des circonstances professionelles, il m'a véhiculé à de nombreuses reprises, d'un point A à un point B, sans hésiter à retourner du point B au point A. A ce moment précis, je m'interroge sur la pertinence de ce remerciement. Néanmoins, à l'aboutissement de cette thèse, je profite de l'instant pour dépasser la pensée cartésienne au profit du surmoi.

Je remercierai évidemment Daniel Lincot pour m'avoir accueilli au sein de son laboratoire. Son enthousiasme n'a aucun égal et celui-ci ne cesse pas de nous surprendre. Je remercie évidemment celui qui fut son homologue EDF, Yves Schlumberger, pour son soutien et la confiance qu'il a su m'accorder lors de la présentation de mes résultats devant les directeurs de la R&D d'EDF et de Thalès. Matthieu Versavel l'a

remplacé et m'a aiguillé dans la définition de mon projet professionel, grâce à sa sincérité et son efficacité. Pour cela, je l'en remercie grandement.
Je remercie Olivier Durand, mon interlocuteur privilégié au sein du laboratoire FOTON qui m'a fourni des échantillons à la pelle. Son humilité et ses compétences ont permis d'établir un dialogue agréable et nourricier. Dans ce même cadre, je remercie Philippe Christol et son équipe de l'IES pour m'avoir reçu sous un soleil de janvier que je ne s'aurai oublié. Notre collaboration s'est interrompu devant les excellentes performances d'échantillons à base d'InGaAsP de FOTON, cependant je retiens leur savoir faire, leur compréhension et leur accueil.
Je tiens également à remercier Prs Conibeer, Sugiyama, Ekins-Daukes pour m'avoir accordé un peu de leur temps précieux. Leur commentaires et leurs questions durant les conférences internationales n'ont cessé de me surprendre par leur qualité.
Au jour le jour, je veux remercier mes collègues de l'équipe "caractérisation" pour nos nombreuses discussions et ergotages scientifiques. Socrate en serais fier. Tout d'abord, dans l'équipe, je veux remercier Pierre qui est "bien au-delà" d'un simple collègue. Nos aventures atteignirent leur apogée lors de cette conférence appelé EMRS. Que le marbre de Strasbourg en témoigne ! Si un porteur chaud doit se détendre, c'est avec toi qui le ferait. Merci d'avoir écouté mes griefs aussi peu nombreux fussent-ils. Ensuite, il y a Amaury dixit "Le Breton". Il m'a beaucoup aidé dans la prise en main de cette appareil à tout faire : l'hyperspectral hyperbon hyperprécis hyperrapide. Y perd pas grand chose avec l'hyperspectral. Puis viens François Gibelli dixit l'alpiniste, je le remercie de m'avoir initié à cette nouvelle langue : le latex me va comme un gant. Merci pour son humilité, sa bonne humeur et ses calculs pas renaux. Je remercie également Gilbert dixit Gilbert pour sa gentillesse, sa motivation perpetuelle, ses encouragements. Ces derniers se traduisent par de récurrentes petite tapes. Quiquonque normalement constitué prendrait ceux-ci pour des crochets du droit. A la salle de muscu, je garde en mémoire l'image de cette barre de "faire à tout fer" pliant sous les 160 kg qu'il soulevait. Il ajoutait : "faut faire attention, ce n'est pas une barre olympique". Aussi avisé que le conseil fusse, je ne me senti guère concerné par le propos. Dans l'équipe carac, je veux remercier Myriam d'avoir relu ma thèse comme s'il s'agissait du dernier roman de Marc Levy. Sa solicitude mêlé de son serieux furent très appréciables. Enfin, bien qu'il ne fasse pas parti de l'équipe carac, je remercie Hugo pour les discussions chaudes que nous entretinrent alors que j'étais encore au batîment K. Est-ce qu'Hugo c'est un phonon ? Après trois ans de thèse, les gens s'interrogent toujours. A ta soutenance, pense à expliquer la différence entre un phonon et un faux nom. Sinon, on risque de t'interroger sur la nature des faux noms acoustiques. Avant d'entamer mes anté-anté-anté-penultièmmes remer-

ciements, je tiens à remercier Claudia d'avoir relu ma thèse entièrement. J'imagine qu'elle restera à jamais la seule personne non scientifique l'ayant fait.
Je tiens à remercier également tous les membres du laboratoires que j'ai pu cotôyer. Bien sur, je n'oublierai pas ma famille et mes proches pour tout leur soutien, leur sollicitude et leur compréhension dans cette épisode de vie.

List of Symbols & Acronyms

$\Delta\mu$	quasi-Fermi levels splitting
HI	hyperspectral imager
PL	photoluminescence
EL	electroluminescence
HCSC	hot carrier solar cells
HC	hot carrier
ESC	energy selective contacts
MQWs	multi-quantum wells
QWs	quantum wells
QD	quantum dot
Q1.6	$In_{0.78}Ga_{0.22}As_{0.81}P_{0.19}$
Q1.4	$In_{0.66}Ga_{0.34}As_{0.733}P_{0.267}$
Q1.18	$In_{0.8}Ga_{0.2}As_{0.44}P_{0.56}$
T0.34	$In_{0.66}Ga_{0.34}As$
T0.47	$In_{0.53}Ga_{0.47}As$
EQE	external quantum efficiency
GLM	generalized linear model
PV	photovoltaic
TQ	thermodynamic quantities

Contents

List of Symbols & Acronyms **13**

List of Tables **19**

List of Figures **21**

Introduction **27**

1 Hot carrier solar cells **29**

1.1 Context of the study 29

1.1.1 Photovoltaic position in Energy field 29

1.1.2 Future Photovoltaic technologies 31

Shockley-Queisser limit 31

Third generation photovoltaics 35

1.2 Introduction of hot carrier solar cell concept 37

1.2.1 General presentation of the device 37

The concept: Ross and Nozik's thought 37

Würfel's analysis 37

Definition of standard parameters 38

1.2.2 Thermalisation rate parameter 39

Origin of thermalisation 39

Experimental evidence of hot carriers 40

Introduction of the thermalisation rate parameter 42

1.2.3 Energy selective contacts 42

energy selective contacts (ESC) role 42

ESC: in the making . . . 43
1.2.4 Theoretical performances . . . 45
Interactions parameters . . . 45
1.2.5 Need to qualify performances of the absorber through standard quantities determination . . . 47

2 Hot carrier solar cells characterization tools 51
2.1 Photoluminescence . . . 51
2.1.1 Generalized Planck's law . . . 51
2.1.2 Thermodynamical probed values . . . 53
Lattice temperature . . . 53
Carrier temperature . . . 53
Quasi-Fermi levels splitting . . . 54
2.1.3 Photoluminescence experimental techniques . . . 55
Pump-and-probe absorption . . . 55
Streak camera . . . 55
Up-conversion gate . . . 55
2.2 Experimental methods . . . 56
2.2.1 Steady-state photoluminescence set-ups . . . 56
Relevant conditions for solar cells . . . 56
Set-ups . . . 57
2.2.2 Description of full calibration and measurement method . . . 57
2.2.3 Development of a method to compare hyperspectral imager (HI) and confocal . . . 58
Accurate local values . . . 60
Spatial average values . . . 60
Confocal collection area determination thanks to carrier temperature . . . 61
quasi-Fermi levels splitting ($\Delta\mu$) calibration of confocal . . . 64
2.3 Samples description . . . 66
2.3.1 General sample diagramm . . . 66
Claddings . . . 66
Extended barriers . . . 67
2.3.2 InGaAsP multi-quantum wells . . . 67
2.3.3 Samples parameters and performances . . . 67
Samples presentation . . . 68
Sample performances . . . 68
Statistical method . . . 69

Model and key parameters 70
Thickness influence on thermalisation rate 72
2.3.4 Detailed description of the bipolar device 73
2.4 Absorbance simulation and measurement 75
2.4.1 Modelling optical indices 75
n and k modelling 75
2.4.2 Simulated absorbance properties 77
2.4.3 Absorbance calculation 78
2.4.4 Measurement of external quantum efficiency (EQE) and its effect on photoluminescence (PL) spectra 80
Simulated and experimental external quantum efficiency . . . 80
Correlation between PL spectra and absorbance 81
2.5 Hot carrier device simulation 84
2.5.1 Introduction to numerical balance equations software 84
Principle of the software 84
Architecture of the software 84

3 Quantitative optical measurement of hc effect 87
3.1 Evidence of performance under-estimation by local measurements . . 87
3.1.1 Probing absolute PL map 87
3.1.2 Local Temperature 91
3.1.3 Local $\Delta\mu$ 94
3.1.4 Thermoelectric effect in hot carrier solar cells (HCSC) 100
Photo-Seebeck coefficient calculation 100
Photo-Seebeck coefficient description 102
Getting the photo-Seebeck coefficient 103
3.2 Optical evidence of HCSC regime by averaged measurements 106
3.2.1 Probing emission and lattice temperature by confocal set-up . 106
Carriers in barrier are thermalised 106
3.2.2 Probing average of $\Delta\mu$ by confocal set-up 108
Getting absolute $\Delta\mu$ in confocal mode 108
Hot carrier solar cell regime by optical probing 112
3.3 Simulation of thermodynamic quantities in device 2757 112
3.3.1 Input parameters 114
3.3.2 Results of PL under different absorbed powers 115

4 Optoelectronic characterisations **119**
4.1 Controlling tq through pl under bias 119
4.1.1 Current-Voltage (IV) curves 120
4.1.2 Comparison between electrical open circuit and optical $\Delta\mu$ . . 123
4.1.3 Temperature of emission under electrical bias 126
4.1.4 $\Delta\mu$ under electrical bias 126
4.2 Simulation of tq under electrical bias 131
4.2.1 Comparison between simulated and experimental temperatures 131
4.2.2 Comparison between simulated and experimental $\Delta\mu$ 133

Bibliography **137**

A Appendix **147**

B Appendix **151**

C Appendix **153**

List of Tables

1.1 Table of the third generation photovoltaics concept for different strategies and their impact on the particle number extracted from [1] . . . 35

2.1 Parameters of the samples . . . 68

2.2 Table of sample performances through thermalisation rate and temperature of emission in quantum wells (QWs). Key parameters of performances are also added. They were identify thanks to the statistical method. . . . 69

2.3 Table gathering the key material parameters found by generalized linear model (GLM) fitting; their related coefficient (name, sign and influence) are added. . . . 71

List of Figures

1.1 The global PV module price learning curve for c-Si and CdTe modules from 1979 to 2015 from [2]. 30

1.2 Net power generation capacities added in Europe (EU28) between 2000 and 2013 from [3]. 31

1.3 Module efficiency as a function of the manufacturing costs in arbitrary unit for different module technologies, from [4] 32

1.4 Module and system prices (US dollars) on residential and commercial installations in US from [5]. 32

1.5 photovoltaic (PV) installation costs in $\$/W_p$ of ground mounted and rooftop in the left. In the right, the balance of system is detailed according to both installation types, from [2]. Reported costs of conventional PV in 2010, USA. 33

1.6 Power ratio of the different losses in a photovoltaic solar cell as a function of the energy band gap, [6] 34

1.7 Conversion efficiency limits as a function of the number of jonction under AM1.5 irradiation extracted from [7] 36

1.8 Schematic of a HCSC extracted from [8] 38

1.9 Time evolution of carrier distribution after pulse solar excitation. Schematic extracted from [1]. 40

1.10 Schematic structure employed by König *et al.* extracted from [9] which was used in order to show extraction of hot carriers generated in the bulk Si by a pulse laser excitation at different wavelength and extracted through resonant quantum dot (QD)s of Si to Al contacts . 43

1.11 Schematic energy band diagram of a resonant tunnelling barrier extracted from [10]. 44
1.12 Schematic of a HCSC with semi-selective contacts extracted from [8] (a). Iso-efficiency curves as a function of extraction energy and contact selectivity for full concentration with a 1 eV energy band gap (b), from [8]. 45
1.13 Fraction of the incident power that is converted (red), not absorbed (black) and lost in the selective contacts under full concentration and no thermalisation extracted from [8] 46
1.14 Fraction of the incident power that is converted with as a function of the carrier density for 1 (green) and 1000 suns (blue) illumination extracted from [1]. Eg=0.7 eV, Eext=1.54-1.58 eV no thermalisation . 47
1.15 Conversion efficiency as function of the extraction energy for a 1eV band gap absorber under full concentration for different energy selectivity width extracted from [8] 48
1.16 Conversion efficiency as a function of the contact conductance for different energy selective width. The extraction energy was optimised for each conductance and selectivity. Eg=1eV, concentration=46000 suns 48

2.1 Example of a PL spectrum (red squares) which is the product of absorbance α (blue squares) the black body spectrum Φ_{BB} (black squares), and an intensity term $\exp(\Delta\mu/k_bT)$ described by Eq. (2.3). The arrows represents the influence of the thermodynamic parameters on the PL spectrum. 54
2.2 Schematic of the confocal (a) and hyperspectral imager (b) set-ups . . 59
2.3 Integration procedure to get accurate local values (a) and spatial average values (b) of the PL spectrum as a function of radius 61
2.4 Determination of the collection area of confocal set-up based on the comparison between confocal (black squares) and HI (green dotted lines). The figure represents the temperatures of emission as a function of the absorbed power. Remark that for each absorbed power, one data acquisition was made. Then, the data were integrated spatially. Legend indicates the radius of integration area, in units of illumination radius, which grows from 0 to 3.8 R_spot (black to green). Hemisphere image of the illumination spot and collection area in the bottom left inset 63
2.5 Comparison between electroluminescence (EL) and PL measurement . 64

2.6 $\Delta\mu/T$ as a function of the absorbed powers plotted for recalibrated confocal (black squares) and HI (red dots) data thanks to the relation Eq. (2.11) and a -0.10185 constant 65

2.7 Simplified band diagram structure of samples studied 67

2.8 GLM fit of thermalisation rate where the probed quantities are represented as a function of the modelled one. Dots represents the probed value whereas red line correspond to the fit. Blue dash lines are the mean probed quantity and red dashed lines are the confidence interval 71

2.9 Conversion efficiency as a function of the absorber thickness for a flat absorber (filled circles) and in the Lambertian limit (empty circles) under a 10 000 times concentrated AM1.5D solar spectrum. The efficiency is found to be monotonously decreasing with the absorber thickness in the case of a flat absorber, but an optimal thickness of about 50 nm is observed, giving a maximal efficiency of 50%, in the Lambertian limit. The efficiencies obtained with the dielectric grating (filled star) and with the plasmonic grating (empty star) are also reported. The thermalisation coefficient Q is taken 10 $W/K/cm^2$ for a 200-nm-thick absorber. Figure extracted from [11] 72

2.10 Simplified band diagramm of sample 2757 73

2.11 Layers representation of the sample 2757 associated to doping, thickness and band gap from top to bottom 74

2.12 Schematic of PL under electrical bias experiment 74

2.13 Real and imaginary part of the refractive indices as a function of photon energy for different $In_{1-x}Ga_xAs_yP_{1-y}$ compositions 76

2.14 multi-quantum wells (MQWs) transitions energy of sample 2757 . . . 78

2.15 Absorbance of the intrinsic part of the sample 2757 79

2.16 EQE of the sample 2757 80

2.17 Simulated and experimental EQE as a function of the incident photon energy (eV) on sample 2757. 81

2.18 Normalized PL and fonction of PL 82

2.19 $\Delta\mu$ as a function of the photon energy extracted from Eq. (2.5). $\Delta\mu$ was calculated according to the emission temperature of the QWs from 0.72 to 0.95 eV and to according to the emission temperature of the barrier from 0.95 eV to the end. The dashed lines represents the intervals on which each $\Delta\mu$ were extracted. 83

3.1 Thermodynamic quantities extracted from spatially resolved PL spectra. Maps (left) and profiles at different powers (right) of spectrally integrated PL intensity (a,b), temperature of emission (c,d) and $\Delta\mu$ (e,f). 88

3.2 (a) Spectrally integrated PL at barycentre of the maps as a function of the absorbed power. (b) Normalized spectrally integrated PL along X direction at Y=Barycenter of the left corresponding maps for different illumination powers (from green to black). Inset: Full width at 50% integral of PL peaks as a function of the absorbed powers (black dots). 90

3.3 Radiative emitted power (a) and integrated PL (b) as a function of the local absorbed power calculated from Eq. (3.6) (b). Sample 2757, $\lambda_{spot} = 975\,nm$. 91

3.4 Temperature of emission of the sample 2757 for different absorbed powers from hyperspectral data 92

3.5 Local measurement of the thermalisation rate deduced from a absorbed power map based on integrated PL map and the corresponding local temperature map of emission under 22000 suns 93

3.6 Conversion efficiency as a function of the thermalisation rate coefficient, with a 1 eV band gap absorber and perfectly selective contacts, with concentration ranging from 100 to 46000 suns, from [8]. 95

3.7 Scatter diagramm of $\Delta\mu$ in the QWs as a function of the local absorbed power (black dots). Data were extracted from $\Delta\mu$ and local absorbed power maps acquired by HI set-up. Red line is the radiative open circuit voltage at 300 K for a 0.78 eV absorber (black straight line). Sample 2757, $\lambda_{spot} = 975\,nm$. 96

3.8 Output voltage extracted from (3.8), $\Delta\mu$, T_{e-h}, and the barrier energy band gap 1.05 eV in the case of isentropic ESC 98

3.9 Potential efficiency limit of the sample 2757 considering perfect selective contacts and taking into account the lateral diffusion (black dots). Theoretical limit of a classical solar cell with a 0.78 eV band gap (black line) 99

3.10 Scatter diagram of the norm of $\Delta\mu$ gradient as a function of the norm of the temperature of emission measured for a mean power of 22000 suns (a) and for 7000 suns (b) on sample 2757, (black dots). A linear fit is also plotted (red line) with the intercept fixed at 0. 104

3.11 Photo-Seebeck coefficient as a function of temperature of emission extracted from Eq. (3.27). Sample 2757, mean absorbed power of 22000 suns, $\lambda = 975\,nm$. 105

3.12 Emission temperature of the MQWs probed by confocal (black squares), by HI (red dots) and emission temperature of the MQWs barrier probed by confocal (green triangles) for different mean absorbed powers on the sample 2757 under laser excitation at 975 nm 107

3.13 $\Delta\mu$ obtain by HI set-up for different spatial integration (green dotted lines) and the recalibrated confocal measurement (black square). Remark that for each absorbed power, one HI data acquisition was made. Then, the data were integrated spatially. Legend indicates the radius of integration area, in units of illumination radius, which grows from 0 to 3.8 R_spot (black to green) 109

3.14 Intensity of PL of QWs and barriers peak normalized by their maximum as function of absorbed power (a). Ratio of MQWs over barrier PL intensity peak (b) 111

3.15 $\Delta\mu$ as a function of the absorbed powers in the barriers (squares black and blue, up) and the wells (squares black and blue, bottom) averaged on different collection area by confocal. The collection area is either the confocal one of a radius equal to 2.5 times the illumination radius ($R = 2.5R_{spot}$, black) or equal to the illumination area ($R = R_{spot}$, blue). $\Delta\mu$ measured by HI are also plotted for the two different collection radius (triangles). Sample 2757, $\lambda = 975nm$. 113

3.16 Energy diagram of the simulated device 2757 115

3.17 Simulation of temperature of emission (a), $\Delta\mu$ (b), V_{oc} (c) as a function of the absorbed power for various thermalisation rate Q=1 (black), 10 (dark green), 100 $W/K/cm^2$ (light green). Open circuit voltage is also plotted as a function of the absorbed power for different extraction energy (d) $E_{ext} = 0.78$ (black), $E_{ext} = 1.05$ (dark green), $E_{ext} = 1.35eV$ (light green). 117

4.1 IV characteristics for different absorbed powers. $\lambda = 975nm$, sample 2757 120

4.2 Short circuit current as a function of the total absorbed powers (top) for different ratio of R_d/R_{spot} ($R_d/R_{spot} = 27$ green,$R_d/R_{spot} = 34$ black). Open circuit voltage as a function of the corresponding short circuit current (Bottom). Sample 2757, $\lambda = 975nm$. 121

4.3 Open circuit voltage probed from average $\Delta\mu$ (green) for different absorbed powers. A linear fit of the average $\Delta\mu$ with the logarithm of the radius is made to get the open circuit voltage 124
4.4 Open circuit voltage measured optically and electrically. Optical open circuit voltage is extracted from from averaged $\Delta\mu$ over an effective radius see Fig. 4.3, (black square). Electrically probed open circuit voltage are measured with a centred illumination (red dots) and with an illumination close to the contact (blue star). $\lambda = 975nm$, $P_{abs} = 22000suns$, sample 2757. 125
4.5 Temperature of emission of the QWs as a function of the applied bias (a) or the current (b) for different illumination powers. Derivative of emission temperature in the wells as a function of the current (c).$\lambda = 975nm$, sample 2757 127
4.6 $\Delta\mu$ of the QWs as a function of the applied bias for different illumination powers (a). Corresponding current as function of $\Delta\mu$ of the QWs (b). $\Delta\mu$ of the QWs and the barriers as a function of the applied bias for different illumination powers (c). Corresponding current as function of $\Delta\mu$ of the barriers (d). $\lambda = 975\,nm$, sample 2757. 129
4.7 Internal conversion efficiency as a function of $\Delta\mu$ of the barriers as the absorbed powers increases (from black to green. These curves are obtained from optical measurements on confocal set-up calibrated thanks to the hyperspectral. 130
4.8 Simulated (a,c) and experimental (b,d) temperatures of emission and $\Delta\mu$ of the QWs as a function of the electrical bias for different absorbed powers. Sample 2757, excitation wavelength 975 nm. 132

A.1 Geometric representation of the emitted PL signal from material n2 to the air n1 148
A.2 Internal radiative efficiency of the sample 2757 as function of absorbed powers 149

B.1 Local temperature of emission 152

Introduction

On Earth, solar energy is an abundant form of potential energy sources. This sentence is definitely an euphemism, as the annual deposit of solar power represents 100000 TWh [12]. In half an hour, the Earth collects the world's entire annual energy production. The technology of photovoltaics aims to convert the latter abundant resources in electricity; its growth was evidenced through Germany's most recent sunnier day (9 June 2014), where it provided 50.6% of the country's total electricity production in a day [13]. The conversion efficiencies of the current industrial photovoltaic technologies range between 10% and 30% [14]. Nevertheless, recent and continuous efforts made by the R&D photovoltaic community induced the emergence of new solar cell concepts such as multi-junctions and hot carrier solar cells. Multi-junction-based solar cells are already being industrialised (reaching 35.5% of conversion efficiency, [15]), whereas hot carrier solar cells are still at a research phase. Theoretical calculations demonstrate that these two concepts are actually capable of providing a conversion efficiency limit of 87% [16].

The elegant physical concept of hot carrier solar cell was introduced in 1982 by Ross and Nozik and immediately after, simulating their performances was of main interest, in order to understand their concept potential [17]. Nowadays, even after three decades, there is not only a lack of hot carrier solar cell experimental characterisation but also the requirement of the use of relevant conditions for operating this kind of solar cells.

First and foremost, in chapter 1, new concepts in solar cell photovoltaics will be positioned in a global context, which will begin from the introduction of the

renewable solar resource to the current photovoltaic solar cell limitations. Then, the photovoltaic hot carrier solar cell concept will be introduced starting from these limitations. At the end, the concept itself will be approached through the identification of key parameters.

Later on, chapter 2 will demonstrate that the hot carrier solar cell light absorber may be described by its light re-emission spectrum, a physical phenomenon called photoluminescence emission of radiation. The phenomenon is described by thermodynamic quantities, which are fundamentally governing the solar cell performance. Not only the characterisation technique based on steady-state photoluminescence will be detailed but also the absorber based on quantum wells. Their preliminary performances will be studied. Finally, the unique hot carrier characterisation method will be developed.

Moving on to the third chapter, the originality of this thesis shall emerge through both the sample's photovoltaic performances and the innovative characterisation methodology of hot carrier solar cells. The hot carriers themselves will be spatially resolved, as well as the performances of the absorber. The characterisation method will be extended to the quantification of a key thermoelectric parameter. Then, local characterisation will highlight the fact that the absorber thermalisation is no longer the limiting parameter in the development of a hot carrier solar cell. Arriving to the contribution of this dissertation's work to the development of the understanding of hot carrier solar cell operation: we demonstrated the achievement of a gain in the electronic potential by hot carriers within the investigated absorber.

Chapter 4 shall finalize this study by establishing connections and plausible links between optical and electronic measurements. In other words, classical photovoltaic opto-electronic measurements will be performed in order to demonstrate hot carrier solar cell are getting closer from the proof of concept. The results will be discussed by preliminary simulations of thermodynamic quantities.

CHAPTER 1

Hot carrier solar cells

1.1 Context of the study

1.1.1 Photovoltaic position in Energy field

The second thermodynamic principle says that each energy conversion is irreversible. It means one must minimize the number of energy transformation steps in order to increase the total conversion efficiency. photovoltaic is by definition the direct conversion of solar radiation into electricity. Therefore, if one classifies the electricity production types by theoretical final conversion efficiencies, the PV would be the best, and more generally renewable energies are better than fossils one. Even though wind-power, biomass, hydro-power, coal, oil, gas result all from solar radiation (in fact wave power is an exception), the transformation steps distinguished fossils and renewable energies: the more conversion transformation steps the longer it renewals. Therefore, taking the Carnot's principle into account one can wonder why fossil energies are used. Their predominance is due to geographical concentration, easy access and storage. Indeed, fossil energies compensate their low conversion efficiencies by their higher accumulation period (billions of years). However, oil and gas production peaks were already reached. Consequently, fossil energies costs are bound to increase in the mid and long run owing to lower availability, higher extraction costs and market pressure. Renewable energies industrial development did not start due to the increase of fossil energies costs but firstly by climate constraints, which lead to Kyoto commitments. Secondly, renewable energies production capaci-

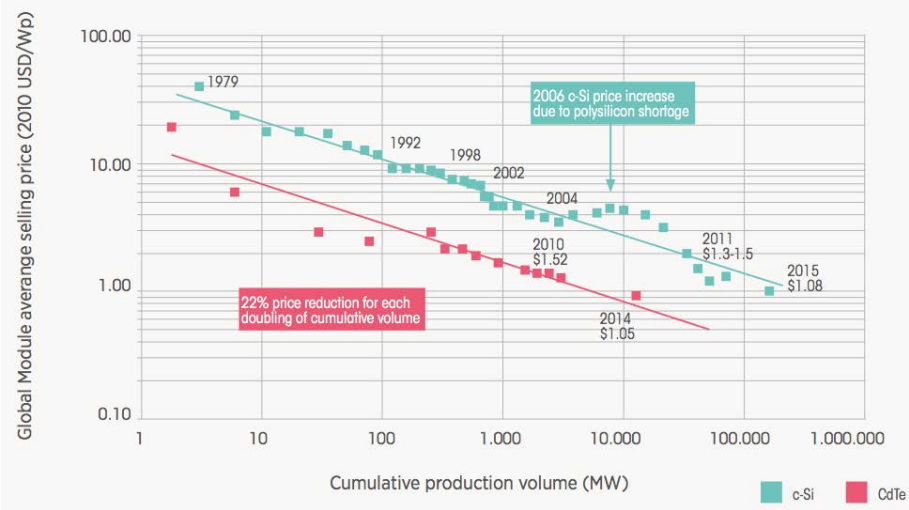


Figure 1.1 – The global PV module price learning curve for c-Si and CdTe modules from 1979 to 2015 from [2].

ties increased and lowered the costs. This can be seen in the industrial development of PV through the learning curves of Si and CdTe PV technologies Fig. 1.1.

As a result, the net electricity power generation capacities added between 2000 and 2013 in Europe (EU28) was dominated by wind and PV, see Fig. 1.2 from [3]. Thus, for the first time, the electrical energy production from all renewable energies was more important (28%) than each independent fossil energies in Europe in 2013 [18].

Contrary to high geographical concentration of fossil energies, solar energy flux is dispersed on the Earth surface, however it represents already 1300 $kWh/year/m^2$ according to [19] at Paris latitude. If one considers the current french thermal building regulation (RT2012), which says the buildings should emit lower than 50 $kWh/year/m^2$ of primary energy (energy before transformation), PV can have a significant contribution.

The beginning of PV development was limited by module costs (red line, 5\$/W_p in 1998), see Fig. 1.4. The strong States driven policies supported its development and PV module cost decreased due to scaling effects to around 1\$/W_p. Silicon module dominate the market (around 90%), even if small breakthrough of thin-film technology started with CdTe (4%). This new technologies are a part of the so-called second generation, which gathers the low-cost technologies, see Fig. 1.3-orange. The figure represents the current module efficiencies as a function of the manufacturing costs (in arbitrary scale) from [4]. Si technology (blue) and PV under concentration (green) are also represented. The solar cell under concentration will be introduced

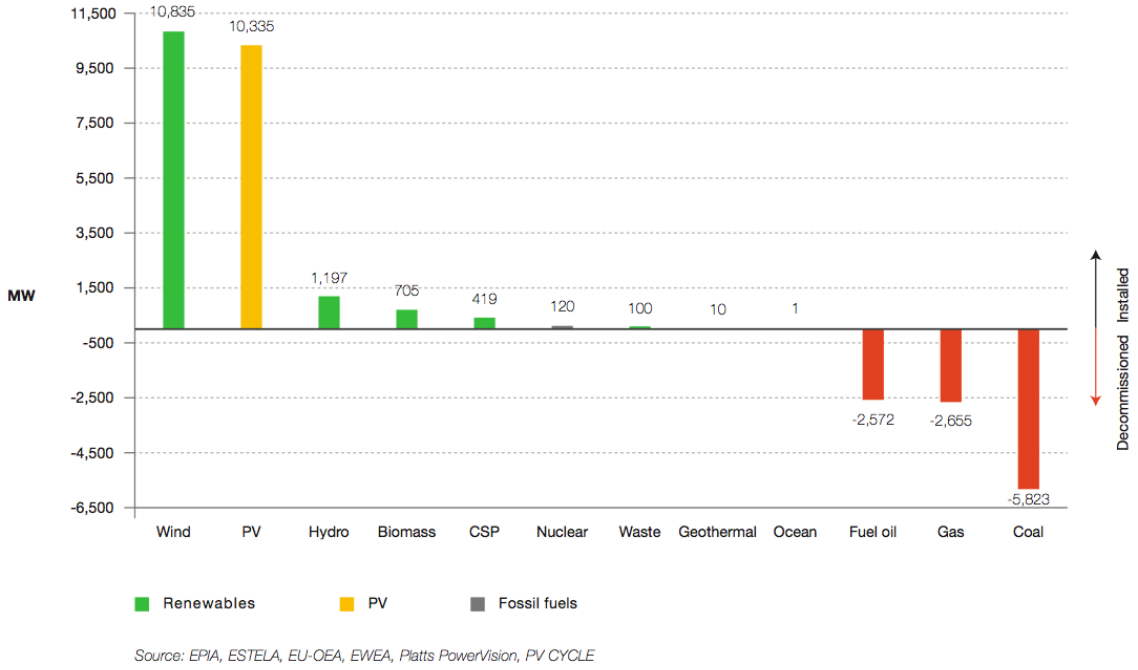


Figure 1.2 – Net power generation capacities added in Europe (EU28) between 2000 and 2013 from [3].

in the next section 1.1.2.

Module costs is not the only only parameter. As one can see in Fig. 1.4, the residential system price was six fold higher than the module price and five fold higher than the commercial one in 2011. The difference between these prices is the BOS (Balance of system) costs. It can be seen in left bar charts representing the conventional PV costs in the USA in 2010 for two installation types: ground mounted and rooftop. The detailed of the BOS costs ($\$/W_p$) are presented in the right bar charts. Therefore, if one wants to lower the total costs either one has to decrease the module costs (second generation photovoltaic) or increase the W_p at constant cost. The W_p increase can be done by increasing the efficiency. This is the aim of third generation PV, which are not limited by the so-called Shockley-Queisser limit contrary to both first generations.

1.1.2 Future Photovoltaic technologies

Shockley-Queisser limit

In conventional solar cells, energy of incident photons from a thermal radiation will undergo a conversion to an electron-hole pair electrochemical energy [20]. The electron-hole pair will initially acquire the same energy as the incident photon. However, it will dissipate its energy through thermalisation phenomena. It will affect

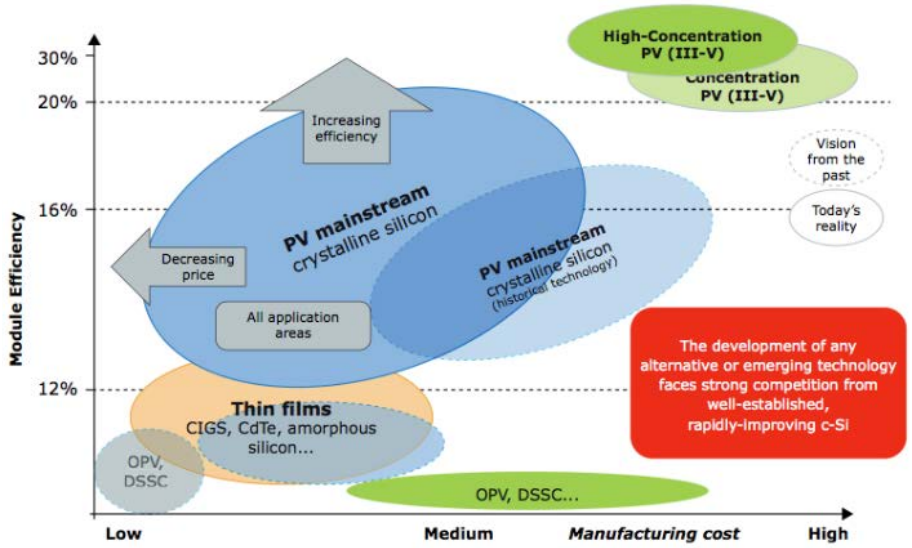


Figure 1.3 – Module efficiency as a function of the manufacturing costs in arbitrary unit for different module technologies, from [4]

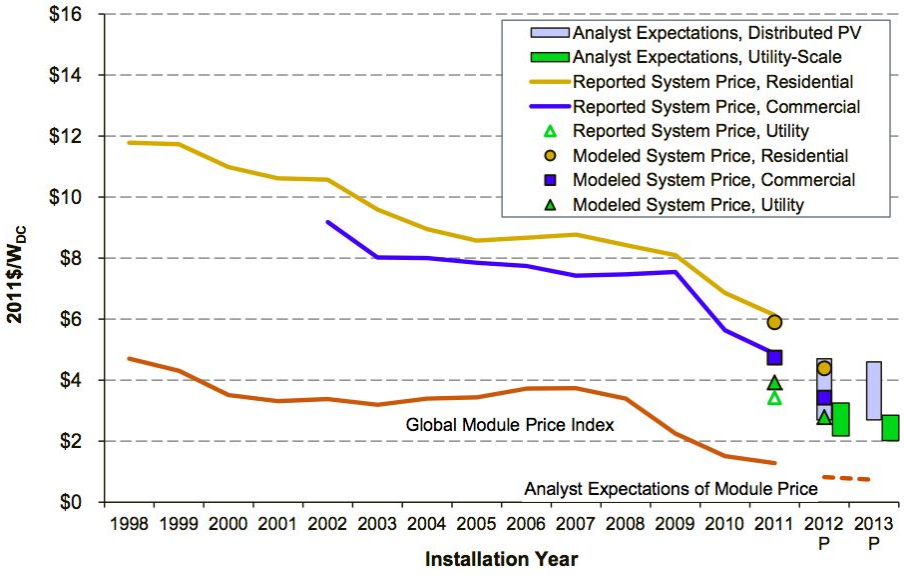


Figure 1.4 – Module and system prices (US dollars) on residential and commercial installations in US from [5].

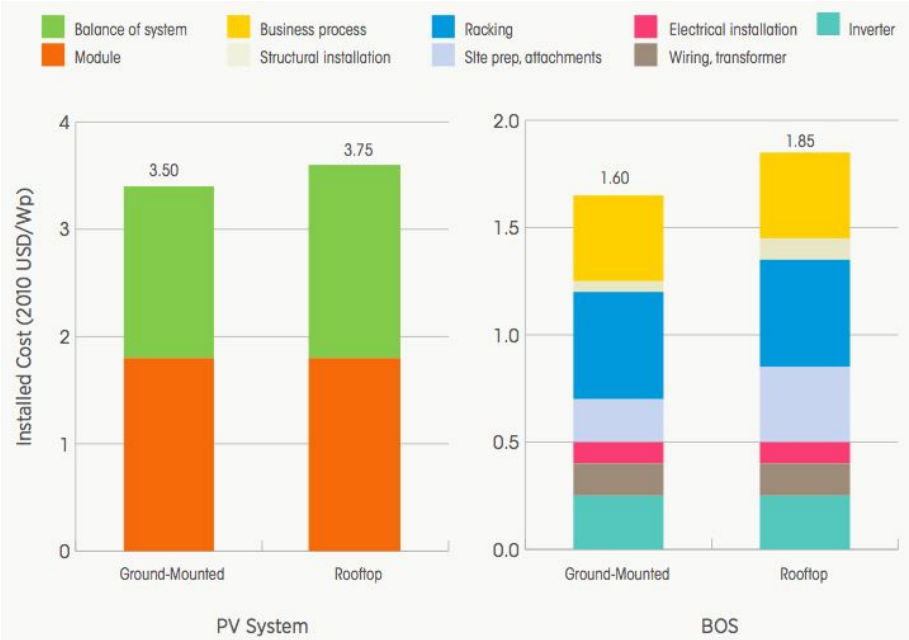


Figure 1.5 – PV installation costs in $\$/W_p$ of ground mounted and rooftop in the left. In the right, the balance of system is detailed according to both installation types, from [2]. Reported costs of conventional PV in 2010, USA.

the electron-hole pair within a few picoseconds [21] to reach the band gap. Therefore, the smaller the semiconductor band gap the higher the entropy generation. But the higher the energy band gap, the higher its transparency. A balance between thermalisation and non absorption has thus to be found. This trade-off was introduced by Schockley-Queisser (SQ) [22] and sets the ideal band gap energy for a solar cell under AM1.5 (solar spectrum) at around 1.4 eV and at 1 eV under full concentration. Full concentration is the maximum solar concentration flux achievable on earth considering the sun and cell solid angles, see [23]. Fundamental SQ conversion efficiency limit reaches 30% and 40% respectively in standard conditions and full light concentration. P. Würfel went beyond the SQ approach, which considered only radiative recombination. He explained all the fundamental losses, which impact the conversion efficiency, by a thermodynamic approach [24]. The Fig. 1.6 displays the fraction of these losses pedagogically as a function of semiconductor band gap [6]. One can see the power out of the cell (dark blue), which increases according to the energy band gap from zero to 30% and decreases again as the band gap increases. This corresponds to the SQ limit mentioned before. As expected, as the energy band gap increases, photons with energy below band gap energy will not be absorbed and the loss by transparency will increase (pink). At last, the thermalisation is represented (light blue) and is the main loss as the energy band gap is reduced, i.e. when the photons excess energy ($E_{ph} - E_g$) is higher.

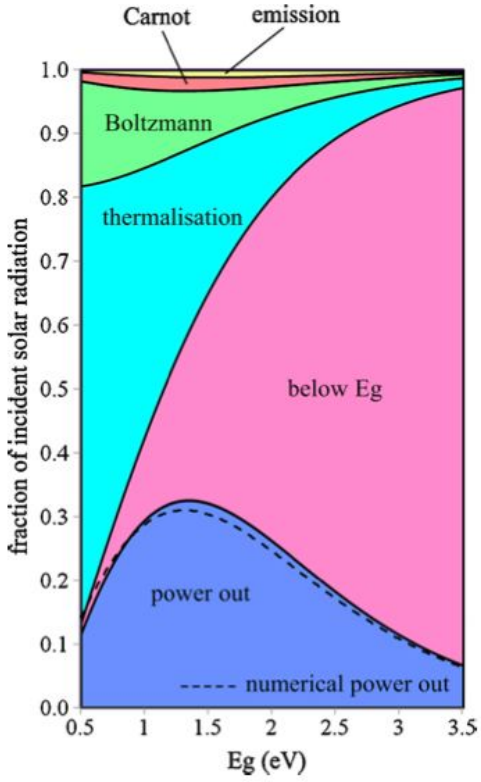


Figure 1.6 – Power ratio of the different losses in a photovoltaic solar cell as a function of the energy band gap, [6]

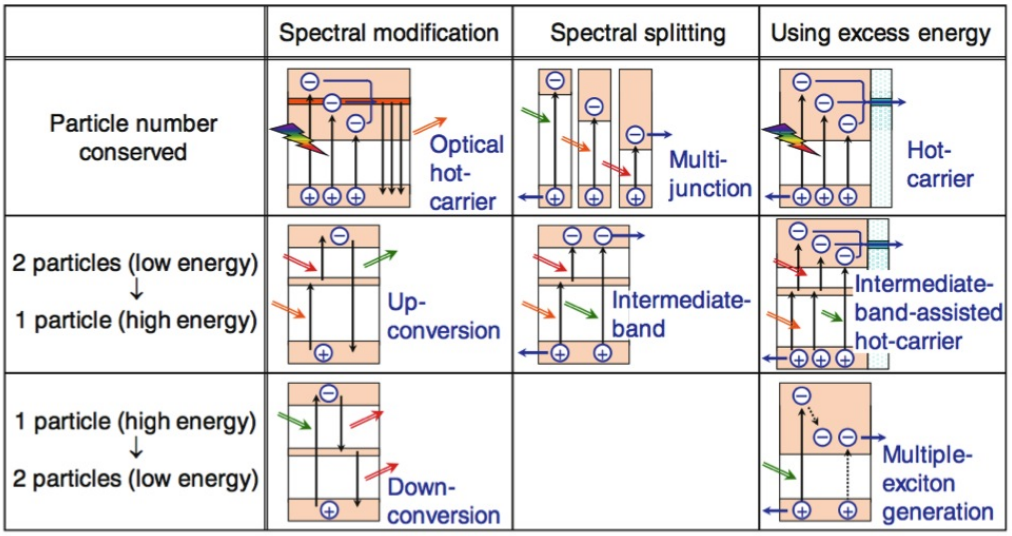


Table 1.1 – Table of the third generation photovoltaics concept for different strategies and their impact on the particle number extracted from [1]

The fundamental limit of thermalisation can be overpassed using new photovoltaics concepts. This emerging field is so-called the third generation photovoltaic.

Third generation photovoltaics

The main idea of the third generation is to go beyond the single junction limitation, while keeping the fabrication costs relatively low. New concepts were widely studied and reviewed by Green in [21]. Takeda also summarized the main concepts in the following Tab. 1.1 in [1]. Three strategies of energy conversion improvement based on spectral modification, spectral splitting and use of excess energy are presented

Some of the concepts are already industrialized (multi-junctions), whereas some others are in the establishment of a proof of concept. Consequently, multi-junctions will be introduced, as it constitutes the most mature concept.

Multijunctions PV As it was said previously, the multi-junctions are well established among the third generation photovoltaic devices. The idea is based on the thermalisation reduction through spectral splitting of the broad solar emission in small energy intervals. Jackson presented the concept in 1955 [25] and did not receive immediate interest. Indeed, he proposed two concepts the optical spectral splitting of the light towards juxtaposed cells, and the cells stacking. Nevertheless, most individual researchers only saw juxtaposed cells, which had to work at their maximum output, which was already a challenge in itself. However, the interest

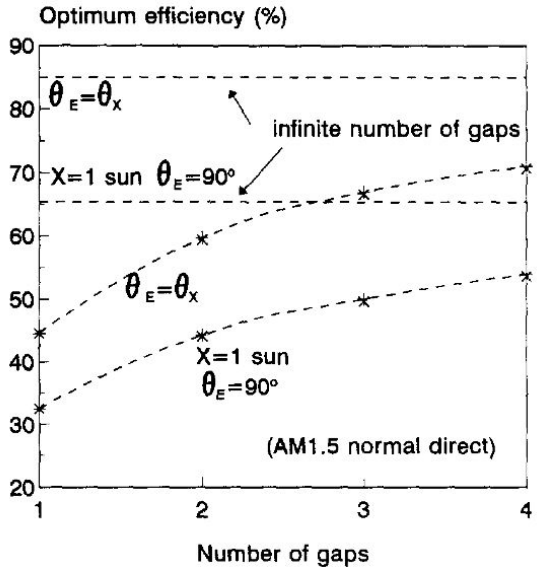


Figure 1.7 – Conversion efficiency limits as a function of the number of jonction under AM1.5 irradiation extracted from [7]

grew again as Moon *et al.* made a proof of concept and as Hamakawa *et al.* transposed the concept to low-cost thin films of amorphous Si [26, 27].
Nowadays, multi-junctions cells have reached 44.4% and 44.7% for respectively triple and quadruple junctions under 302 and and 297 suns [28, 29]. The triple junction was made by Sharp. It is a monolitic cell made of three diodes InGaP/GaAs/InGaAs. The quadruple junction was made by the conglomerate Fraunhofer, CEA-Leti, Soitec, HZB. It is based on the bonding of two separate cells of GaInP/GaAs and GaInAsP/GaInAs. These world records are very impressive, although it "only" consists in small cell results. The difference between cells and modules efficiency is huge and results mainly from front concentration optics losses. They represents 10 points as the best module efficiency is held by the NREL with a 35.9% efficiency [28].
In order to get a better idea of the theoretical potential of multi-junctions we plotted the maximum efficiencies as a function of the number of energy band gaps under AM1.5 illumination in Fig. 1.7 from [7].

The maximum theoretical efficiency for a quadruple junction device is 50% and 70% for 1 sun and full concentration illumination. To that end, there is still room for improvement. However, multi-junctions suffers from two strong limitations. Firstly, the junctions are connected in series, which imposes a current matching. Thus the lowest current flow output in a junction will limit the current of the stack. It implies a condition on band gap energy selection in order to satisfy the current and lattice (if monolithic growth) matching. The current matching also induces a strong

spectral dependence which will tend to lower the output power, when the incident light spectrum changes (thickness of atmosphere, water turbidity...) [30].
We have shown multi-junctions are already efficient and consist in the most mature concept of the third generation. However, in future, it will be limited by fabrication technical complexity and the costs it will engendered. Consequently, we will introduce the HCSC concept with the aim of responding to these limitations.

1.2 Introduction of hot carrier solar cell concept

1.2.1 General presentation of the device

The concept: Ross and Nozik's thought

HCSC concept was introduced by Ross and Nozik in 1982 [17]. The question behind their concept is to know the performance of a material with no thermalisation with the lattice so the carriers would keep their kinetic energy. Indeed, the carrier distribution in a semiconductor after generation is defined by the product of the incident spectrum and the density of state in the semiconductor. Accordingly, the continuous illumination will generate a non Maxwellian distribution. This carriers distribution will be affected by carrier-carrier interactions, i.e. some of the carriers will have high velocities, some others will have lower ones, and their energy exchange will form an equilibrated distribution defined as a Maxwellian distribution. At this point, the distribution can be characterised with a quasi-Fermi levels splitting and hot temperature of emission. Consequently, if one extracts the hot carriers before they thermalise, conversion efficiency might be much higher. This is the tenet Ross and Nozik established. From this definition, they extracted a theoretical maximum conversion efficiency of 66% under AM1.5 approaching the infinite stack of cells.

Würfel's analysis

In 1997, P. Würfel translated this HCSC concept into the more "realistic" picture seen in Fig. 1.8. Considering the impact ionization dominating Auger recombination and inelastic phonons scattering in the absorber, he explained the establishment of a hot distribution, which must not be in contact with metallic electrodes, where the phonon scattering prevails. Consequently, hot carriers must be isolated and their extraction should be isentropic to minimize their thermalisation towards ambient temperature. The energy selective contacts (ESC) would satisfy these conditions. We will introduce this notion further in section 1.2.3. He also emphasizes that the

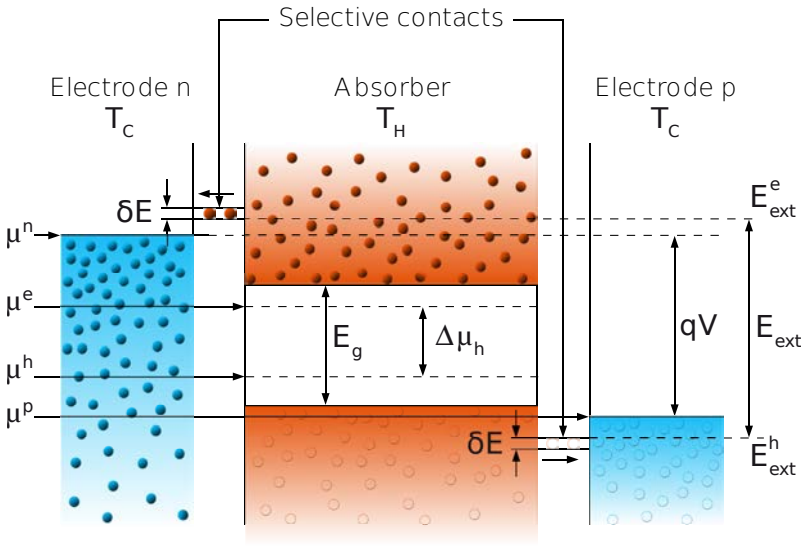


Figure 1.8 – Schematic of a HCSC extracted from [8]

new absorbers should be found, as impact ionization improvement would not be sufficient to realise the concept.

Definition of standard parameters

In order to understand the predominant parameters P. Würfel introduced, we will present some simulation results, which essentially comes from A. Le Bris' thesis [8]. Before showing the influence of the parameters, let us define them using the schematic Fig. 1.8. The parameters can be divided into three categories: the thermodynamic quantities, the device parameters, and the interactions parameters which are not represented in the schematic.

Thermodynamic quantities are the hot quasi-Fermi levels and the hot temperature of electrons and holes, respectively μ^e, μ^h, T_e^h and T_h^h, which come from their Fermi distributions. The difference between the quasi-Fermi level of holes and electrons is the so-called hot quasi-Fermi levels splitting. The temperature of emission, here T^h, is defined as the geometric average of the temperature of electrons and holes.

Device parameters are the extraction energy of holes E_{ext}^h and electrons E_{ext}^e. The difference between both is the extraction energy E_{ext}. Another crucial parameter is the selectivity of the contact δE, the energy width of the contact. At last μ^n and μ^p are the "cold" quasi-Fermi level of electron and hole; their difference will give the electrical difference of potential qV. In a classical solar cell the electrical

difference potential will be written as:

$$qV = \Delta\mu_l = \mu^n - \mu^h \tag{1.1}$$

whereas in the case of a HCSC:

$$qV = \Delta\mu_l = \left(1 - \frac{T_l}{T_h}\right) E_{ext} + \Delta\mu_h \frac{T_l}{T_h} \tag{1.2}$$

with T_l the lattice temperature. If $T_h = T_l$ we found the Eq. (1.1).

Interaction parameters and their interaction are the following:

- Energy band gap of the absorber E_g, light/matter interactions
- Thermalisation rate Q, carriers/phonon interactions
- Light concentration (or/and re-equilibration rate), carrier-carrier interactions
- Electrical contact conductance G, hot/cold distributions interactions

1.2.2 Thermalisation rate parameter

Thermalisation phenomenon in the absorber is the first and main parameter one has to considered. It was neglected in the initial models from Würfel, Ross and Nozik. However, it needs to be evaluated and measured so its impact on the efficiency can be fully known. Firstly, we will start by defining the origin of carrier thermalisation. Secondly, we will show the experimental evidences of hot carrier existence thanks to the thermalisation rate reduction. Thirdly, we will demonstrate that the thermalisation rate definition has to be standardised so that samples can be compared. At last, the lack of experimental data in standard conditions and the crucial importance of the evaluation of the thermodynamic quantities will be pointed out.

Origin of thermalisation

The thermalisation process is the phenomenon, which causes the carriers energy dissipation. It is much faster than radiative recombination between electron and hole (in a time scale around 3 order magnitude smaller see Fig. 1.9). The thermalisation results from electron-phonon interactions, which can be divided in two sub-categories: intra-valley or inter-valley scattering. These scattering processes originate from different electron-phonon couplings. Intra-valley scattering comes from the coupling between the electrons and the material polarisation: electron energy loss emits longitudinal optical polar phonons. The inter-valley scattering comes

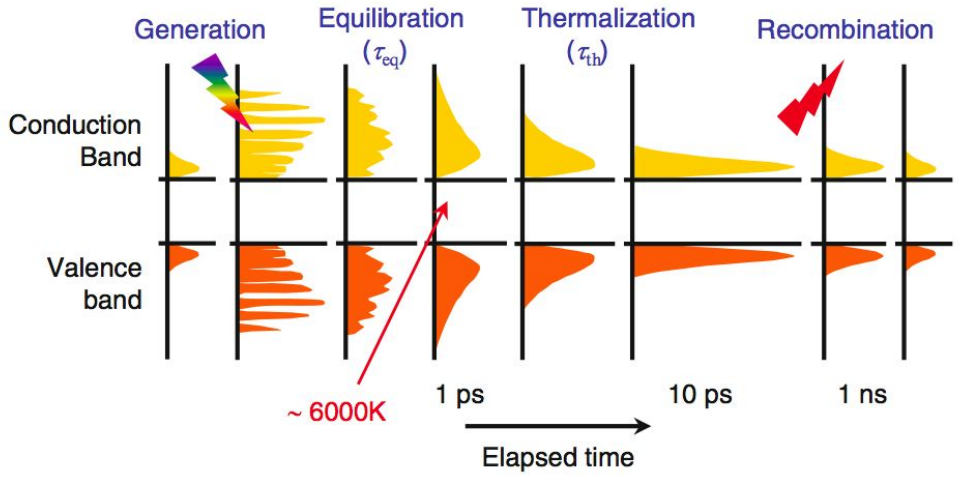


Figure 1.9 – Time evolution of carrier distribution after pulse solar excitation. Schematic extracted from [1].

from carriers energy dissipation through deformation potential of the crystal, and it involves optical or acoustic phonons emission. If one compares the scattering processes emission rate, the inter-valley one is one order of magnitude higher than the intra-valley one. This statement is true, only if the gamma valley is the lowest one. These mechanisms were proven experimentally by [31] and then theoretically explained in [32, 33]. After generation of the optical phonon, the phonon will either decay into lower energy phonons, i.e. entropy loss, or will be reabsorbed. Reabsorption is possible if the decay time of the optical phonon is at least of the same order of magnitude than the phonon generation rate. This phenomenon is so-called the phonon bottleneck effect. The decomposition of the optical phonons are widely treated in [34, 35, 36, 37]. Phonon or band engineering are the way to reduce thermalisation. The aim of band engineering would be to collect carriers before they thermalise, as the thermalisation characteristic length is around 10 nm according to [21]. Several measurements of thermalisation reduction in various semiconductors have been performed. These results will discussed in the next subsection.

Experimental evidence of hot carriers

The experimental evidence of hot carrier was reviewed by A. Le Bris in [8]. Strong interest was shown on the study of carrier cooling rates in GaAs quantum well structures. The most commonly studied structures were GaAs/AlGaAs multi-quantum wells and super-lattices. An experimental study by Xu and Tang [38] using picosecond photoluminescence showed that the carrier energy loss rate is much more carrier-density dependant in quantum wells than in bulk material. As a consequence,

the carrier cooling rate is strongly reduced in quantum wells and becomes significantly lower than in bulk when the carrier density is higher than $10^{18}cm^{-3}$. They also found that higher carrier temperatures were reached in QWs than in bulk under high excitation. Another study [39] stated that the cooling rate measured in a modulation doped GaAs/AlGaAs multi quantum well was reduced by a factor of 60 compared to the predicted rate using a three-dimensional nondegenerate-electron model. Different hypotheses were proposed to explain this reduced thermalisation in 2D systems: a modification of the energy loss rate could arise from a change either in the phonon emission rate or in the phonon decay rate. Shah *et al.* rejected the effect of the reduced dimensionality on the optical phonon lifetime or a screening of the electron-phonon coupling by a high plasma density [40], in favour of a non-equilibrium LO phonon population, in excess of what is expected in the 2D system. Leo *et al.* [41, 42] then studied the influence of the well width on the energy loss rate reduction. They showed that at high carrier densities (up to $10^{18}cm^{-3}$), the cooling rate was slower in thick wells (20 nm) than in thin ones (3 nm). This difference however disappears when one considers the sheet carrier density rather than the volume carrier density as parameter. This indicates that the main effect in the energy loss rate reduction in 2D systems is the selection of wave vectors parallel to the plane of the well in the electron-phonon interaction. Therefore, the phonon emission rate becomes only dependent on the sheet carrier density, and independent of the well thickness. This is confirmed by theoretical studies highlighting the influence of interface modes in the electron-phonon scattering rate [43, 44]. The impact of a modification of the LO phonon lifetime by the material structuration would then play only a minor role. This was in agreement with a theoretical study of hot phonon effects in GaAs/AlGaAs systems [45]. Nevertheless, the conclusion above was only valid in the range of carrier density that was considered ($10^{15} < n < 10^{18}cm^{-3}$). Pelouch *et al.* re-examined the problem in the $2 \times 10^{18} < n < 1.5 \times 10^{19}cm^{-3}$ range [46], showing that the carrier energy loss rate was indeed reduced in 2D systems compared to bulk for carrier density higher than $2 \times 10^{18}cm^{-3}$. They found that the effect was stronger in thinner wells, and that the reduction becomes more pronounced with an increased photo-generated carrier density. Such a reduction of energy loss rate was related to an enhanced hot phonon effect because of a longer LO phonon lifetime due to the two dimensional confinement, in contradiction with previous conclusions. Those results were then confirmed in [47]. The energy loss rate reduction in 2D systems was similarly observed in other materials: InGaAs/InP [48], InGaN/GaN [49] for instance. The long phonon lifetime in quantum structures is usually attributed to the opening of phonon band gaps in the dispersion relation.

The major LO phonon decay process (one LO phonon decaying into two acoustic phonons [34]) can be forbidden if there is no available state with half of the energy of the zone center LO phonon [50, 51]. Other experiments of pulse laser excitation were performed on graphene and pointed out hot carriers generation [52, 53] of around $1 \times 10^{11} cm^{-2}$ and therefore around $1 \times 10^{21} cm^{-3}$ considering the sheet thickness. It was shown that the carrier-carrier scattering was very efficient and prevailed over phonon emission. Furthermore, the hot carrier temperature has shown a dependence on the energy of the incident photons.

Introduction of the thermalisation rate parameter

Definition It was seen in the previous section that thermalisation could be reduced. Measurements of hot carrier temperatures were made on various samples and under different experimental conditions. Therefore, A. Le Bris proposed the use of a thermalisation rate parameter Q so as to facilitate the comparison between the different samples. Its definition relies on a semi-empirical analysis where the absorbed power is considered to be only dissipated by thermalisation, i.e. emission of LO-phonon, see [54]. The analysis is also described in [8]. Consequently, the thermalisation rate Q in $W/K/cm^{-2}$ is written:

$$P_{th} = Q(T_{e-h} - T_l) exp\left(\frac{\hbar\omega_{LO}}{k_b T_{e-h}}\right) \tag{1.3}$$

where T_{e-h}, T_l, ω_{LO} are respectively the temperature of emission, the lattice temperature and the longitudinal optic phonon frequency. The latter parameter is crucial, therefore it will be detailed and calculated in the next chapter for various samples.

1.2.3 Energy selective contacts

ESC role

Thermalisation rate can be reduced in the absorber and a hot electron-hole distribution can be generated. Before introducing the other parameters of influence, the ESC has to be introduced. The aim of ESC is to extract carrier at optimum energy level minimizing the entropy exchange with the outside. Therefore, the energy selectivity δE should be the narrowest. However, carrier extraction should be fast enough otherwise the carrier will thermalise. Consequently, there is a trade-off between electrical conductance of the ESC and the thermalisation rate. Various strategies are currently investigated in order to fabricate these ESC. We will introduce the resonant tunnelling contacts made from QWs in a double barrier and the

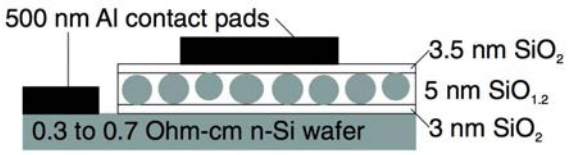


Figure 1.10 – Schematic structure employed by König *et al.* extracted from [9] which was used in order to show extraction of hot carriers generated in the bulk Si by a pulse laser excitation at different wavelength and extracted through resonant QDs of Si to Al contacts

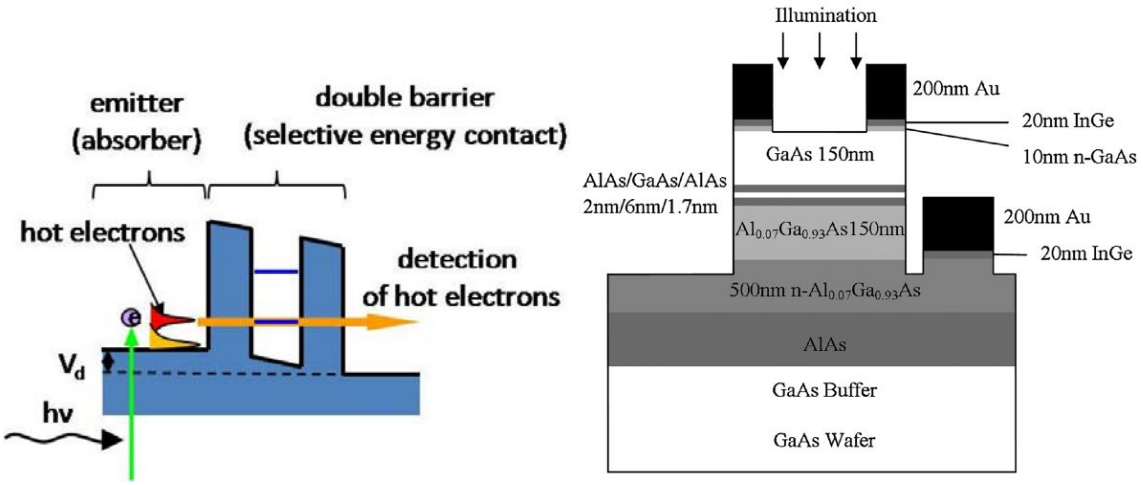
QD embedded in a matrix. Some other concepts were proposed such as superlattice contacts and optical selective contacts [55].

ESC: in the making

Quantum dots as resonant barrier tunnelling are made of nanocrystals surrounded by thin insulating layers. The insulating barrier prevents the phonon scattering from absorber to metallic contacts while the nanocrystals transfer the charge. Indeed a nanocrystal presents two energy levels and as a consequence can be used as an energy selective contact for electron or hole. For example, the extraction of hot electrons from a PbSe nanocrystal to a wide band gap semiconductor TiO_2 was shown by Tisdale *et al.* under a pulse excitation laser [56]. It was also shown that electrons could be transfered from a hot to a cold distribution, using Si dots surrounded by an SiO_2 matrix in a silicon absorber excited by pulse excitation [57, 58]. The corresponding structure is found in Fig. 1.10. Similar results were obtained on a different structure made of a GaAs substrate with QDs of InAs embedded in AlGaAs matrix [10].

Resonant tunnelling barriers The same team also investigated resonant tunnelling and showed an effective extraction of hot carriers. The proposed structure was made by MBE (molecular beam epitaxy) on a GaAs substrate. It was composed of a AlGaAs double barrier with a GaAs QW [10]. The schematic of a resonant tunnelling double barrier is represented and is extracted from the same article [10]. A similar device was proposed by Dimmock *et al.* with a one electron-ESC [59]. He found a good agreement between the simulation and the experiments. But once gain, experimental conditions were unrealistic.

There is a main difference between QWs and QD embedded in a double barrier. Indeed in a QD, the carrier transmission function is controlled according to all the momenta. It ensures a spatial and energetic selectivity, which is not provided by QWs. Therefore, better results on QD are expected even if the technical realisation

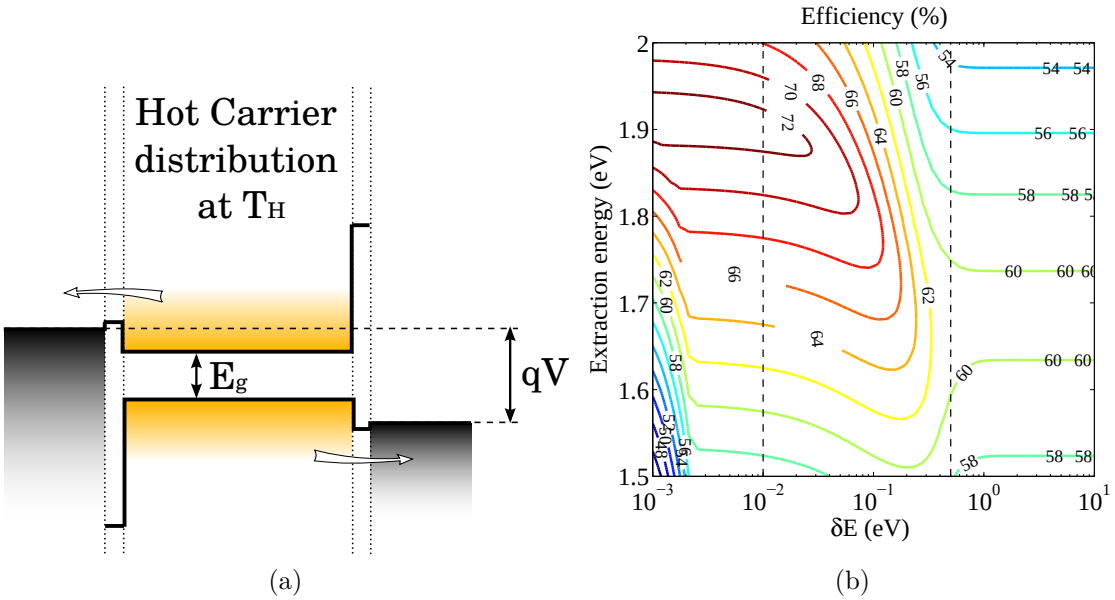


(a) (b)

Figure 1.11 – Schematic energy band diagram of a resonant tunnelling barrier extracted from [10].

of high conductance contact is much more complicated. All the previous experiments presented showed hot electron extraction, however no experimental study has yet been done on contact quality and therefore on optimum conductivity. Moreover, the proof of hot carrier extraction above was not made under standard conditions. They used pulse laser excitation or/and low lattice temperature measurement. Their aim was to show the feasibility of a ESC.

Semi-selective contacts A. Le Bris introduced an alternative solution to ESC. It could simplify the carrier extraction and make an intermediate step between the HCSC and the standard junction: the semi-selective contacts. It consists in an energy high pass filter. Thus, the fabrication can be simplified since classical wide band gap semiconductors with different chemical potentials can be used. The HCSC with semi-selective contacts is represented with the schematic in Fig. 1.12a. The analysis is based on balance equations, and the selectivity of the contact was shown not to be fundamental [60]. The Fig. 1.11b shows the iso-curves of conversion efficiencies as a function of extraction E_{ext} and the selectivity δE energies for a 1 eV energy band gap. One can see that the maximum conversion efficiency reaches 60% for low selectivity ($\delta E > 1\,eV$ for $1.65\,eV < E_{ext} < 1.75\,eV$) whereas it attains 72% at high selectivity ($\delta E < 10^{-2}\,eV$ for $1.9\,eV < E_{ext} < 1.95\,eV$) in the ideal case of full concentration. The difference is not that important however it is still far beyond SQ limit.



(a) (b)

Figure 1.12 – Schematic of a HCSC with semi-selective contacts extracted from [8] (a). Iso-efficiency curves as a function of extraction energy and contact selectivity for full concentration with a 1 eV energy band gap (b), from [8].

In this section, it has been seen that the ESC realisation is on the way but still requires further investigation. Moreover, studies focused on electrons extraction as no ESC for holes has been made yet. In the next section, we will finish to introduce the other parameters of influence taking into account both thermalisation in the absorber and ESC characteristics.

1.2.4 Theoretical performances

G. Conibeer defined the ideal absorber through a non exhaustive list of parameters [35]. As said, the internal parameters (low optical/acoustic phonon coupling, small band gap...) can be separated from the external ones (abundance, non-toxicity...). Here, we will focus on the parameters, which influence the performances. Thus, only the internal parameters will be broached.

Interactions parameters

Energy band gap The influence of the energy band gap on the efficiency is very important, as shown in section 1.1.2. If the thermalisation is suppressed, the efficiency will only be affected by the absorbed power. We can plot the efficiency as a function of the energy band gap in the case of an ideal HCSC in Fig. 1.13. The efficiency limit for a 0 eV band gap is 87% at full concentration. It decreases slowly

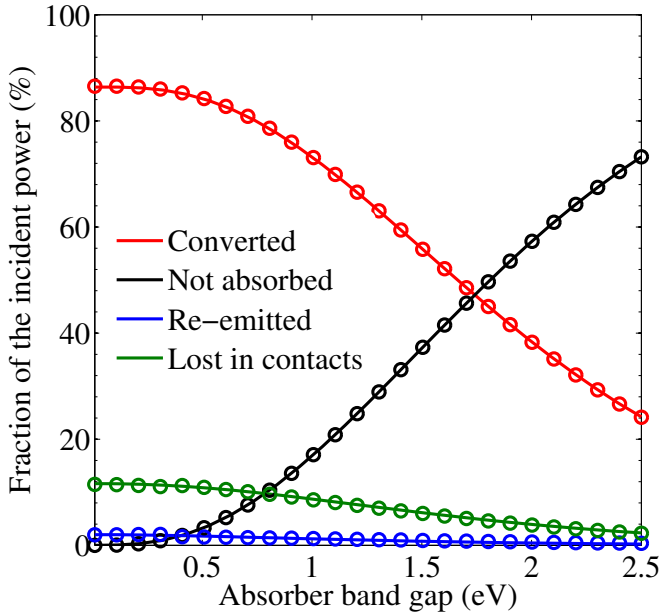


Figure 1.13 – Fraction of the incident power that is converted (red), not absorbed (black) and lost in the selective contacts under full concentration and no thermalisation extracted from [8]

until 1 eV and then decreases linearly from 1 to 2.5 eV. Therefore, an energy band gap smaller than 1 eV has to be used.

High injection The concentration has a strong influence on $\Delta\mu$. This is not limited to HCSC as in standard solar cells $\Delta\mu$ depends on the logarithm of the carrier density. Takeda plotted the fraction of the incident power, which is converted into a 0.7 eV absorber with no thermalisation as a function of the carrier density, see Fig. 1.14. One can see the linear increase with the logarithm mentioned before. Carrier concentration is a crucial parameter. High carrier concentration can be achieved either by optical means and/or thickness reduction.

Extraction energy Carriers extraction energy will highly depend on the carriers distribution. For this reason, in the case of no thermalisation and full absorption, extraction energy is expected to be close to the average incident photon energy which is 1.85 eV for a AM1.5 solar spectrum. A. Le Bris plotted the conversion efficiency as a function of the extraction energy for different energy selectivity for a 1 eV energy band gap absorber in the absence of thermalisation in Fig. 1.15. One can see the influence of the extraction energy is strong as the conversion efficiency increase from 40% to 70% as E_{ext} increase respectively from 1 to 2 eV when $\delta E = 1meV$. An optimum E_{ext} depending on the energy selectivity can be found. It

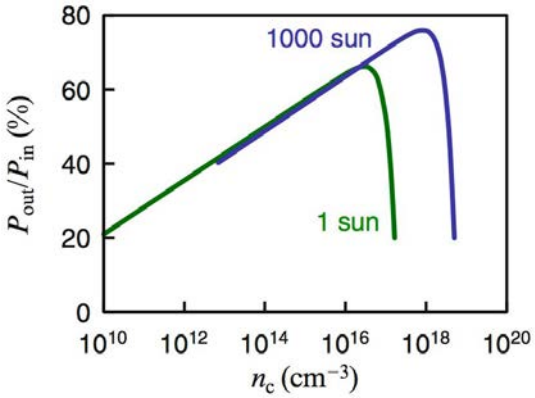


Figure 1.14 – Fraction of the incident power that is converted with as a function of the carrier density for 1 (green) and 1000 suns (blue) illumination extracted from [1]. Eg=0.7 eV, Eext=1.54-1.58 eV no thermalisation

decreases slightly with the selectivity increase even if as expected, it stays close to the average photon energy. At last, beyond the optimum, the decrease of the conversion efficiency is slightly weaker, which means that the extraction energy should be rather overestimated than underestimated.

Optimized conductance Carriers extraction will affect the hot equilibrated distribution, as it will change the inside carrier density. The extraction rate can be defined by a conductance parameter. A. Le Bris studied the influence of the carrier extraction on a HCSC by simulating the efficiency as a function of the conductance for different contact selectivities, see Fig. 1.16. Once again, the conductance has a strong influence on the conversion efficiencies. Whatever the selectivity, as the conductance increase the conversion efficiency increases, reaches a plateau (optimum) and then decreases again. SQ limit is reached when the conductance is too high as carriers will thermalise in the contacts. And the optimum conversion efficiency shifts towards higher conductance when increasing δE.

The parameters influencing the performances of HCSC were introduced. Reduction of thermalisation in MQWs was observed experimentally and ESC are in current development. Consequently, contact-less characterization of the absorber by standard quantities should be develop until ESC are mastered.

1.2.5 Need to qualify performances of the absorber through standard quantities determination

The global performances of a solar cell depends on energy and charge current densities balance equations which are derived from the particle conservation model,

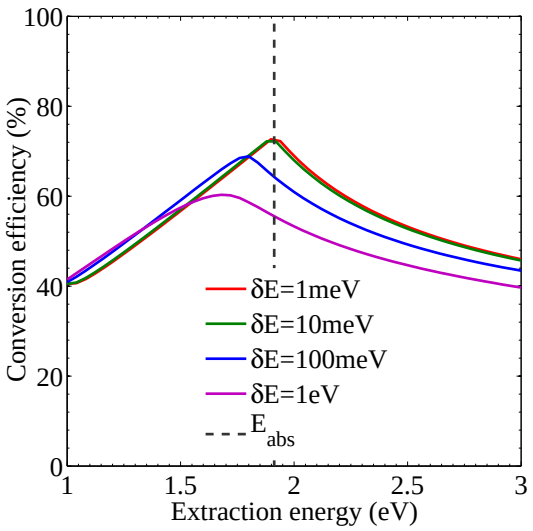


Figure 1.15 – Conversion efficiency as function of the extraction energy for a 1eV band gap absorber under full concentration for different energy selectivity width extracted from [8]

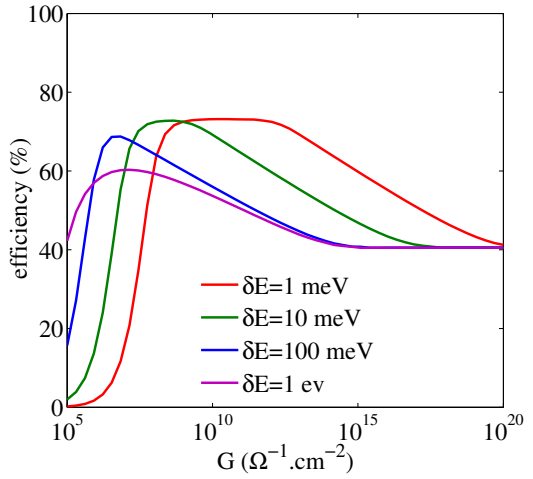


Figure 1.16 – Conversion efficiency as a function of the contact conductance for different energy selective width. The extraction energy was optimised for each conductance and selectivity. Eg=1eV, concentration=46000 suns

see [61]. However, compared to Würfel's analysis the thermalisation power term P_{th} is taken into account. Therefore the equations become:

$$J = J_{abs} - J_{em}(\Delta\mu, T_{e-h}) \tag{1.4}$$

$$P = P_{abs} - P_{em}(\Delta\mu, T_{e-h}) - P_{th}(Q) \tag{1.5}$$

With J, J_{abs}, J_{em} are respectively the extracted, the absorbed and the emitted charge current densities and their corresponding energy current densities P, P_{abs}, P_{em}. The absorption terms are related to the incident photon flux and are well known. Therefore, these equations depends only on the thermalisation rate Q and the thermodynamic quantities ($\Delta\mu$,T_{e-h}). We will develop the way we extract each term experimentally in the next chapter in order to get the absorber performances without electrical contacts.

Short summary - New concepts and technologies have a potential of a bigger reduction cost impact regarding their theoretical efficiencies. It improves considerably the simple junction efficiency limit from 40% to 87%. Multi-junctions already achieve 44.7% and spectral splitting coupled to multi-junctions gets a 38.5% record. In this study, we considered another approach which is the HCSC. They have a clear potential of cheaper manufacturing costs. HCSC are now theoretically well known thanks to previous modelling and the first obstacle to overpass seems to get a better insight and understanding of the absorber material through thermalisation rate. Thermalisation rate has to be studied in different materials in order to estimate the performances of the complete device. If the performances are high enough, a particular study can be launched on its opto-electrical parameters. This is a requirement to go beyond theoretical models and start studying materials in standard solar cells conditions.

CHAPTER 2

Hot carrier solar cells characterization tools: definitions, development and preliminary results

The chapter will first introduce the steady-state PL phenomenon from the generalized Planck's law. PL spectra will be acquired from both confocal and HI set-ups, which will be detailed. Then, the samples will be presented through a preliminary statistical study on thermalisation reduction. At last, a bipolar sample will be described in depth, showing that hot carrier study required absorbance measurement.

2.1 Photoluminescence

In chapter 1, the different processes, which establish the existence of an equilibrated hot carrier distribution was seen. There is a need to determine the physical parameters at stake in a real device. Therefore, we need appropriate experimental tools. In this regard, we will study PL experiments. First, the physical model describing photoluminescence (PL) experiments will be developed. Then, we will explain how we can obtain useful thermodynamic quantities from a PL spectrum.

2.1.1 Generalized Planck's law

Non-thermal luminescence process comes from the recombination of an electron-hole pair distribution separated by a forbidden energy gap. It is an inter-band relaxation. Each carrier type (electron or hole) presents a distinct Fermi-Dirac distribution regarding its specific density of states and occupancy rate. One can

consider carriers in equilibrium among themselves in steady-state regime. A unique Bose-Einstein distribution can be defined for photon emission, i.e. the electron hole pair radiative recombination, which follows the generalized Planck's law Eq. (2.1), [20]. Thus, the PL emission per unit volume within solid angle Ω of an element of semiconductor writes as:

$$I_{PL}(\hbar\omega) = \alpha(\hbar\omega) \times \frac{\Omega n^2}{4\pi^3\hbar^3 c_0^2} \times (\hbar\omega)^2 \left[\exp\left(\frac{\hbar\omega - \Delta\mu}{k_b T_{e-h}}\right) - 1\right]^{-1} \tag{2.1}$$

where I_{PL}, $\hbar\omega$, α, Ω, n, $\Delta\mu$, T_{e-h}, are respectively the PL intensity, the photon energy, the absorbance, the solid angle of emission, the refractive index of the medium, the chemical potential of radiation, and the temperature. The concept of chemical potential of radiation will be detailed in the next subsection. At high energy, i.e. $\hbar\omega - \Delta\mu > k_b T_{e-h}$, the Bose-Einstein distribution can be approximated by a Maxwell-Boltzmann distribution:

$$I_{PL}(\hbar\omega) = \alpha(\hbar\omega) \times \frac{\Omega n^2}{4\pi^3\hbar^3 c_0^2} \times (\hbar\omega)^2 \exp(\frac{-\hbar\omega}{k_b T_{e-h}}) \exp(\frac{\Delta\mu}{k_b T_{e-h}}) \tag{2.2}$$

As the PL spectrum is acquired outside the semiconductor ($n = 1$) with a solid angle Ω_{out}, the generalized Planck's law simplifies as a product of an absorbance term A, the black body spectrum Φ_{BB} and an exponential term of intensity related to $\Delta\mu$:

$$I_{PL}(\hbar\omega) = A(\hbar\omega)\Phi_{BB}(\hbar\omega) \exp\left(\frac{\Delta\mu}{k_b T_{e-h}}\right) \tag{2.3}$$

where:

$$A(\hbar\omega) = \alpha(\hbar\omega) \times \frac{\Omega_{out}}{4\pi^3\hbar^3 c_0^2}$$

As usual spectrometer acquires spectrum in wavelength intervals, one must convert the PL spectrum in energy unit:

$$I_{PL}(E) = I_{PL}(\lambda)\frac{d\lambda}{dE} \tag{2.4}$$

An example of spectrum in wavelength units is plotted in Fig. 2.1. We have represented the different terms (α in blue squares, Φ_{BB} in black squares) of the Eq. (2.3) in order to get a better understanding of their impact on the PL spectrum (red squares).

So as to extract thermodynamic quantities from the PL spectrum, one can rewrite the Eq. (2.2) as a linear equation:

$$\ln\left(\frac{I_{PL}}{A(\hbar\omega)\times(\hbar\omega)^2}\right) = a\times\hbar\omega + b \tag{2.5}$$
$$\text{where : } a = -(k_b T_{e-h})^{-1} \text{ and } b = \frac{\Delta\mu}{k_b T_{e-h}}$$

This form simplifies parameters extraction. In this equation the term $\Delta\mu$ can be ascertained if, and only if, the PL spectrum intensity is known in absolute unit. However, relative units for I_{PL} are enough regarding the lattice and carrier temperatures determination. Let us now see more in details the thermodynamic parameters that can be extracted from a PL experiment.

2.1.2 Thermodynamical probed values

Lattice temperature

The temperature is an indirect measurement of the degree of microscopic agitation in a system. In solid state physics, it reflects the lattice agitation T_l, i.e. vibration waves (phonons). The interaction between electrons and phonons is done through optical phonons, which can decay into acoustic phonons. These acoustic phonons are in equilibrium with the surrounding environment and therefore the material absorbs and emits them continuously. The lattice temperature is thus correlated to the acoustic phonon density and has two main effect on the emitted PL spectrum. Firstly, a change of lattice temperature implies a change in the atomic arrangement. Indeed, there is either a dilatation or a compression of the lattice, depending on the material Varshni's sign parameter [62]. As a result, the absorbance is modified (shape and band gap) implying a PL peak displacement (left and right arrows for T_l in Fig. 2.1). This change is only visible at low energies (high wavelength) as the absorption variation is negligible compared to the exponential decay. Secondly, as the lattice temperature increases, the slope at high energy (low wavelength) will be smaller (rising arrow in Fig. 2.1). It is directly linked to the black-body emission.

Carrier temperature

Under high carrier injection regime or high electric fields, carriers can gain kinetic energy as the carrier-carrier scattering starts prevailing over the phonon scattering, i.e carriers go upper in their dispersion energy band diagrams. Therefore, the

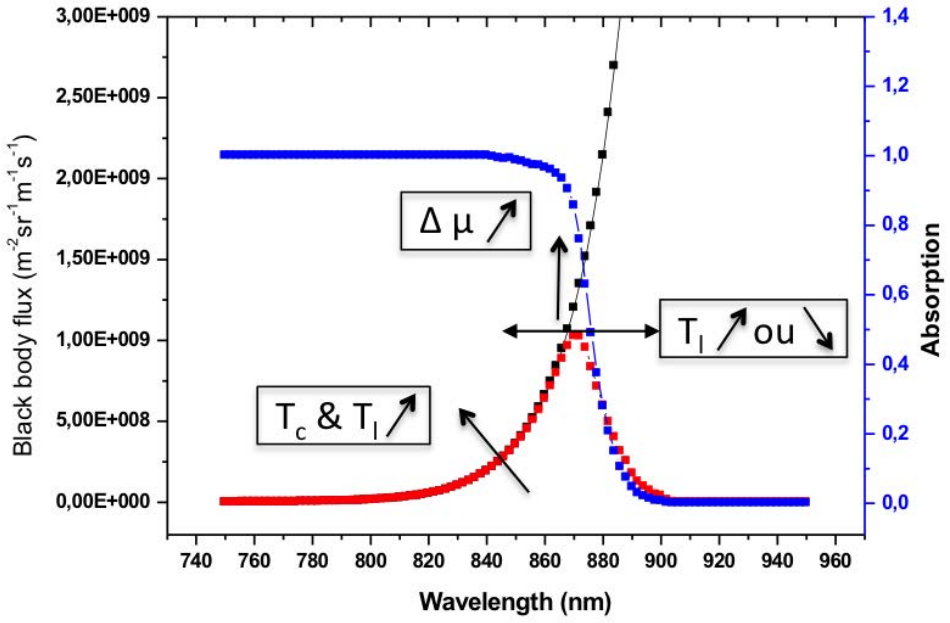


Figure 2.1 – Example of a PL spectrum (red squares) which is the product of absorbance α (blue squares) the black body spectrum Φ_{BB} (black squares), and an intensity term $\exp(\Delta\mu/k_bT)$ described by Eq. (2.3). The arrows represents the influence of the thermodynamic parameters on the PL spectrum.

electron-hole Bose-Einstein distribution will be described by a hot carrier temperature. This temperature is called the temperature of emission T_{e-h}, which is different from the lattice temperature. It gathers the contribution of the kinetic energy gain (temperature of carriers) and of the lattice. Consequently, the effect on the slope at high energy on the PL spectrum will be similar to that of the lattice temperature. However it will not affect the absorption profile. It is therefore the way we will distinguish one from another in section 3.2.1.

Quasi-Fermi levels splitting

Quasi-Fermi levels splitting ($\Delta\mu$) is a thermodynamic quantity that can also be called the chemical potential of radiation. In order to popularize its role, $\Delta\mu$ represents the spread potential of the electron-hole pair. In solar cells, if $\Delta\mu$ is probed at open circuit voltage, it represents the maximum achievable open circuit voltage the cell can deliver at 300 K if, and only if, $\Delta\mu$ is spatially constant [63]. Then, as the generalized Planck's law indicates, the PL intensity depends exponentially on $\Delta\mu$ (rising arrow in Fig. 2.1).

2.1.3 Photoluminescence experimental techniques

The different interaction mechanisms that govern the energy and momentum relaxation of carriers occur at very small time scales. In order to observe these ultra-fast phenomena in the carrier dynamics, different techniques were developed. They were made possible thanks to the development of ultrafast pulsed laser and detection. The main advantage of these time resolved techniques is to provide a direct determination of the energy loss rate by the electron-hole plasma. The different available techniques are described below and reviewed in [33]. This subsection resumes A. Le Bris' work in [8].

Pump-and-probe absorption

In the pump-and-probe technique, an ultra-short laser beam is separated in two part: a pump and a probe. The pump pulse excites the sample under investigation, causing a change in its absorption. A weaker probe pulse then monitors these changes at a time delay δt. By varying δt, the time evolution of the absorption is measured. In that case, the measured absorption can be related to the carriers dynamic at the energy level of the probe beam. As the time resolution is excellent (few fs), it can also be used to monitor time-resolved Raman scattering: here the phonon population is investigated.

Streak camera

A streak camera is a device that records time resolved spectrum. The light emitted from a sample that is photo-excited by an ultra short laser pulse is focused on a photo-cathode that releases an electron flux proportional to the incident light intensity. The electron flux is then accelerated and detected. An applied voltage sweeps the electrons across a phosphor screen: electrons released at a different time will reach the camera at a different position. The spatial intensity profile is then related to the temporal variation of the PL spectrum. Streak cameras have resolutions of a few picoseconds.

Up-conversion gate

After an ultra-short excitation pulse, the PL signal is collected, collimated and combined with a probe pulse, called the gating pulse, in a non linear crystal. The angle of the crystal is set to phase match the frequency of the gating pulse with a selected frequency of luminescence. A signal whose frequency is the sum of the laser and luminescence frequencies is then measured by a photomultiplier. By varying the

time delay of the gating pulse, the temporal profile of luminescence can be obtained. This technique provides a better time resolution than streak camera and offers the possibility to scan further in the infrared.

The techniques described above were used to study the carrier dynamics in semiconductors in the first picoseconds after photo-excitation. However, these techniques requires high injection regime in order to have sufficient detection. As the carriers density has a strong influence on carrier relaxation, one cannot simply extrapolate material performances in continuous excitation regime which is the relevant regime for solar cell operation. We have thus chosen to use our continuous wave PL. As we will see thermalisation properties are measurable. Let us now describe the experimental methods and set-ups.

2.2 Experimental methods

2.2.1 Steady-state photoluminescence set-ups

Relevant conditions for solar cells

In the HCSC characterization one has to keep in mind that experimental measurement conditions are fundamental because it can largely influence the results. It is crucial to insist on this aspect when one wants to get relevant solar cell characterization and performances. The conditions, which affect the hot carrier characterization are: sample temperature, excitation regime (pulsed or continuous), illumination area and injection regime:

- Sample temperature must be higher than 40 K for the GaAs and 80 K as a precaution. Indeed, under these temperatures the impurities scattering prevails over the carrier-phonon scattering and therefore the extracted performances will not be relevant to HCSC behaviour. Moreover it will not be possible to extrapolate ambient room temperature performances. This effect can be seen on thermal conductivity studies as a function of the temperature in [64] but also in the hot carrier spectroscopy review [65].
- Continuous regime, which will be the solar cell operating regime, should be preferred, as mechanism of carrier-carrier scattering and carrier relaxations are strongly influenced by carriers density. Indeed, non steady-state studies could minimize lattice temperature contribution as the lattice cools down between two pulses.
- However, even if pulsed regime is used, a laser spot diameter larger than 15

μm is crucial so the lateral carrier diffusion can be neglected regarding the diffusion length of typical III-V semiconductors (few microns), see [42]. If one uses another material, the spot diameter should be adjusted.

- Then, achievable solar concentration (<46000 suns) is also preferable as, again, it will impact the carrier-carrier scattering and their relaxation.

This is a recommendation list. However, some materials or set-ups can limit hot carrier generation/detection. The first criterion to adjust or change should be the light concentration, which will impact less hot carrier physics.

Set-ups

Two different set-ups were used in order to get steady-state PL spectra: a confocal microscope and a HI. We will describe those set-ups and explain the calibration procedure of the emitted flux.

Confocal mode The confocal set-up is widely used so we will not go into many details. The configuration of the one we developed is introduced in Fig. 2.2a. The main differences between "classical" confocal set-up and the one we use are firstly the spatial resolution, secondly the imaging capability.

- Resolution: as spot diameter should be higher than 15 μm, we deliberately lowered the resolution of the confocal collection area, so we can collect most of the photo-generated carriers and thus maximise the photon detection.
- Imaging: a CCD camera allows us to image the sample, position the sample under the laser spot and ensure the focus is adjusted.

HI mode The HI mode is described in the schematic Fig. 2.2b. The set-up was developed in collaboration with the company *Photon etc.* It provides spatially resolved PL spectra (data cube). Therefore from each pixel (around $0.5 \times 0.5\,\mu m$) of the map we get a PL spectrum. The PL spectra we acquire are in absolute units thanks to the full calibration procedure which consists in spatial, spectral, intensity, and flux calibrations, see [63].

2.2.2 Description of full calibration and measurement method

We have seen that the absolute calibration is required to access some physical parameters, see section 2.1. Four steps are required so we can make a full calibration: spatial, spectral, intensity and flux calibration. The first three steps (so-called partial calibration) can be applied on both set-ups whereas only the HI allows a flux calibration.

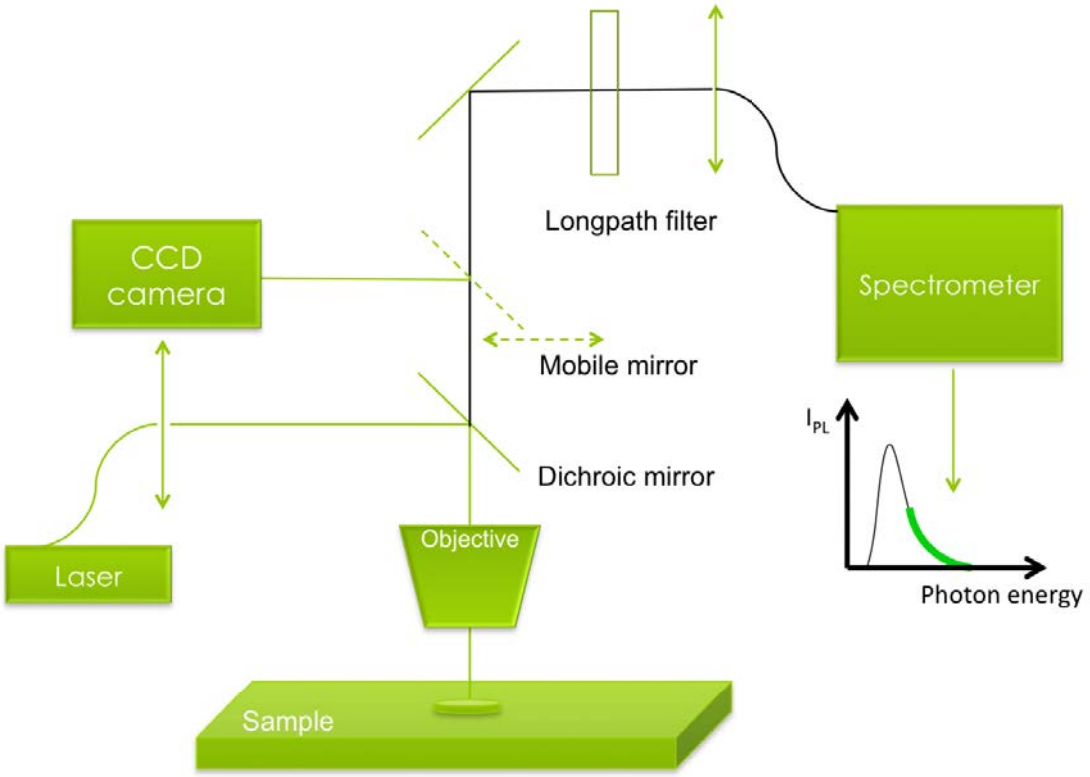
Partial calibration of the set-ups and measurement method

- Spatial calibration is made firstly by imaging a grating which provides the ratio of pixel over microns. Secondly, in order to get the mean absorbed power flux, the laser spot diameter must be determined. Thus, the spot must be well focalised on a surface which is done by adjusting the height while controlling the laser spot image clearness. As the laser is multi-mode and slightly elliptic, the diameter was extracted from the mean of two axis profiles, where each axis diameter was extracted at the full width at half maximum (FWHM). Note that the PL spectra will also be acquired by adjusting the laser clearness on the sample surface. It is not done by maximizing the PL intensity signal so the excitation conditions are kept similar.
- Spectral calibration is performed by measuring rays intensity of a Xe lamp by the spectrometer or the HI. It ensures the wavelength measured corresponds to the one we sent to the detection system.
- Intensity calibration is made thanks to the measurement of a calibrated halogen lamp in an integration sphere. Therefore all spectra will have a correct intensity variation independent on the set-up.
- Flux calibration in HI mode means the emitted photon flux is acquired in absolute units. It is done following the method described in [63]. The principle is to image the output of a fiber laser and measure its incident power. Therefore, PL signal in HI mode is obtained in $N_{ph}/s/m/m^2$.

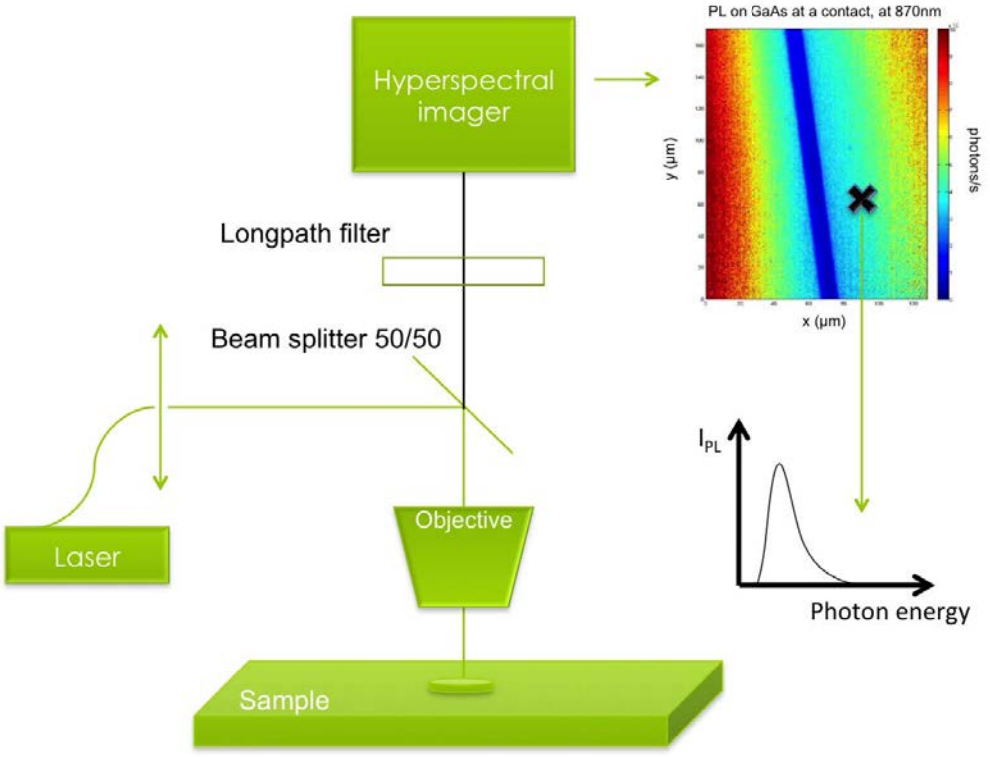
Other measurement requirements Room temperature is always measured by a thermometer as close as possible to the sample as it impacts significantly our results. Samples are always positioned on metallic substrate so the heat is always dissipated.
At last, all the electrical measurements were performed with a Keithley sourcemeter.

2.2.3 Development of a method to compare HI and confocal

The HI set-up has the strong advantage of getting absolute quantities spatially resolved, whereas the confocal one is easier to handle, allows wider spectral range acquisition, and reaches higher incident powers due to the IR objective coupled to a dichroic mirror. Reaching high incident powers is crucial in a hot carrier study as carrier density impacts the thermalisation rate. We propose to combine the two techniques in order to get both advantages by developing a transfer method from one set-up to another (i.e. the confocal set-up flux will be absolutely calibrated).



(a)



(b)

Figure 2.2 – Schematic of the confocal (a) and hyperspectral imager (b) set-ups

The values extracted from this procedure are called *spatial average values*, which are different from the *accurate local values*, which only consist in improving HI measurements. Because both methods are based on HI signal integration they will be introduced in this section. For all the data, as the illumination spot is close to a Gaussian beam and materials are homogeneous, we make the assumption of a cylindrical symmetry.

Accurate local values

The first procedure of spatial integration is made to improve the signal over noise ratio. We change the coordinates system from cartesian to cylindrical HI data. Indeed the farther the pixel from the illumination center, the lower the signal. We integrate the signal over a 360° sector centered at the spot center. This integration, done prior to the extraction of local thermodynamic quantities, will increase the accuracy. This procedure is represented in Fig. 2.3a. It corresponds to an angular average at a fiwed radius (light green zone) of the PL signal according to Eq. (2.6). Therefore, for each radius we get a PL spectrum:

$$I_{PL}(r,\lambda) = \frac{\int_0^{2\pi}\int_r^{r+dr} I_{PL}^{HI}(u,\theta,\lambda)udud\theta}{\int_0^{2\pi}\int_r^{r+dr} udud\theta} \tag{2.6}$$

where $I_{PL}(r,\lambda)$ the radial PL spectrum, r the radius, dS the surface of the ring.

Spatial average values

As said earlier, the spatial average value procedure is made in order to compare confocal and HI data. Indeed, one can see the confocal data as a spatial integration of the HI one. Thus the confocal data can be written as a function of the HI data:

$$I_{PL}(u,\lambda) = \frac{\int_0^{2\pi}\int_0^{\infty} I_{PL}^{HI}(u,\theta,\lambda)FT(u)ududu\theta}{\int_0^{2\pi}\int_0^{\infty} FT(u)ududu\theta} \tag{2.7}$$

with FT a transfer function which represents the function of signal collection of the confocal system, see section 2.3b. As the confocal system spatially integrates the PL intensity through circular optics (lenses, fibers), one can simplify the transfer function as a heavy-side function of radius r, which would corresponds to a collection area of radius r. Therefore the equation becomes:

$$I_{PL}(r,\lambda) = \frac{\int_0^{2\pi}\int_0^{r} I_{PL}^{HI}(u,\theta,\lambda)ududu\theta}{\int_0^{2\pi}\int_0^{r} ududu\theta} \tag{2.8}$$

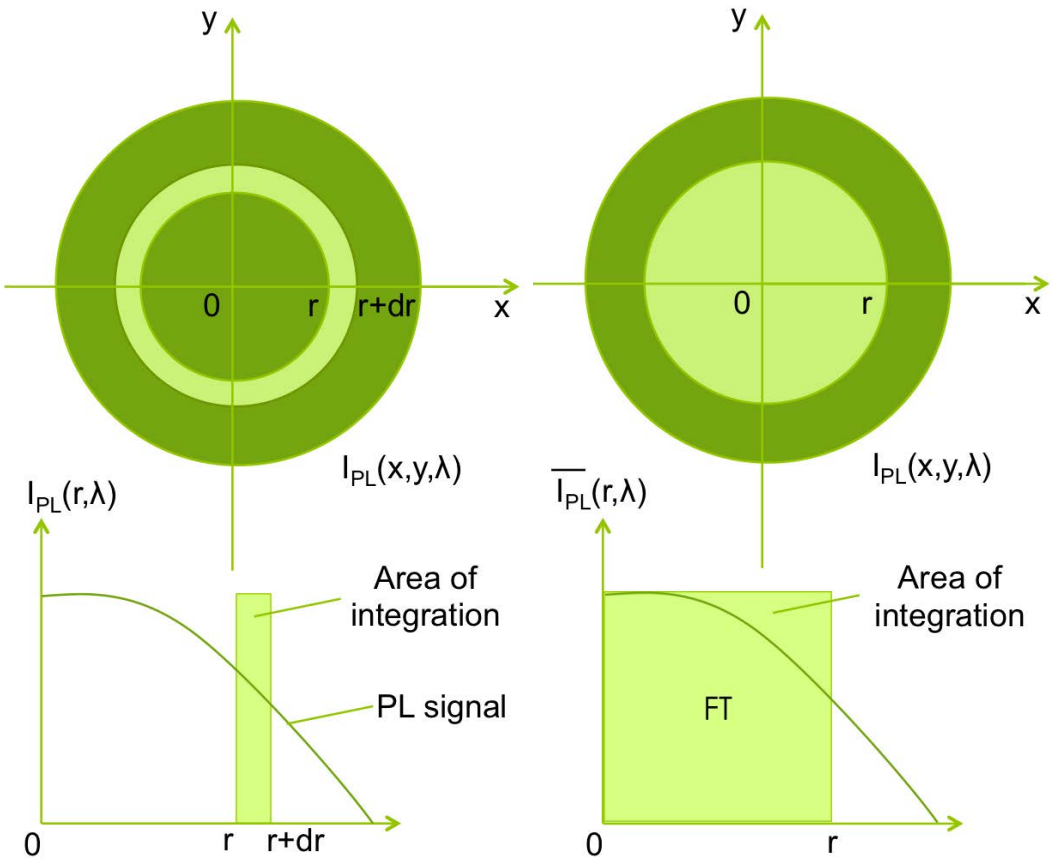


Figure 2.3 – Integration procedure to get accurate local values (a) and spatial average values (b) of the PL spectrum as a function of radius

It is therefore the equation of a surface area average of the PL intensity for each radius r. It is plotted in Fig. 2.3b, PL signal is represented in green and the average area in light green.

In order to determine the collection area of the confocal we need to match the shape of the average HI PL spectra with the confocal PL spectrum for the same absorbed power. It will be detailed in the next section.

Confocal collection area determination thanks to carrier temperature

We have seen in section 2.2.3 that the confocal set-up makes a spatial integration of the PL signal. Thus, in order to get average thermodynamic quantities in confocal mode the first step is to determine the spatial area of integration (i.e. the collection area). As we will see, the comparison of temperature of emission between confocal and HI allows to determine it. Indeed, temperature measurement does not require

absolute intensity measurements as it is extracted from the slope of the PL spectrum from Eq. (2.5). Therefore, as we measured temperature of emission for both set-ups we can compare the results. With the HI, we followed the method described in section 2.2.3, where a spatial integration of PL data is made for different rays and absorbed powers. Thus we get for each absorbed power PL map and each surface area of integration an averaged PL spectrum and therefore an effective temperature of emission. Then we can directly compare the results to confocal measurements in Fig. 2.4. It represents the temperature of emission of confocal measurements (black dots) and HI (green lines) at different mean absorbed powers. Each line represents the temperature of emission of a given integrated surface area for different powers. It means one absorbed power corresponds to one experiment. The radius of integration in the legend is normalized by illumination radius R_{spot}. The green lines are extracted from the central value ($0R_{spot}$) to 3.8 R_{spot}. One can see that the radius of integration increases when the temperature of emission decreases. This corresponds to the decrease of the temperature as we draw away from the center. Temperatures measured with confocal set-up increases from 370 K to 1170 K at respectively 2800 and 130000 suns. If one looks at the trend of the curve, we can see that the second, third and fourth points do not follow the global trend. It comes from the experiment uncertainty. However we could estimate the radius of collection in confocal at 2.5 times the illumination radius. In order to validate our measurement, we imaged the hemisphere of both the illumination spot and the collection area (inset bottom right). The central spot is the illumination spot and the ring correspond to the extremity of the collection area. The radii length match with the one we extracted from the temperatures measurement.

The experiment started only at 2800 suns in confocal due to limited detection capacity of the set-up. One can wonder if the value of 370 K is not overestimated. Therefore we decided to perform EL measurement. Indeed, EL generates quasi homogeneous illumination (in the case of a low sheet resistance value) of the collection area at a lower injection regime. Consequently, we will get a higher photons number detected at a low absorbed power. One can see the resulting luminescence spectra in the Fig. 2.5. Three green dotted curves corresponds to PL spectra at different absorbed powers and one results from EL (black) at 2 suns equivalent. From this measurement, EL gave a temperature of emission of around 300 K (room temperature) validating the temperature reliability in absence of hot carrier. Thus, the lowest extracted emission temperature of 370 K at 2800 suns in Fig. 2.4 is not overestimated.

From these measurements we could get the collection area, which corresponds

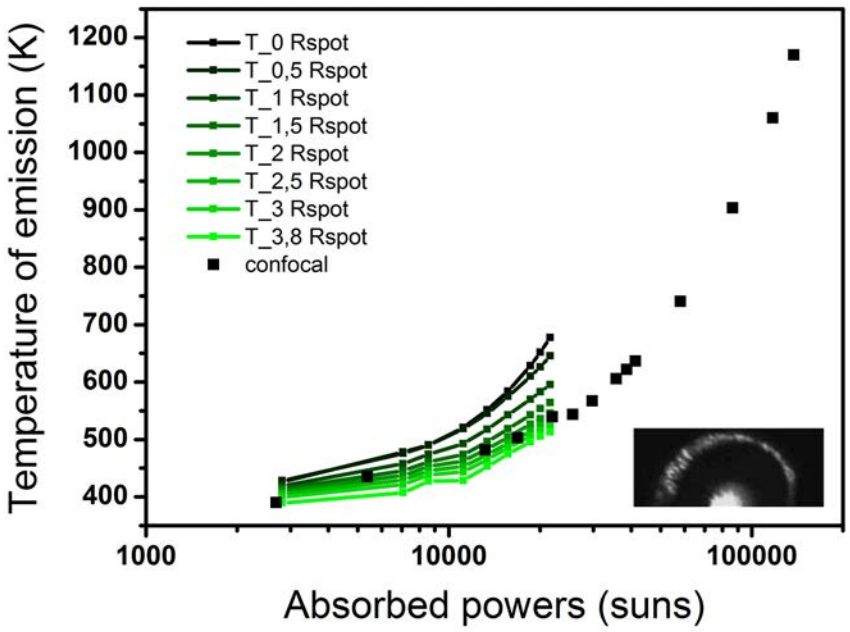


Figure 2.4 – Determination of the collection area of confocal set-up based on the comparison between confocal (black squares) and HI (green dotted lines). The figure represents the temperatures of emission as a function of the absorbed power. Remark that for each absorbed power, one data acquisition was made. Then, the data were integrated spatially. Legend indicates the radius of integration area, in units of illumination radius, which grows from 0 to 3.8 R_spot (black to green). Hemisphere image of the illumination spot and collection area in the bottom left inset

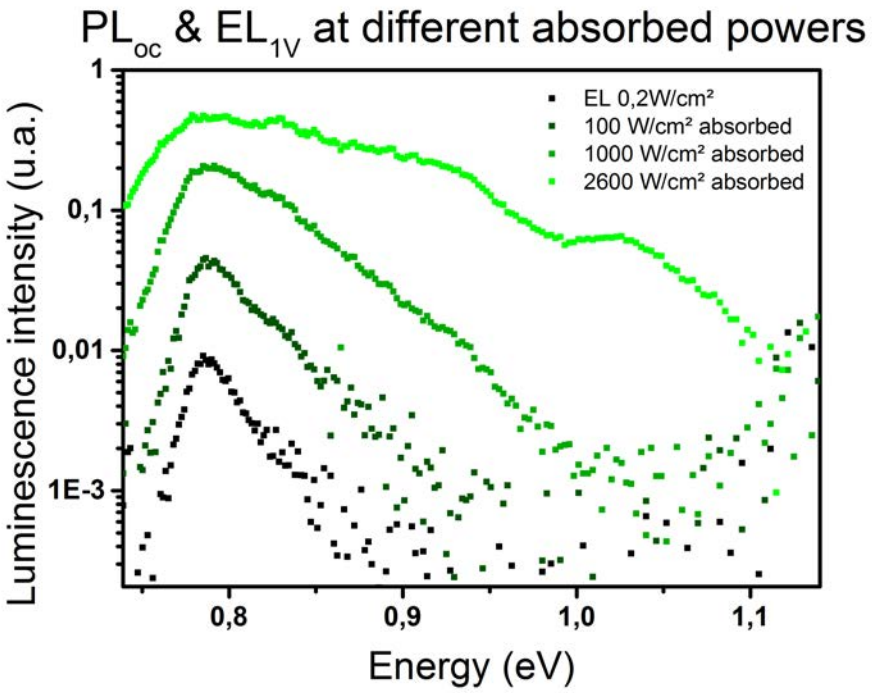


Figure 2.5 – Comparison between EL and PL measurement

to 2.5 times the illumination radius and EL validates the temperature of emission measurement reliability.

$\Delta\mu$ calibration of confocal

The aim of the subsection is to show that we can absolutely calibrate confocal spectra thanks to HI one. Indeed, knowing the spatial emitted flux in HI allows to calibrate the relative emitted flux on the confocal collection area for similar experimental conditions. Therefore we can write that the PL intensity in confocal mode equals up to a multiplicative constant the HI one:

$$I_{PL}^{HI}(\Delta\mu_{HI}, T_{HI}) = C \times I_{PL}^{conf}(\Delta\mu_{conf}, T_{conf}) \tag{2.9}$$

Remember the generalized Planck's equation, under the Boltzmann approximation writes as:

$$I_{PL}(\hbar\omega) = \alpha(\hbar\omega) \times \frac{\Omega n^2}{4\pi^3\hbar^3 c_0^2} \times (\hbar\omega)^2 \left(\exp - \frac{\hbar\omega}{k_b T_{e-h}} \exp \frac{\Delta\mu}{k_b T_{e-h}}\right) \tag{2.3}$$

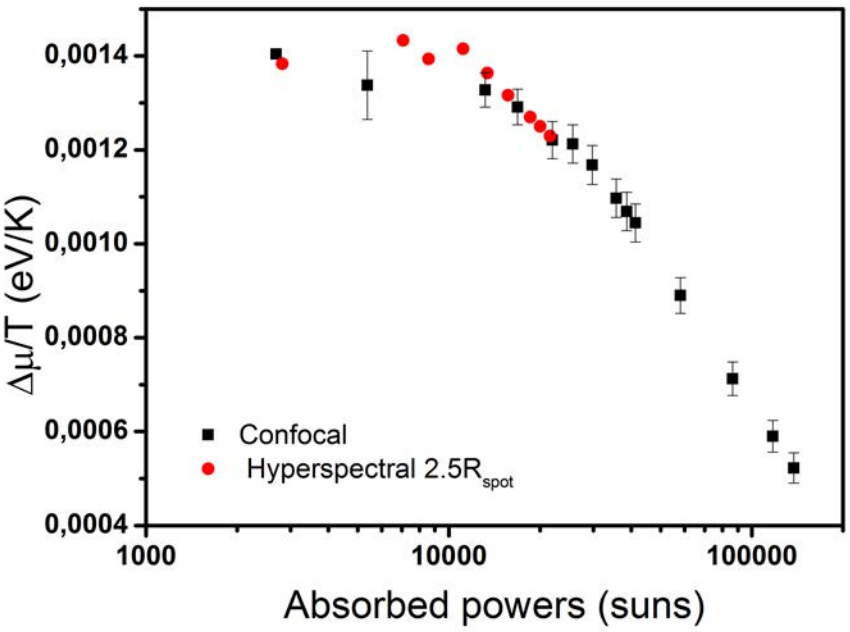


Figure 2.6 – $\Delta\mu/T$ as a function of the absorbed powers plotted for recalibrated confocal (black squares) and HI (red dots) data thanks to the relation Eq. (2.11) and a -0.10185 constant

Therefore the Eq. (2.9) can be simplified as:

$$\begin{aligned} I_{PL}^{HI}(\Delta\mu_{HI}, T_{HI}) &= C \times I_{PL}^{conf}(\Delta\mu_{conf}, T_{conf}) \\ \Rightarrow \exp\left(\frac{\Delta\mu_{HI}}{k_b T_{HI}}\right) &= C \exp\left(\frac{\Delta\mu_{conf}}{k_b T_{conf}}\right) \\ \Leftrightarrow \frac{\Delta\mu_{HI}}{k_b T_{HI}} &= C' + \frac{\Delta\mu_{conf}}{k_b T_{conf}} \end{aligned} \tag{2.9}$$

The C' constant will be determined from different absorbed powers measurements, in order to increase the constant fitting accuracy Fig. 2.6. The aim is to minimize the difference between the HI average absolute $\Delta\mu_{abs}^{HI}/T^{HI}$ and the confocal relative $\Delta\mu_{rel}^{C}/T$ as a function of the mean absorbed powers (Fig. 2.6). This is done by subtracting a constant (0.010185) to the relative $\Delta\mu_{rel}^{C}/T$ (black squares) and therefore linking the two set-ups intensities.

One can see that the alignment is satisfying at high powers although at lower powers the result suffers from experimental uncertainties.
From each emitted PL spectra in confocal we can deduce the absolute $\Delta\mu$ keeping similar conditions than that used to get the C' constant. Consequently, one can

write:

$$\frac{\Delta\mu_{conf}^{abs}}{k_b T_{conf}^{abs}} = C' + \frac{\Delta\mu_{conf}^{rel}}{k_b T_{conf}^{rel}} \tag{2.10}$$

Remember that the temperature is obtained in absolute units or without a calibrated PL spectrum therefore $T_{conf}^{abs} = T_{conf}^{rel}$. Thus, the absolute $\Delta\mu$ is:

$$\Delta\mu_{conf}^{abs} = \Delta\mu_{conf}^{rel} + C' T_{conf} \tag{2.11}$$

In this section, the set-ups and the calibration method have been introduced. It was shown that we could extract local or averaged thermodynamic quantities, which is a requirement to get the performances of the device in the absence of ESC. The next step is therefore the presentation of the samples on which we will work.

2.3 Samples description

We have seen that thermalisation was slower in MQWs than in bulk materials in section 1.2.2. However, no study was done on a batch of MQWs samples with various parameters. We have chosen samples based on InP substrate. On the one hand these structures are particularly well mastered and understood as laser diode or photo-detector. Thus, it will facilitate interpretation and simulation. On the other hand, we wanted structures without Sb or Al content in order to get a high chemical stability over time [66].
All the structures we studied and characterized were grown at the laboratory FOTON-INSA (Rennes, FRANCE) by MBE, [67, 68, 69, 70].

2.3.1 General sample diagramm

Our samples have a general structure based on MQWs with extended barriers surrounded by claddings, see Fig. 2.7. We will define below the role of the different part of the sample.

Claddings

The importance of the claddings is the confinement of photo-carriers generation. If one illuminates the sample below the energy band gap of the claddings and above the barriers one, the generation will take place only in the MQWs region (extended barriers and MQWs). The photo-carriers recombination will be depth limited and consequently their high concentration will be maintained. We expect it to lower the cooling rate as shown in section 1.2.2.

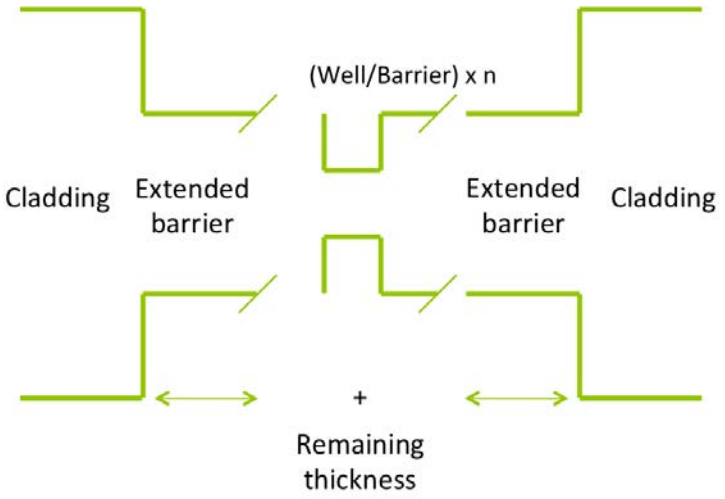


Figure 2.7 – Simplified band diagram structure of samples studied

Extended barriers

Extended barriers have a double interest. Firstly, it increases the absorption. Extended barriers and barriers of the MQWs will act as a reservoir of carriers which will recombine in the QWs. The carrier density will strongly increase from barriers to QWs. As increasing carrier density is known to increase the hot carrier effect, we expect an improved hot carrier effect in these structures compare to classical MQWs. Secondly, if claddings are doped and polarized, extended barriers will spread the voltage drop all over the MQWs, reducing electric field and Stark effect [71]. Thus, the PL emission should not be shifted with the applied bias.

2.3.2 InGaAsP multi-quantum wells

MQWs structure depends on many parameters such as barrier width, well width, number of wells, materials... We decided to work on InGaAsP MQWs because this material is known to have a dominant radiative recombination over Auger effect even at high injection regime [72]. Moreover, quaternary materials are highly content tunable. A continuous panel of lattice matched material can be used on InP, from InP (1.27 eV) to $In_{0.53}Ga_{0.47}As$ (T0.47) (0.76 eV) at 300K.

2.3.3 Samples parameters and performances

Thermalisation reduction was shown on samples without really being the fruit of an intentional design of material parameter, see section 1.2.2. Therefore, there is a need to characterize a wide set of various MQWs. The aim of this subsection is to establish a correlation between sample performances and MQWs parameters.

Acronym	Material composition
Q1.6	$In_{0.78}Ga_{0.22}As_{0.81}P_{0.19}$
Q1.4	$In_{0.66}Ga_{0.34}As_{0.733}P_{0.267}$
Q1.18	$In_{0.8}Ga_{0.2}As_{0.44}P_{0.56}$
T0.47	$In_{0.53}Ga_{0.47}As$
T0.34	$In_{0.66}Ga_{0.34}As$

Sample number	Barrier/Well composition	Well number	Well width	Barrier width	Remaining thickness	Total thickness	PL peak	PL intensity	Well tension modulation by P concentration (cc)
4467	Q1,18/T0,47	6	7,5	10	50	155	1601	**	
4473	Q1,18/T0,47	6	6,5	10	50	149	1582	**	
4476	Q1,18/T0,47	6	5,5	10	50	143	1560	***	
4487	Q1,18/T0,47	3	5,5	10	50	96,5	1556	***	
4535	Q1,18/T0,34	6	3	10	50	128	1563	***	
4536	Q1,18/T0,34	6	5	10	50	140	1566	***	
4587	Q1,18/Q1,4	5	12	10	190	300	1334	***	5
4588	Q1,18/Q1,4	5	12	10	190	300	1373	***	4
4589	Q1,18/Q1,4	5	12	10	190	300	1418	***	3
4675	Q1,18/Q1.6-1%	6	7	10	50	152	1598	***	5
2757	Q1,18/Q1.6-1%	5	7,4	10	250	337	1598	***	5

Table 2.1 – Parameters of the samples

Firstly, we will introduce the samples that were used. Secondly, their performances will be determined and then a statistical study will allow us to analyse the results. Thirdly, key parameters of the performance will be identify from the statistical model.

Samples presentation

Samples with different well thickness, composition, constraint, number of wells were used, keeping the general structure introduced in Fig. 2.7. The specificities of the samples are gathered in Tab. 2.1. Note that the second column "barrier/ well composition" presents acronyms, which are defined at the top of Tab. 2.1. Letters and numbers of the acronym means respectively quaternary (Q) or ternary (T) and the wavelength of emission in microns of the material. As one can see in the table, most of the samples are very different. It makes the comparison between each other very difficult.

Sample performances

The performances of the samples are evaluated thanks to determination of the thermalisation rate from the following experiment.

Experimental analysis Experiments consist in PL spectra acquisition as a function of absorbed powers thanks to the confocal set-up defined in section 2.2.1 at 300

Sample number	Thermalisation rate (Q in W/K/cm^2)	Well number	Well width (nm)	Well tension modulation by P concentration (cc)
4467	43,3	6	7,5	0
4476	7,9	6	5,5	0
4487	14,2	3	5,5	0
4535	14,8	6	3	0
4536	4,9	6	5	0
4587	10,3	5	12	5
4588	7,2	5	12	4
4589	9,4	5	12	3
4675	18,7	6	7	5
2757	24	5	7,4	5

Table 2.2 – Table of sample performances through thermalisation rate and temperature of emission in QWs. Key parameters of performances are also added. They were identify thanks to the statistical method.

K. Then PL spectra are fitted thanks to Eq. (2.5), previously introduced:

$$\ln\left(\frac{I_{PL}}{A(\hbar\omega)\times(\hbar\omega)^2}\right) = a\times\hbar\omega + b \tag{2.5}$$
$$\text{where : } a = -(k_b T_{e-h})^{-1} \text{ and } b = \frac{\Delta\mu}{k_b T_{e-h}}$$

Fitting ranges were adjusted on both regions, where the absorbance does not vary according to the absorbed power and at high energy enough from the transition energy so the Boltzmann approximation is valid. Thanks to the determination of temperature of emission and absorbed powers, we could extract thermalisation rate from:

$$P_{th} = Q(T_{e-h} - T_l)\exp\left(\frac{\hbar\omega_{LO}}{k_b Te - h}\right) \tag{1.3}$$

The thermalisation rates were gathered in Tab. 2.2, which range from 4.9 to 43.3 $W/K/cm^2$. Thus, the best sample (lowest Q) is 4536. Considering the number of sample parameters, their differences and that no analytical model links the parameters with the thermalisation rate we performed a statistical study.

Statistical method

Interest of the study The aim of the study will be to find a generalized linear model (GLM) on thermalisation rates according to the sample parameters. GLM fits experimental data D thanks to a polynomial, limited in this study at the second order such as:

$$D(x_i, x_j) = a_0 + \sum_i a_i x_i + \sum_j b_j x_j^2 + \sum_{i,j} c_i x_i x_j \tag{2.12}$$

with a_i, b_i, c_i fitted parameters, and x_i, x_j the input parameters (material one). The relevance of the fitted values a_i, b_i, c_i is evaluated by analysis of variance (ANOVA). The best fit is obtained when the R-square (multiple correlation coefficient) of the model is satisfactory (R-square>80%) and the model contains only statistically significant input parameters. Some statistical softwares provide this method of analysis. Among them, we used JMP software [73].

Method The method was the following: all the potential parameters x_i influencing thermalisation rate were implemented without prejudices from Tab. 2.1. Parameters, which had a negligible influence on the fit were eliminated. Then, we included the second order of each parameters x_j^2 step by step and checked the resulting GLM quality. At last, we included the second order of the product of the parameters $x_i x_j$ between each others step by step in order to include their interactions. For each simulation, we tried to maximize the R square of the model in order to increase the quality of the fit.

Model and key parameters

Both minimization of R square and number of parameters allow to find a GLM with a R square of 0.98 for the thermalisation rate, see Fig. 2.8, which writes as:

$$\begin{aligned} Q =& a_0 + a_1 w_w + a_2 w_n + a_3 w_t \\ &+ b_1 (w_w - k_1)^2 + b_2 (w_n - \overline{w_n})^2 + c_1 (w_w - \overline{w_w}) \times (w_n - \overline{w_n}) \end{aligned} \tag{2.13}$$

with a_i, b_i, c_i are the fitted coefficient. $\overline{w_n}$ and $\overline{w_w}$ are respectively the mean well number and width of the samples. A first interesting result is that the parameters of influence are only geometrical parameters (well width, well number, well tension). Indeed, we tried to use many parameters (indium content, absorbance, and all the parameters mentioned in Tab. 2.1) for GLM and geometrical parameters gave the best result. One has to keep in mind that the conclusion will only be valid in this studied sample domain.

We will not discuss the fitted coefficient values but only their sign, which are gathered in Tab. 2.3 (third column). Moreover, fitted coefficient can be rendered dimensionless, which allows to compare them. Thus, stars in the column "influence" represent the value of dimensionless fitted coefficient in relative units. One can see the most important one, applies on the product of well number and well width (8 stars). Therefore, total thickness of the wells (well width $\times$ well number) has a

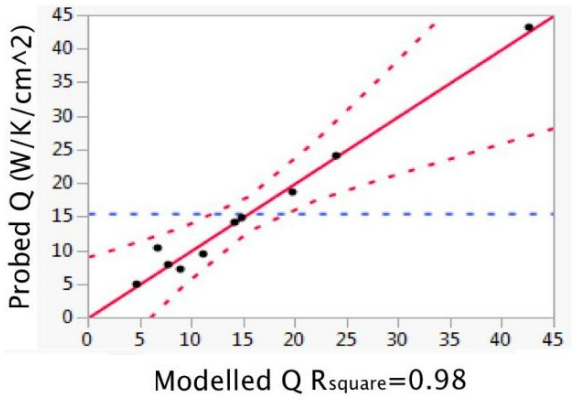


Figure 2.8 – GLM fit of thermalisation rate where the probed quantities are represented as a function of the modelled one. Dots represents the probed value whereas red line correspond to the fit. Blue dash lines are the mean probed quantity and red dashed lines are the confidence interval

Material parameters	Fitted coefficient name	Fitted coefficient sign	Influence
Well width	a_1	-	*
Well number	a_2	+	**
Well tension	a_3	-	-
(Well width)²	b_1	+	***
(Well number)²	b_2	-	***
Well width x Well number	c_1	+	********

Table 2.3 – Table gathering the key material parameters found by GLM fitting; their related coefficient (name, sign and influence) are added.

strong influence on thermalisation rate. As coefficient c_1 is positive, Q increases with the total wells thickness. Remind that the lower the thermalisation rate, the higher the performances.

In a second order, the two other parameters, which impact the thermalisation rate (3 stars) are the squares of the well width and well number. The square of the width will increase the thermalisation rate whereas the square of the number will decrease it. Therefore, it could be interesting to get a sample with numerous narrow wells keeping in mind the total thickness should be low (for instance < 30 nm, corresponding to the best sample 4535). However, narrow well imply high energy transition and therefore weak carrier confinement. The structure would be bulk-like, i.e a "classical" solar cell. Another solution would be to rely on the main parameter of influence (total thickness of the well) making a one well structure. The fabrication of such a sample is on the way. One has to keep in mind that the GLMs and our conclusion are valid if one stays in the range of samples parameters we have used.

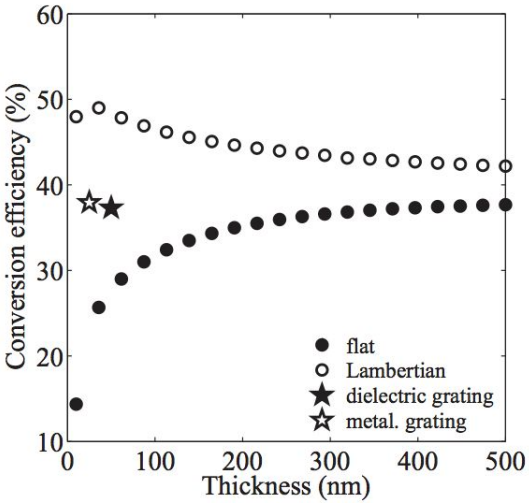


Figure 2.9 – Conversion efficiency as a function of the absorber thickness for a flat absorber (filled circles) and in the Lambertian limit (empty circles) under a 10 000 times concentrated AM1.5D solar spectrum. The efficiency is found to be monotonously decreasing with the absorber thickness in the case of a flat absorber, but an optimal thickness of about 50 nm is observed, giving a maximal efficiency of 50%, in the Lambertian limit. The efficiencies obtained with the dielectric grating (filled star) and with the plasmonic grating (empty star) are also reported. The thermalisation coefficient Q is taken 10 $W/K/cm^2$ for a 200-nm-thick absorber. Figure extracted from [11]

Thickness influence on thermalisation rate

The fact that the thermalisation can be reduced thanks to the use of MQWs instead of bulk material has been seen. The absorber thickness reduction associated with a constant carrier generation will increase the carrier concentration and therefore saturate more easily the LO-phonon emission [50]. Accordingly, hot phonons will be reabsorbed by carriers and slow down the thermalisation. The thickness impact was studied thanks to HCSC modelling in [74]. The thermalisation rate was taken proportional to the thickness t according to [11]: $Q = Q_0 t/t_0$, with Q_0 the thermalisation rate at thickness t_0. It was shown the thickness reduction is effective if the absorption is high enough and if the thermalisation rate is already low, see in Fig. 2.9. Two structures were proposed to maximise the light concentration in the thin absorber based on nano-photonic and dielectric gratings.

It was seen in this section that a sample with a low thermalisation rate was obtained (4.9 $W/K/cm^2$). Then, that a statistical study was a requirement so as to understand thermalisation rates of the samples, which presents various parameters and no related physical model. Then, the total thickness of the absorber was found to be a crucial parameter, showing a linear influence on the thermalisation rate, in

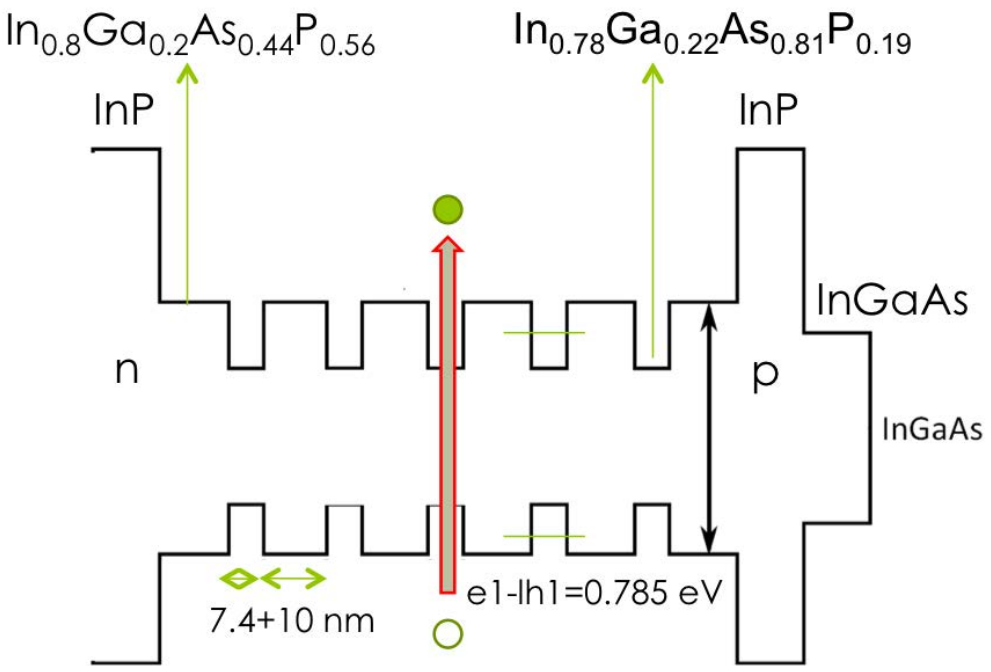


Figure 2.10 – Simplified band diagramm of sample 2757

agreement with [75]. At last, we proposed the fabrication of a one well sample to get a very low thermalisation rate.
All these samples were undoped except the sample 2757. We will see it provides an important advantage to go further on hot carrier properties analysis. The sample will be detailed in the next section.

2.3.4 Detailed description of the bipolar device

Sample introduction The sample 2757 was initially used as a laser emitting diode at 1.55μm Telecom wavelength. It has the same general structure than the previous undoped samples except it is bipolar. Claddings surrounding intrinsic MQWs region are n and p doped. The sample is represented in Fig. 2.10, which is a schematic of the energy band diagram of the sample according to the depth (not to scale). The composition and the doping are also indicated. The layers will be illuminated from the right to the left and the photo-carrier generation will take place mainly in the barrier (red arrow).

The complete device and layers are represented in Fig. 2.11. Materials, doping rate, thickness and energy band gap are indicated from left to right. The colours represents the different doping type: p (green), n(brown), intrinsic (white), metallic (orange). The additional layers compared to the previous schematic are here for

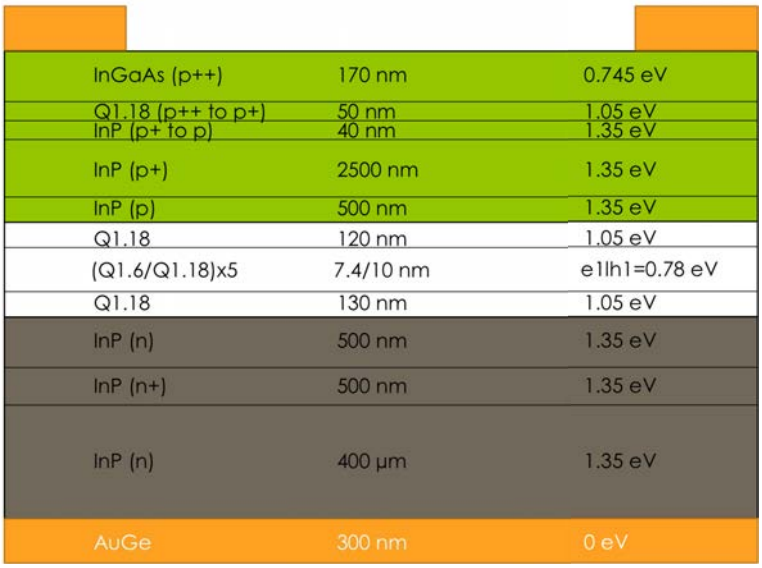


Figure 2.11 – Layers representation of the sample 2757 associated to doping, thickness and band gap from top to bottom

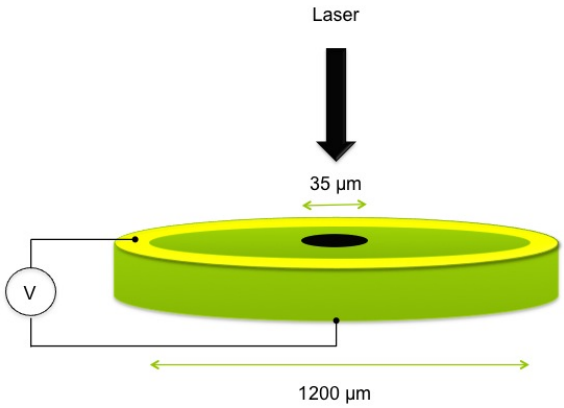


Figure 2.12 – Schematic of PL under electrical bias experiment

their electrical role. They ensure ohmic contact on metallic layer. Moreover, all the structure has a doping and composition gradient in order to minimize contact resistivity and layers accumulation charges.

Taking electrical contacts for PL under bias measurements in confocal mode PL under applied bias required electrical contacting. The rear contact (AuGe, Fig. 2.11) was taken on all the rear plate, whereas the front contact was micro-welded such as described in the schematic in Fig. 2.12. Micro-welding was inevitable given that the front contact area was very narrow and the IR objective we used had a small working distance (1 cm).

2.4 Absorbance simulation and measurement

In order to get a better understanding of the bipolar sample 2757, we will study its spectral absorbance. Indeed, we have seen that the extraction of $\Delta\mu$ requires a quantitative measurement. However, one has to keep in mind throughout study that the absolute errors on temperature and $\Delta\mu$ due to relative absorbance error can be written as:

$$dT = \frac{k_b T^2}{E}\frac{dA}{A} \tag{2.14}$$

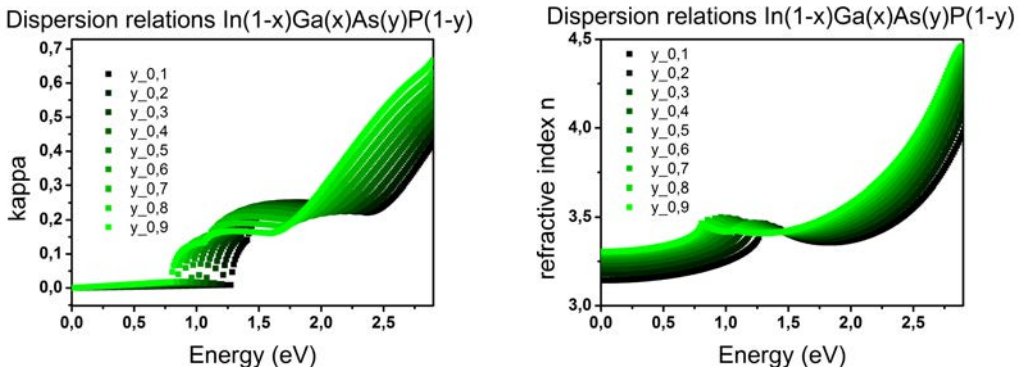
$$d\Delta\mu = k_b T\frac{dA}{A} \tag{2.15}$$

Therefore, the absolute error on the temperature and $\Delta\mu$ will be respectively of 5K and 0.010 eV for a 50% relative error on absorbance. For more details on measurement errors, please refer to appendix section C.
In some conditions the measurement of absorbance is not possible (absorption by front layers, rear metallic surface). Therefore, firstly modelling absorbance will be done in the active region (MQWs and extended barriers). Secondly, we will model the transition energy of the MQWs. Thirdly, we will compare simulated and experimental EQE. Quantum efficiency measurement EQE(E) can be also very useful experimentally, as it is equal up to a constant (collection factor) at the absorbance A(E).

2.4.1 Modelling optical indices

n and k modelling

Sample 2757 is composed of four different types of materials: InP, T0.47, $In_{0.66}Ga_{0.34}As$ (T0.34) and $In_{1-x}Ga_xAs_yP_{1-y}$. Spectral dependence of the optical indices in InP, T0.47 and T0.34 are well known [76, 77]. However, our specific compositions of InGaAsP cannot be found in the literature. Therefore, modelling optical indices is a prerequisite before modelling the aborbance. Thus, using S. Adachi's model [78] based on identification of critical points associated with Kramers-König relations, we modelled the spectral and composition dependence of the dielectric functions. Then real and imaginary part of the refractive indices are extracted from



(a) (b)

Figure 2.13 – Real and imaginary part of the refractive indices as a function of photon energy for different $In_{1-x}Ga_xAs_yP_{1-y}$ compositions

dielectric functions:

$$n = \sqrt{\frac{\sqrt{\epsilon_1^2 + \epsilon_2^2} + \epsilon_1}{2}} \tag{2.16}$$

$$\kappa = \sqrt{\frac{\sqrt{\epsilon_1^2 + \epsilon_2^2} - \epsilon_1}{2}} \tag{2.17}$$

with respectively n and κ the real and imaginary part of the refractive indices.

ϵ_1 and ϵ_2 are the real and imaginary part of the dielectric function. Considering a lattice matched $In_{1-x}Ga_xAs_yP_{1-y}$ material on InP substrate, the composition variation is limited by [78]:

$$x = \frac{0.1896y}{0.4176 - 0.0125y} \tag{2.18}$$

The resulting indices are plotted over a wide spectral range from 0 to 2.9 eV in Fig. 2.13.

The real part of the refractive index Fig. 2.13b increases from 3.2 to 4.2 in the visible range as predicted by Adachi's model [79]. κ is related to the absorption coefficient Eq. (2.19):

$$\alpha = \frac{4\pi\kappa}{\lambda_0} \tag{2.19}$$

with λ_0 the wavelength in the vacuum.

The Fig. 2.13a directly provides the band gap for different compositions. As the arsenide composition (y) increases, $In_{1-x}Ga_xAs_yP_{1-y}$ compound approaches to the $In_{0.53}Ga_{0.47}As$ composition, i.e. to a smaller band gap. These observations associated with S. Adachi results [79] validates our modelling.

2.4.2 Simulated absorbance properties

In this section we will use the commercial simulation software Silvaco. This software can calculate not only optical properties but also electrical ones. The point is: we can directly compare our experimental results (EQE) with the simulation. Indeed, optical measurement of the absorbance are influenced by front layers. In the following section, the words in capital letters corresponds to Silvaco syntax (to ease the reproduction of our simulations).

Software parameters of simulation In order to check our simulation results, we started by defining only the multi-quantum wells region. It was done using the implemented model based on Adachi's calculations, which deduces the energy band parameters of InGaAsP according to quadratic interpolation of the corresponding binary compounds. We checked the Silvaco band parameters values thanks to a matlab code (ZincBlendeIIIV.m), which provides fundamental material parameters from similar quadratic interpolation of the binaries made by T.Mei [80]. The results were in good accordance. Then, from these band diagrams, we decided to use the implemented general QWs model (QWELL statement) so we can get the QWs energy states. Secondly, a Ishikawa constraint model was added in the wells (ISHIKAWA statement). As the constraint has an effect on heavy and light holes, the general QWs model requires the calculation of two valence bands (ZB.TWO statement).

Band diagram and QWs transitions We could also calculate the bands diagram of the MQWs and its extended barriers. The band diagrams are plotted as a function of the depth of the sample in Fig. 2.14. It is constituted of valence and conduction bands for bulk and well transitions. As the materials have direct band gaps, we only plotted the energy bands in the center of the Brillouin zone Γ. Two bulk valence bands are represented: one for the heavy holes (#1, light blue) the other for light holes (#2, orange). One can see the heavy hole valence band #1 is pushed away in the bulk continuous density of state due to the strain in the MQWs. Only one conduction energy band exists for the electrons (#1, red). From these bulk energy bands, the calculation of the quantized states have shown single state in each band, which represents the transition energy e1-lh1 at 0.78 eV (e1=green, lh1=dark blue). The simulation gives a slight difference of energy transition of roughly 0.01 eV if we relate it to the PL peak. Thus, we have chosen to adjust the strain in the sample simulation as it is a difficult parameter to adjust during growth. We changed

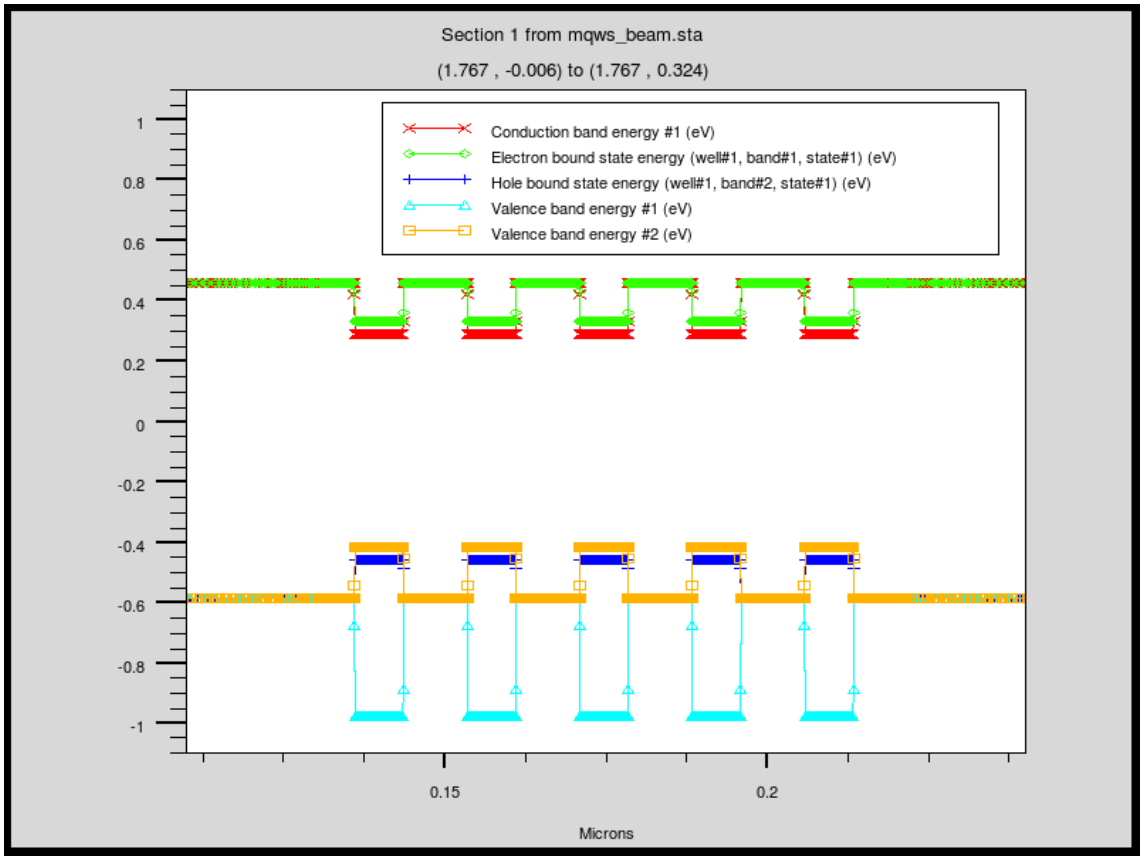


Figure 2.14 – MQWs transitions energy of sample 2757

it from initially 1% to 1.2%. Let us reminder that the strain is defined as followed:

$$\text{Strain}(\%) = \frac{a - a_0}{a_0} \tag{2.20}$$

with respectively a and a_0 the strain lattice parameter and the unstrain one.

2.4.3 Absorbance calculation

Software parameters of simulation From the QWs energy states calculation we can deduce the internal absorbance (neglecting reflexion and interferences). Indeed, we decided to simulate only the intrinsic part of the device (barriers and extended barriers) so we can simply see the MQWs absorbance. The absorbance is directly calculated from the energy transition (ABS QWELL statement), which solves a Schrodinger-Poisson system of equation. However, prior to the calculation, the complex refractive indices of the QWs bulk material and the barriers must be added. As no suitable refractive indices is implemented for InGaAsP we employed the one we calculated in section 2.4.1 thanks to the user-definable statement "F.NKEG".

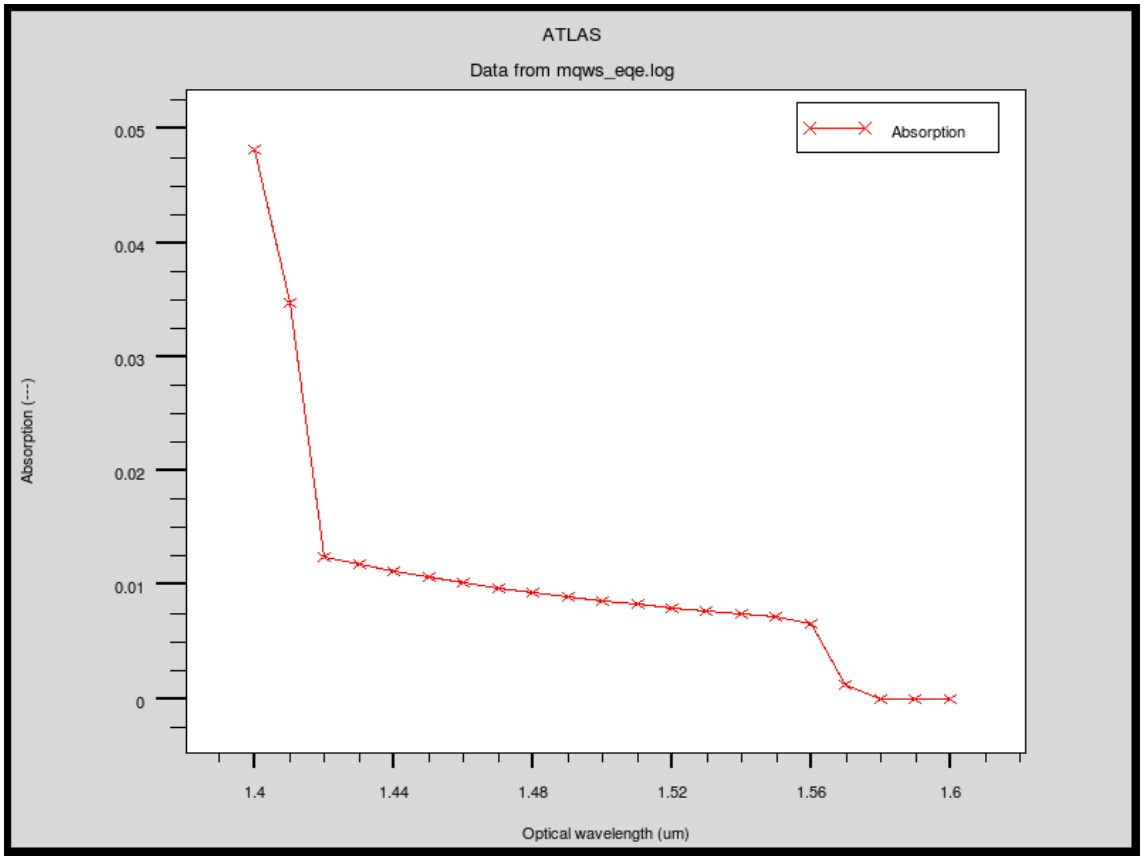


Figure 2.15 – Absorbance of the intrinsic part of the sample 2757

Absorbance calculation As a part of photo-carriers will recombines by emitting PL in the MQWs region (extended barriers and MQWs), we calculated the absorbance of this region. It will firstly give an approximate absorbance value because front layers reflection and interferences are not taken into account; even though we expect low losses from layers reflections as the real refractive indices are close between each others. Secondly, it will allow us to compare the absorption value (without interferences) with the external quantum efficiency measurement. Thus the fraction of photo-carriers collected electrically will be known. The Fig. 2.15 represents the absorbance as a function of the optical wavelength. One can see two absorption thresholds at 1580 nm and at 1420 nm, which correspond respectively to the energy transition of the MQWs and the beginning of the barriers absorption region. The absorption is almost constant between the two thresholds, which shows we can fit the temperature of emission thanks to the generalised Planck's law neglecting the absorption variation in this spectral range. At last, let us keep in mind the mean absorption value calculated in the wells is of 0.7%.

This section allowed us to see our thermodynamic study on hot carrier will concern a single transition well and that the spectral absorbance variation is low in

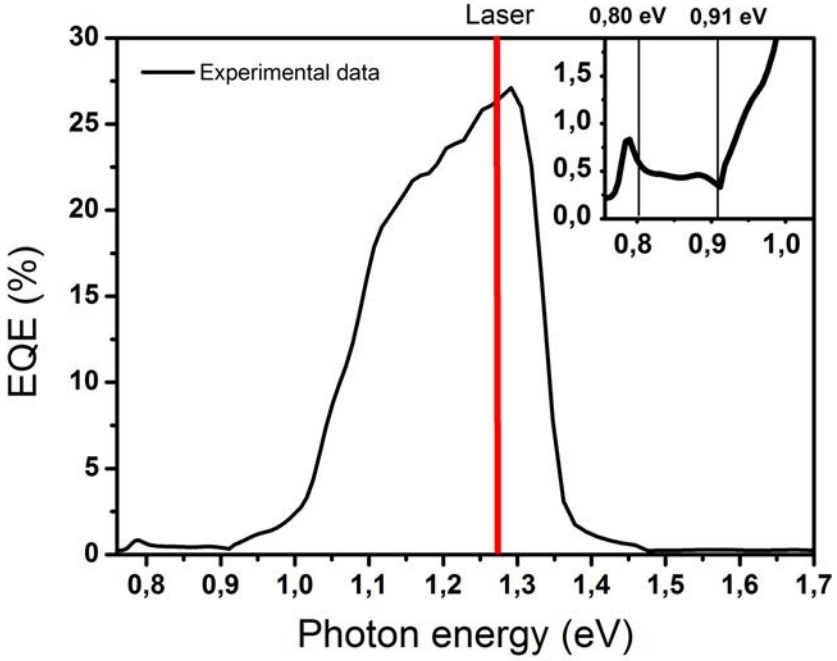


Figure 2.16 – EQE of the sample 2757

the QWs. We decided to perform an EQE measurement so we can compare it to the absorbance value we got in the previous simulation. It would not be possible to do it on an undoped samples (EQE requires electrical contacts), which validates our sample choice.

2.4.4 Measurement of EQE and its effect on PL spectra

Simulated and experimental external quantum efficiency

The usefulness of the EQE measurement is to have experimental outlook of the sample. EQE measurement is plotted in Fig. 2.16, where three regions can be distinguished. Firstly, from 0.78 to 0.91 eV one can observe the relatively constant step-like e1-lh1 transition mentioned in the previous paragraph with a mean value of 0.5 %. It represents a maximum 30% relative difference between EQE and the absorbance. This discrepancy can be due to the electrical collection of photo-carriers in the wells at short circuit regime, which seems quite efficient. Secondly, an another threshold corresponds to the absorption of the barriers at 1.05 eV. The EQE is about 50 fold higher than in the MQWs, which is expectable as the barriers and extended barriers thickness is about one order magnitude higher than the QWs. At last, the front InP layer plays a cut-off filter role at 1.35 eV.

EQE could be simulated thanks to Silvaco, see Fig. 2.17. The simulation was

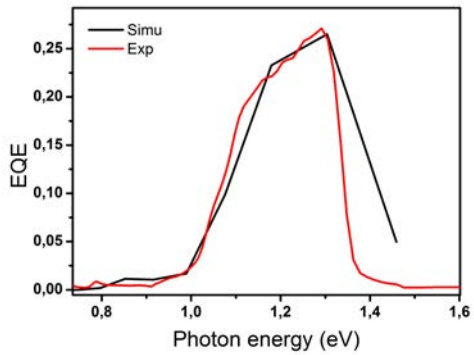


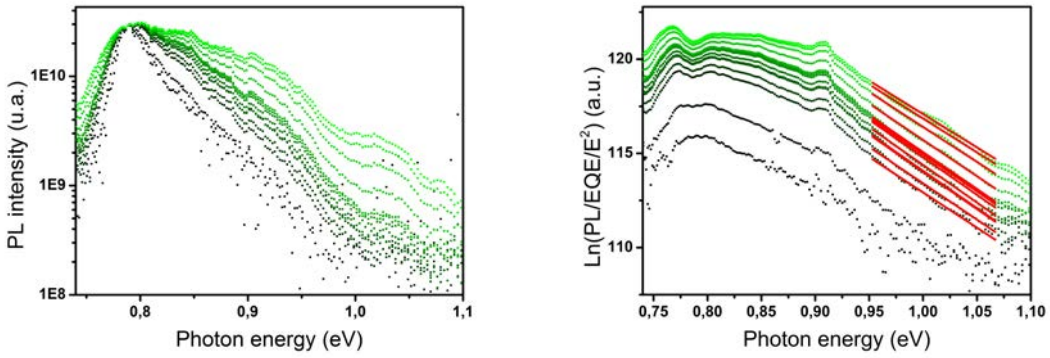
Figure 2.17 – Simulated and experimental EQE as a function of the incident photon energy (eV) on sample 2757.

averaged on intervals of 100 nm due to both the strong interferences generated by the numerous layers of the device, and the resolution of the set-up. The simulation allows to validate our previous absorbance simulation, as there is a good agreement between the experimental and the simulated one (signone point each 0.1 eV).

From these results, firstly we will set the PL spectrum fitting bounds from 0.82 to 0.91 eV where the EQE shows a plateau (vertical black lines, inset of Fig. 2.17) with an absorbance value of 0.5%. Secondly, as the sample will be illuminated at 975 nm (1.27 eV), we will set the absorbance value at 26% (vertical red line on 2.16). This value is crucial in order to determined the absorbed power and then the thermalisation rate. Probing it experimentally is then very useful and could not be done with undoped samples. Remark that these parameters are very important, as they will be used all along the thesis.

Correlation between PL spectra and absorbance

We have seen there are strong variations of the spectral absorbance on the sample 2757 except in the MQWs. Therefore, if one observes the normalized PL spectra in logarithmic scale at different absorbed powers, we can see that each spectral variation of the EQE affects the PL spectra (Fig. 2.16,Fig. 2.18). In order to exceed the absorbance variation and get the thermodynamic quantities, one can use the Eq. (2.5). Therefore, the PL spectrum transformation should only give one slope at high photon energy proportional to $1/T_{e-h}$. Using the EQE instead of the absorbance in previous equation and plotting it in Fig. 2.18b shows there is two slopes. One corresponds to the wells (from 0.82 to 0.91 eV) the other to the barriers (beyond 0.95 eV). This is a very interesting result because thanks to



(a) (b)

Figure 2.18 – Normalized PL and fonction of PL

the EQE measurement we are able to distinguish two thermodynamic quantities according to the spectral region. On the one hand, as absorption variation are low in the well region, we will use a constant value of 0.5% for absorbance and set the fitting range from 0.82 to 0.91 eV so the EQE does not add supplementary noise. On the other hand, for the barriers of the well, the fitting range will be set between 0.95 and 1.07 eV and the EQE will be used as absorption data.

As seen previously, the temperature can be determined directly from a linear fit of PL spectra, whereas $\Delta\mu$ requires absolute measurement. Thus, $\Delta\mu$ can be extracted according to Eq. (2.5), see Fig. 2.19.

For each spectral region we divided the data by its temperature and one can observe a constant $\Delta\mu$ on the spectral region of interest, which validates the procedure. Indeed, thermodynamic constants are independent to the photon energy, in each material (well or barrier). The discussion on the results themselves will be led in the next chapter.
As a conclusion of this section, thermodynamic quantities can be measured either in the single transition wells or in the barriers. Therefore, we will use the EQE measurement as the absorbance component in the generalized Planck's law from 0.95 to 1.07 eV for the barriers of the MQWs. For the MQWs, as the absorbance is flat from 0.82 to 0.91 eV we will use a constant value of 0.5%. At last, according to the EQE we determined the absorbance at the laser wavelength (26%), which will be used to link the incident power flux to the mean absorbed power.

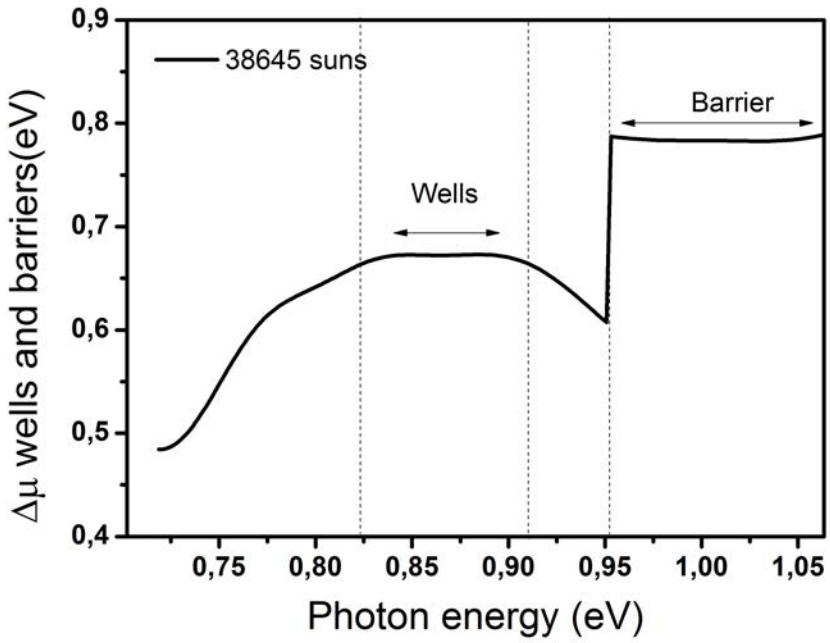


Figure 2.19 – $\Delta\mu$ as a function of the photon energy extracted from Eq. (2.5). $\Delta\mu$ was calculated according to the emission temperature of the QWs from 0.72 to 0.95 eV and to according to the emission temperature of the barrier from 0.95 eV to the end. The dashed lines represents the intervals on which each $\Delta\mu$ were extracted.

2.5 Hot carrier device simulation

Hot carrier device simulation is an undeniable asset for the experimental understanding. Thus, we will introduce the software we used and its architecture.

2.5.1 Introduction to numerical balance equations software

Principle of the software

The MATLAB software was developed by A. Le Bris [8] and modified so we can simulate as closely as possible our device and experiments. The numerical software is based on energy and current balance equations resolution where we extract without any approximation on carrier distributions (Fermi-Dirac distributions) the temperature of emission, $\Delta\mu$, current and efficiency according to the applied external bias on a hot carrier absorber surrounded by non ideal selective contacts in presence of carriers thermalisation.

The balance equations can be written as two variables functions of the temperature of emission and $\Delta\mu$, which in steady-state cancel each others (see chapter 1). The numerical resolution of this pair of equation allows to calculate the solar cell characteristic and therefore its conversion efficiency.

The solar cell will be defined by its energy band gap E_g, its thermalisation rate Q, the concentration of the incident light C, and three parameters linked to the selective contacts: the energy extraction E_{ext} (difference between electrons and holes extraction energies), the conductance G of the contact and the selectivity of the contacts δE.

Architecture of the software

The software is composed of two blocks:

- Initialization: the user defines the external physical quantities such as: sun temperature or laser emission energy, ambient temperature, concentration factor... Then material parameters are defined (band gap of the absorber, phonon energy, thermalisation rate...) and at last, the device parameters are added (selectivity, conductance...). In this initialisation part of the software, the user will define the parameter he wants to study: the variable on which a conversion efficiency optimisation of the other parameters will be done (conductance and extraction energy). In this study, the optimisation is not relevant as device parameters are the sample ones.

- System resolution: the system resolution is done by the numerical research of balance equations cancellation at an external applied bias. As the bias is fixed, $\Delta\mu$ and the temperature of emission are directly extracted so the charge and energy conservation is satisfied. Therefore, the power and current provided by the cell is acquired as a function of each bias. The operation is repeated at each change of main variable defined. At each step, the research of the optima of conductance and extraction energy is performed, if required.

Conclusion In this chapter, we have seen steady-state photoluminescence spectrum provides useful thermodynamic quantities. HI and confocal set-ups allows to determine it thanks to the method we developed. Then, the samples have shown good thermalisation rate ranging from 4 to 40 $W/K/cm^2$. Their thermalisation rate presented a linear dependance on the absorber thickness in agreement with our article [75]. At last, a specific absorbance study was made on the bipolar sample, which will be studied in depth, in the next chapter.

Short summary - Characterization of HCSC absorber is a first requirement in order to estimate performances and potential efficiencies. As selective contacts are still an on going research field, a device characterization based on contact-less method is necessary. Identifying the hot carrier effect can be done by luminescence study. We have chosen steady-state PL, because it is close to operating solar cell conditions regarding excitation conditions and time scale. Additionally, by fitting PL spectra we can extract pertinent thermodynamical quantities such as lattice temperature, carrier temperature and $\Delta\mu$. These quantities can be measured thanks to both our confocal and HI set-ups. HI brings a spatial and an absolute $\Delta\mu$ whereas confocal has the advantage of rapidity and simplicity of use. Hence, a flux calibration method of confocal set-up was developed. A batch of samples were studied and performances were qualified. We identify that the absorber thickness is a key parameter and therefore a one-well structure should present a very low thermalisation rate. A specific sample, 2757, was selected regarding its strong advantages of being a bipolar device and having a low enough thermalisation rate. In this respect, the sample allows us to go further in the optoelectronic characterization in the chapter 3.

CHAPTER 3

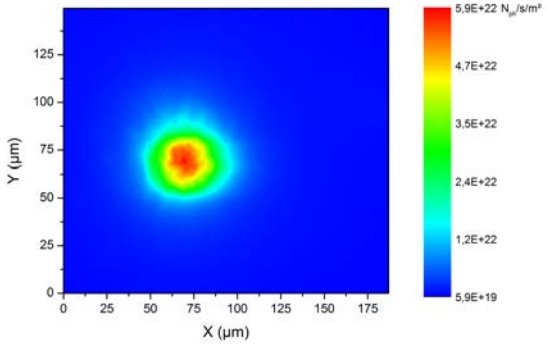
Quantitative optical measurement of hot carrier effect

3.1 Evidence of performance under-estimation by local measurements

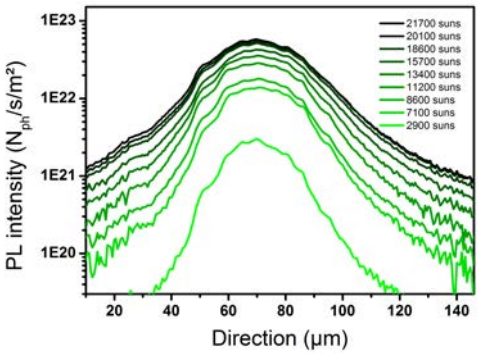
We will see how local measurements of absolute PL spectra is a key point in order to understand finely the hot carrier phenomena. The absolute measurements couple to the spatial resolution allows us to measure thermodynamic quantities ($\Delta\mu$ and T_{e-h}) and therefore estimate hot carrier potential performances.
Firstly, we will point out the ability of the HI set-up to probe absolute spatially resolved PL spectra on the bipolar device made of InGaAsP MQWs (2757).
Secondly, we will show the first local measurements of temperature of emission and $\Delta\mu$.
Thirdly, we will see that the carrier diffusion has to be taken into account in the real device performances measurements.
At last, we will open the study by demonstrating that the sample behaves as a "photothermoelectric" device and that thermoelectric performances can be acquired.

3.1.1 Probing absolute PL map

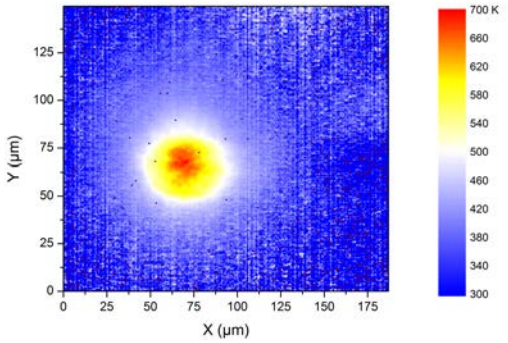
On the one hand, we will study absolute spatially resolved PL spectra for different illumination powers. On the other hand, we will see how the photo-carriers diffusion follows the increase of the absorbed power. We will see that because of



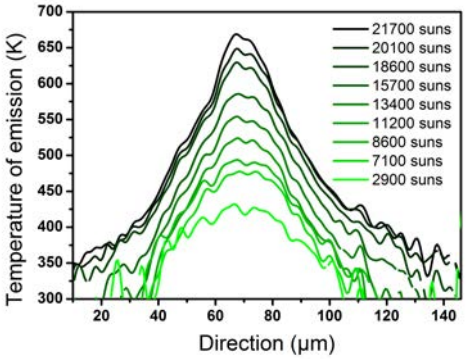
(a) Spectrally integrated PL map of the sample 2757 under 22000 suns illumination



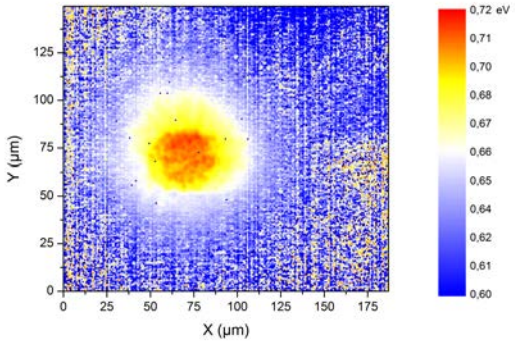
(b) Spectrally integrated PL along X direction at Y=Barycenter of the left corresponding map at different illumination powers



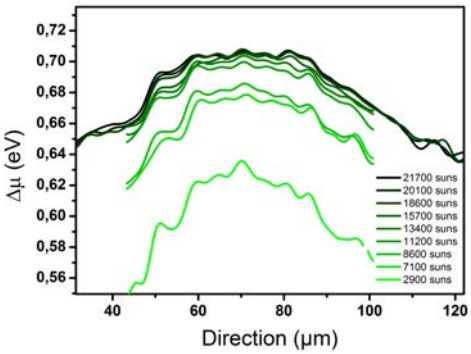
(c) Temperature of emission of the sample 2757 under 22000 suns illumination



(d) Temperature of emission along X direction at Y=Barycenter of the top/left PL map at different illumination powers



(e) $\Delta\mu$ of the sample 2757 under 22000 suns illumination



(f) $\Delta\mu$ along X direction at Y=Barycenter of the top/left PL map at different illumination powers

Figure 3.1 – Thermodynamic quantities extracted from spatially resolved PL spectra. Maps (left) and profiles at different powers (right) of spectrally integrated PL intensity (a,b), temperature of emission (c,d) and $\Delta\mu$ (e,f).

the inhomogeneous illumination, lateral diffusion must be taken into account in the local absorbed power determination.

Absolute PL maps As it was seen in section 2.2.2, the bipolar sample 2757 (section 2.3.4) is illuminated thanks to a 975 nm multimode laser. The resulting PL signal is then acquired by the HI set-up, which provides the map display in Fig. 3.1a where the emitted photons flux is measured in absolute unit ($N_{ph}/s/m^2$). This value reaches 6×10^{23} $N_{ph}/s/m^2$ at the center and decreases quite monotonously as one draws away from the center. We have plotted the corresponding profile of integrated PL for more clarity in Fig. 3.1b. The chart represents the profile as a function of X direction at the Y barycentre of the map for different absorbed powers. The line starts from green and turns to black as the absorbed powers increases.
Two elements can be discussed: the intensity in accordance with the power at the center, and the carrier diffusion. Firstly, we expect the PL intensity to be linear with the absorbed power and observed it in Fig. 3.2a:

$$I_{PL} \propto \exp(\Delta\mu) \propto P_{abs} \tag{3.1}$$

In addition, so as to observe the lateral carrier diffusion, spectrally integrated PL profiles were normalised by their maximum, see Fig. 3.2b. Then, full width at 50% integral was extracted and plotted in the inset of the figure. One can see the width increases linearly with the absorbed power from 16 to 23 μm. The effect of lateral hot carriers diffusion has never been observed optically. Consequently, we will see that if one wants to get the real performances of the device, it has to be taken into account.

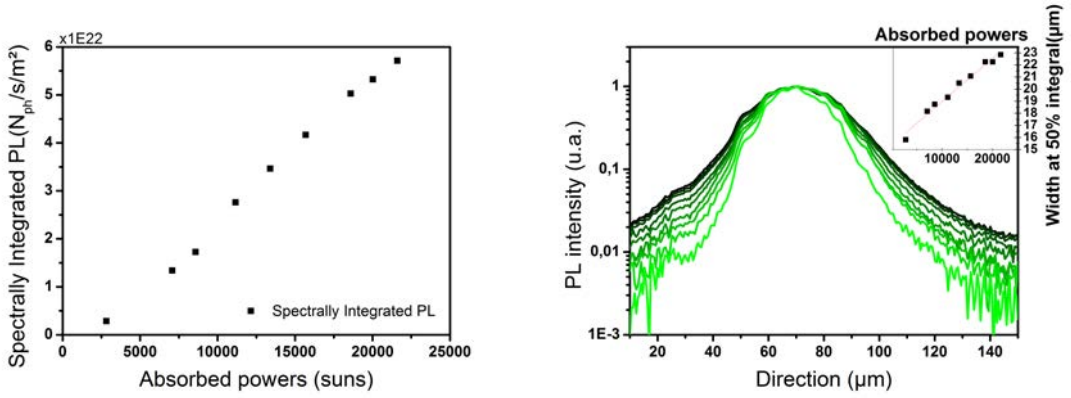
Taking into account the photo-carriers diffusion can be done by determining the local absorbed power without diffusion, which requires the energy flux balance equation:

$$\frac{\partial J_Q}{\partial t} = P_{abs} - P_{em} - P_{th} - P_{el} - div(\overrightarrow{J_Q}) \tag{3.2}$$

with J_Q, P_{abs}, P_{em}, P_{th}, P_{el}, which are respectively locals energy flux, absorbed power, radiative emitted power, thermalisation power, and the electrical power.

As the laser is continuous, the steady-state condition applies $\frac{\partial J_Q}{\partial t} = 0$. Moreover, the study is done at open circuit regime, hence the electric power P_{el} is zero. Thus the balance equation rewrites as:

$$\frac{\partial J_Q}{\partial t} = 0 = P_{abs} - P_{em} - P_{th} - div(\overrightarrow{J_Q}) \tag{3.3}$$



(a) (b)

Figure 3.2 – (a) Spectrally integrated PL at barycentre of the maps as a function of the absorbed power. (b) Normalized spectrally integrated PL along X direction at Y=Barycenter of the left corresponding maps for different illumination powers (from green to black). Inset: Full width at 50% integral of PL peaks as a function of the absorbed powers (black dots).

The aim is to get the local absorbed power $P_{abs} - div(\overrightarrow{J_Q})$, but we just know the spatial integrated absorbed power $P^I_{abs} = \alpha \times P_{laser}$. This value can be compared to spatial integrated emitted power P^I_{em}, which can be calculated thanks to HI absolute measurement:

$$P^I_{em} = \int\int\int I_{PL} \times EdEdXdY \tag{3.4}$$

To that end, one can plot spatial integrated emitted power P^I_{em} as a function of the absorbed powers P^I_{abs} in Fig. 3.3a. Firstly, there are about 4 order of magnitude between the two. Thus, one can neglect the local emitted power compared to the local absorbed power and Eq. (3.3) is simplified as:

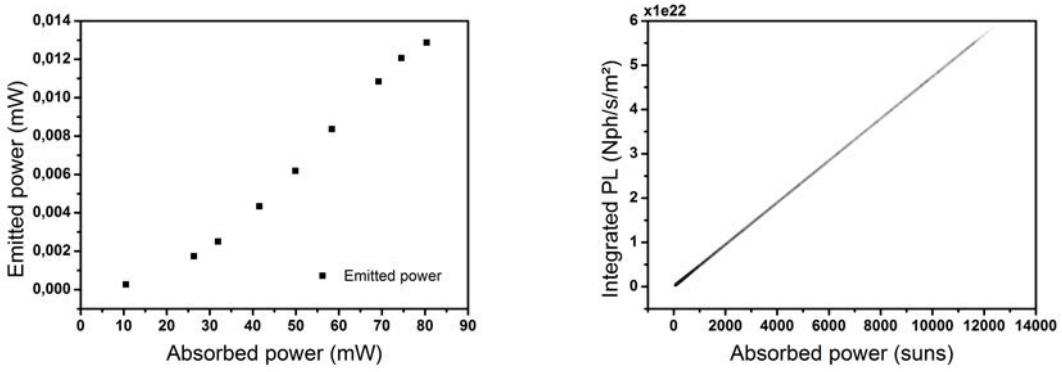
$$P_{th} = P_{abs} - div(\overrightarrow{J_Q}) \tag{3.5}$$

The local thermalised power equals the local absorbed power after carriers diffusion.

Secondly, the figure shows that the quantities are quasi-linear. Hence, one can consider that the local absorbed power, after carriers diffusion, is proportional to the local emitted power:

$$P_{abs} - div(\overrightarrow{J_Q}) = K \times P_{em} \tag{3.6}$$

This method can be applied because radiative recombination is the slowest phenomenon after carrier-carrier scattering, electron-phonon scattering, and Auger re-



(a) (b)

Figure 3.3 – Radiative emitted power (a) and integrated PL (b) as a function of the local absorbed power calculated from Eq. (3.6) (b). Sample 2757, $\lambda_{spot} = 975\,nm$.

combination as we saw insection 1.2.2.
In other words, from the the PL intensity map we could to determine the local absorbed power without diffusion. Consequently, we can plot the spectral integrated PL map as a function of the local absorbed power one (without diffusion) in Fig. 3.3b. The maximum value reaches 14000 suns at $6 \times 10^{22}\, N_{ph}/s/m^2$. Let us remind that the initial mean absorbed power, which was calculated from illumination spot area and the spatial integrated power was of 22000 suns equivalent. This power decrease is due to the increase of area of photo-carriers distribution.
These local absorbed powers values will be widely used to take into account the lateral diffusion while calculating further thermodynamic quantities.

3.1.2 Local Temperature

We have seen we can probe the local absorbed powers and take into account the lateral diffusion. Starting from this result, we will first show the ability of the set-up to probe local temperature of emission. Then, we will measure the thermalisation rate parameter and deduce the potential efficiency of our sample.

Local temperature determination Temperature of emission was introduced in section 2.1.2 and its extraction is based on the PL spectra fit using the generalized Planck's law Eq. (2.5). In this equation, the absorbance term has to be taken into account to ensure the validity of the measurement, see section 2.4.4. In such a way, PL spectra at each pixel of the HI provides a local temperature Fig. 3.1c. One can see the temperature of emission reaches more than 650K at the center of the map for a mean absorbed power of 22000 suns. Similarly to the integrated PL map

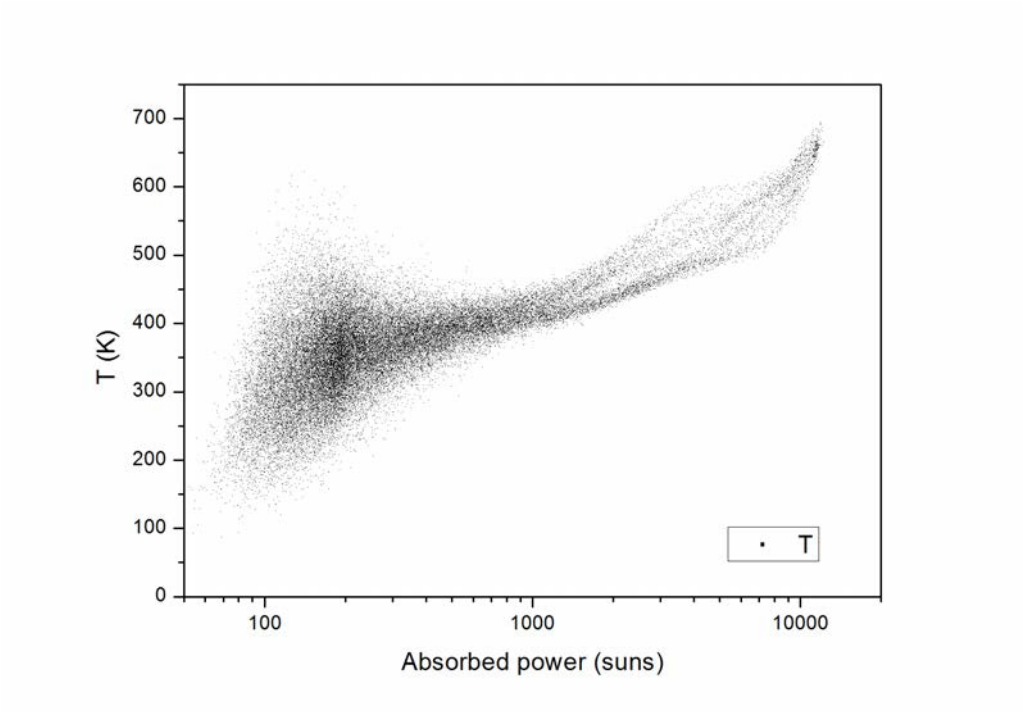


Figure 3.4 – Temperature of emission of the sample 2757 for different absorbed powers from hyperspectral data

Fig. 3.1a, the temperature decreases homogeneously as we draw away of the center. We can plot the temperature profiles to have a better insight in the temperature gradient. The Fig. 3.1d represents the temperature of emission as a function of X direction at the Y barycentre of the PL map. The darker the line, the higher the mean absorbed power. As the absorbed power increases, one can observe that the width of the plateau at the center decreases (i.e the peak gets shaper), whereas the temperature on each side of the peak increases. The consequence of these two effects is that the FWHM stays constant whatever the absorbed power (baseline at 300 K). These effects come from both of the temperature dependence on the power (Eq. (1.3)) and the carrier diffusion.

In order to avoid it, one can use the local power determine in previous section. Thus, one can have a better idea of the relation between the absorbed power and temperature Fig. 3.4. The graph represents the local temperature of emission as a function of the local absorbed power (mean absorbed power of 22000 suns). Each dot corresponds to a pixel of the HI map (Fig. 3.1c). Thus, one can see that the overall tendency is an increase from 350 to 670 K at respectively 100 suns and 14000 suns. If one extends the scatter diagram to low absorbed powers, the temperature approaches 300 K, which validates our measurement. For the highest local powers, the highest temperature of 670 K corresponds to the center of the map. Considering

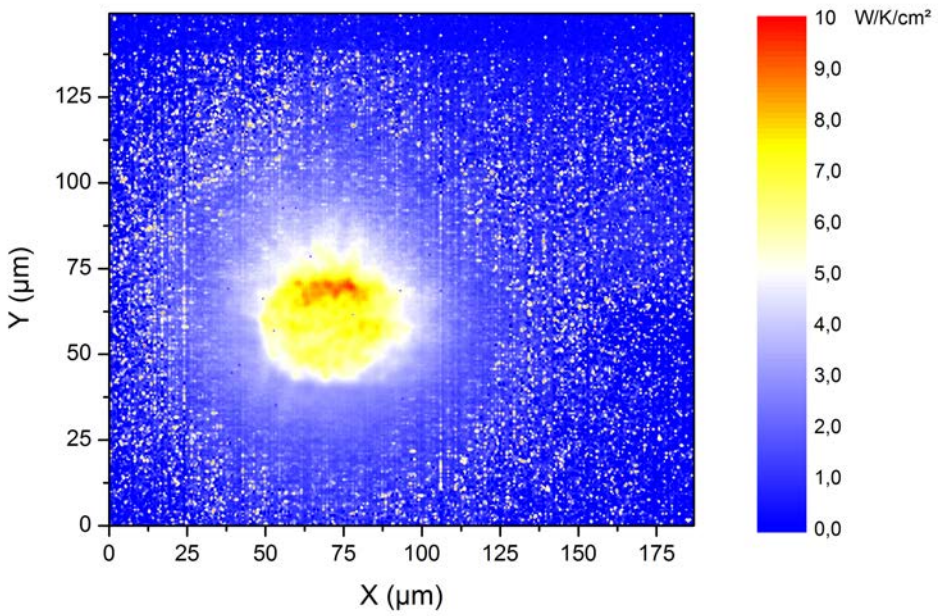


Figure 3.5 – Local measurement of the thermalisation rate deduced from a absorbed power map based on integrated PL map and the corresponding local temperature map of emission under 22000 suns

that the experiment is performed at room temperature, under achievable sunlight concentration and continuous excitation, this value is very high. It constitutes the highest hot carrier temperature probed in continuous wave regime at room temperature. Compared to the literature, Le Bris *et al.* found a temperature of emission of 270 K (continuous regime, 80K sample temperature,mean absorbed power 10000 suns), see [11]. It represents a 190 K elevation above sample temperature, thus, at similar power, our increase of 370K is very promising (InGaAsP MQWs). In pulsed regime at room temperature, the highest temperature (1200K) was observed by Pelouch *et al.* in GaAs/AlGaAs QWs, 100 fs after excitation [46]. After a 1 ps delay of the pulsed laser excitation (generating a 2e18 cm-3 density), they found a temperature of emission of 510 K. The temperature went down to 350K after 5 ps delay.

Local thermalisation rate So as to understand distinctly the sample performances, one can extract the thermalisation rate (Q), see section 1.2.2. It facilitates the comparison of samples. The local value of Q is calculated directly from the local power map and the emission temperature according to the equation seen in chapter

1:

$$P_{th} = Q(T_{e-h} - T_l)exp\left(\frac{\hbar\omega_{LO}}{k_bTe - h}\right) \tag{1.3}$$

It is plotted spatially in Fig. 3.5. The value at the center is close to 7 $W/K/cm^2$. It decreases to 4 $W/K/cm^2$ as one draws away from the center. As we expect a constant value (material constant), we attribute the decrease to the measurement error, which increases as the ratio of signal over noise decreases. As we saw in section 2.3.3, this result is different from the confocal measurement ($24W/K/cm^2$), which is around 3 times higher. This difference can be explained as the confocal set-up makes a spatial integration of the signal, see section 2.2.3. Consequently, such studies did not take into account lateral effect and therefore overestimated the Q value, [11]. This is an important result as it means that the potential conversion efficiency is underestimated in confocal set-up. One can see it in Fig. 3.6, which represents the efficiency of a 1 eV band gap material with perfectly selective contacts for different absorbed powers [8]. If the thermalisation rate is higher than 100 $W/K/cm^2$ the conversion efficiency gets close to the Shockley-Queisser (SQ) limit and HCSC structure does not bring any added value. Nevertheless, if the rate is lower than 10 $W/K/cm^2$, the efficiency can reach 50% at maximum concentration (46000 suns), which represents 10 absolute points over the SQ limit. In this conditions, HCSC begins to have a strong interest. Our absorber of 4 $W/K/cm^2$ could even potentially reach a conversion efficiency of 60%.

We have demonstrated in this section that we could probe the local temperature of emission and that the carrier diffusion has a strong impact on it. On top of that, the performances are very high compared to the literature. As seen in section 1.2.2, most of the experiments were done at low lattice temperature or under pulsed laser excitation, which are not characterisation conditions close to solar cells operation conditions. These experimental results cannot easily be extrapolated to operating conditions, as phonon density and/or carrier density dramatically depends on characterisation set-ups, as we saw in section 2.2.1.
Finally, we have seen thermalisation rate could induced a potential conversion efficiency of 60% at full concentration, with the use of perfectly selective contacts. As the results are very promising, we will continue and evaluate a second thermodynamic quantity: the local $\Delta\mu$.

3.1.3 Local $\Delta\mu$

This section will show the importance of measuring local $\Delta\mu$ as a function of the local power. This is a unique measurement and it represents one of the major

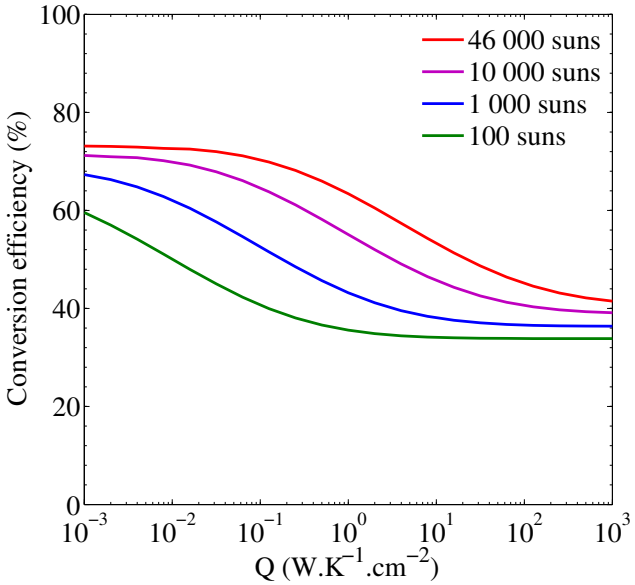


Figure 3.6 – Conversion efficiency as a function of the thermalisation rate coefficient, with a 1 eV band gap absorber and perfectly selective contacts, with concentration ranging from 100 to 46000 suns, from [8].

contribution of this thesis. As $\Delta\mu$ is the maximum open circuit voltage optically measured at 300K (see section 2.1.2), it will be compared to the so-called radiative open circuit voltage. Then, the ideal output voltage qV_{ESC} will be defined and calculated from $\Delta\mu$. At last, the potential conversion efficiency of the device will be extracted from our measurements, showing the full capability of our set-up.

Local determination of $\Delta\mu$. $\Delta\mu$ definition and role was introduced in section 2.1.2. We explained how we can probe it on classical GaAs cell by a HI thanks to its absolute calibration [63]. In this work, we want to generalize the method to our hot carrier devices. Using the method described in section 2.1 and Eq. (2.5), we can extract the absolute $\Delta\mu$ on each pixel of the map Fig. 3.1e. As $\Delta\mu$ is a thermodynamic constant, we checked there was no variation according to the photon energy (in QWs spectral range), meaning the calibration procedure, temperature fit and absorption variation were proper, see Fig. 2.19 in section 2.4.4. $\Delta\mu$ reaches 0.71 eV at the center of the illumination spot and decreases as one draws away from it. In order to see more distinctly the variation of $\Delta\mu$, the profiles were plotted in Fig. 3.1f. Once again, one can see the different profiles along the X direction at Y barycentre of the maps, which are getting darker as the mean absorbed powers increase. The strong variations observed are only due to the multi-mode laser source. At the center, $\Delta\mu$ increases from 0.63 eV to 0.71 eV as the mean absorbed powers

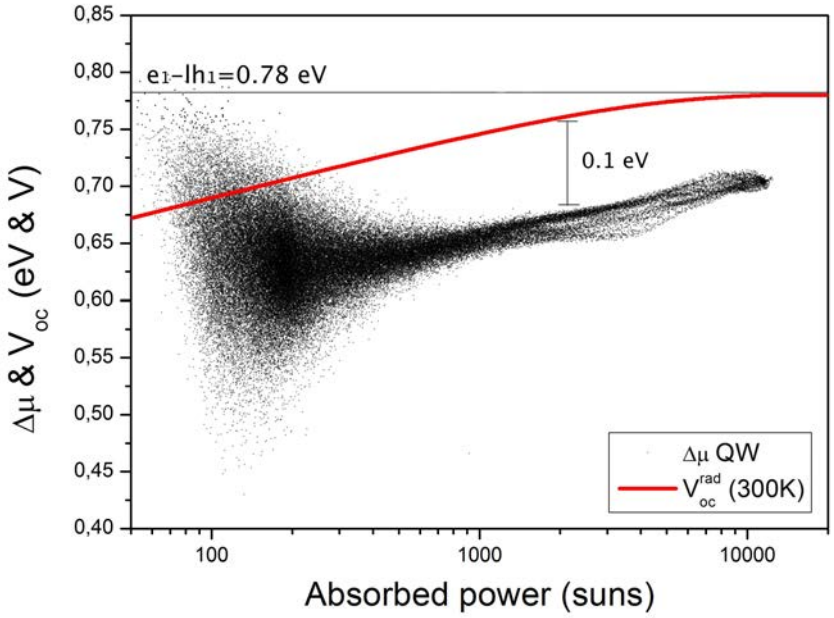


Figure 3.7 – Scatter diagramm of $\Delta\mu$ in the QWs as a function of the local absorbed power (black dots). Data were extracted from $\Delta\mu$ and local absorbed power maps acquired by HI set-up. Red line is the radiative open circuit voltage at 300 K for a 0.78 eV absorber (black straight line). Sample 2757, $\lambda_{spot} = 975\,nm$.

increases from 3000 suns to 22000 suns. The highest value is only 70 meV below the e1-lh1 energy transition at 0.78 eV. If one now focus on each side of the profiles, $\Delta\mu$ flatten as the absorbed powers increase from 3000 to 22000 suns. This is due to lateral diffusion which was observed in inset of Fig. 3.2b. Indeed, it follows $P_{abs} \propto exp(\Delta\mu)$ and $\overrightarrow{J}_Q \propto \overrightarrow{grad}(\Delta\mu)$. This will be detailed in section 3.1.4.
As we did for the temperature of emission, we can plot $\Delta\mu$ (black dots) as a function of the local power to take into account the diffusion and the local variation of local powers Fig. 3.7. The scatter diagram shows that $\Delta\mu$ increases from 0.62 eV to 0.71 eV at respectively 200 and 14000 suns. Remind the absorbed power here is the local one; as the local values are not influenced by lateral diffusion contrary to mean absorbed power. Therefore the lateral diffusion lowers the mean absorbed power considered before. One can see the strong variations induced by multimode excitation we observed on the profiles can be counterbalanced taking into account the local absorbed power.

In order to understand the impact of this result we can plot the radiative open circuit voltage at 300 K (red line) as a function of the concentration in Fig. 3.7. The radiative open circuit voltage is calculated thanks to Eq. (3.7) with J_{sc} and

J_0 the black body integrals, which includes a threshold function of the absorption beyond the energy band gap at 0.78 eV, see [81].

$$V_{oc}^{rad} = \frac{k_b T_l}{q} \times ln(1 + J_{sc}/J_0) \tag{3.7}$$

Thus, the radiative open circuit voltage grows logarithmically as the absorbed power increases until 2000 suns, then, the V_{oc}^{rad} saturates at the 0.78 eV band gap. If we compare $\Delta\mu$ and V_{oc}^{rad}, the difference remains more or less constant (around 0.1 eV).

Output voltage determination In hot carrier solar cells, as carriers are transmitted to the cold electrodes through ESC, an additional electrical potential, comes from the carrier kinetic energy. Indeed, if one wants to extract the cold electrical potential in the case of isentropic ESC, the following relation should be used, see[17, 61, 21].

$$qV^{ESC} = E_{ext}\left(1 - \frac{T_l}{T_{e-h}}\right) + \Delta\mu_h \frac{T_l}{T_{e-h}} \tag{3.8}$$

Electrical contacts can be supposed to be made by barriers of the MQWs, and so the extraction energy is its band gap energy at 1.05 eV. Thereby, we can extract an output voltage from $\Delta\mu$ and the temperature of emission in the case of isentropic ESC. The results are plotted in Fig. 3.8 as a function of the local absorbed power (black dots). V_{oc}^{rad} (red line) and $\Delta\mu$ in the QWs (green line) were added for illustration purposes. Remark that $\Delta\mu$ comes from 3.7 but it was averaged for figure clarity.

The output voltage increases logarithmically from a mean value of 0.7 eV to 0.9 eV at respectively 200 and 14000 suns. The output voltage becomes very high as it surpasses both the radiative limit at 300K and the transition energy of the well at respectively 300 and 1000 suns. The slope of the output voltage is much steeper than $\Delta\mu$ of the QWs. Moreover, if one extends both the output voltage and the averaged $\Delta\mu$ to low absorbed powers, the curves joins. At these low absorbed powers, temperature of emission is lower and the hot carrier effect gets negligible, i.e the temperature of emission is close to the lattice temperature. These observations, indicates obviously that the change of slope comes from the hot carrier. This effect will be detailed in section 3.3 by simulation results. Measuring a potential output voltage improvement on a hot carrier absorber as never been done in the literature. This is due to the absence of efficient ESC (see section section 1.2.3), which is overcome here through the use of contactless HI measurement. Additionally, this result shows the thermalisation in the absorber is no longer the limiting parameter.

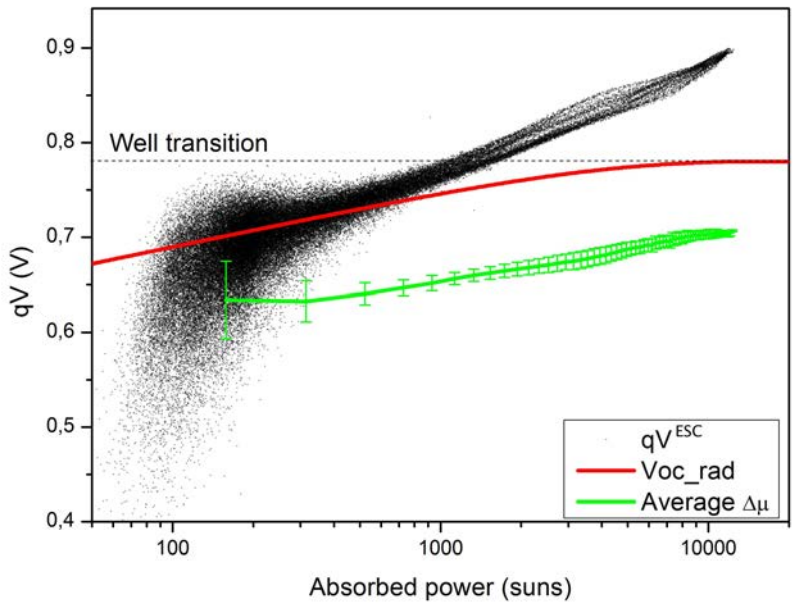


Figure 3.8 – Output voltage extracted from (3.8), $\Delta\mu$, T_{e-h}, and the barrier energy band gap 1.05 eV in the case of isentropic ESC

With a view to go further in the analysis, we can calculate the potential efficiency we would get if we had such output voltages.

Potential conversion efficiency The more suitable parameter to understand the absorber performances is the conversion efficiency. Thus, we can compare the theoretical efficiency limit of a classical pn junction to our expected device performances. To do so, the theoretical classical limit is estimated thanks to the following equation from [81]:

$$\eta = \frac{J_{sc} V_{oc} \times FF}{P_s} \tag{3.9}$$
$$\text{where : } FF = \frac{V_{oc}/k_b T_l - ln(1 + V_{oc}/k_b T_l)}{1 + V_{oc}/k_b T_l}$$

With J_{sc}, FF, P_s, which are respectively the short circuit current density, the fill factor and the incident power. In order to calculate the short-circuit current, we will consider all the photons with energy higher than the energy band gap to be absorbed.

In the case of a HCSC the conversion efficiency is also the the product of the short circuit current, the FF, and open circuit voltage, but here the open circuit voltage

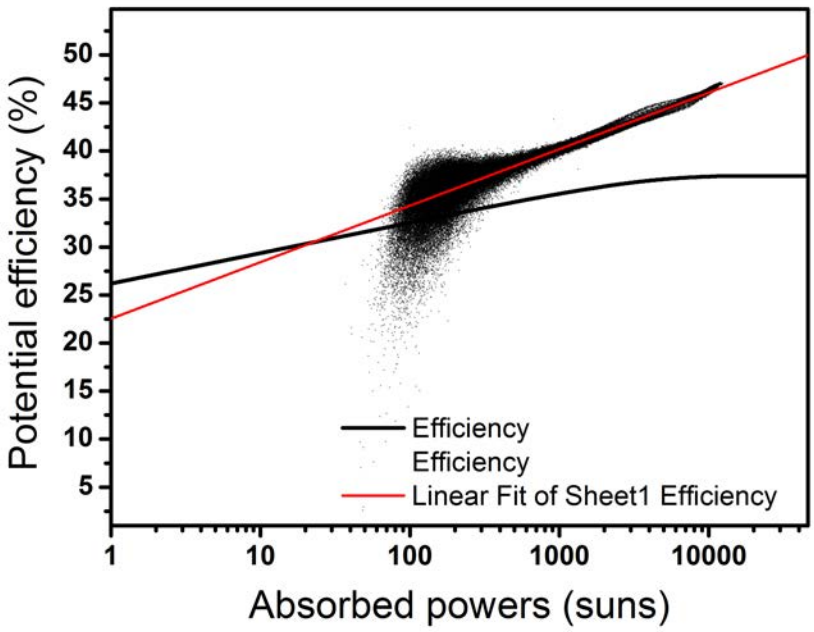


Figure 3.9 – Potential efficiency limit of the sample 2757 considering perfect selective contacts and taking into account the lateral diffusion (black dots). Theoretical limit of a classical solar cell with a 0.78 eV band gap (black line)

is the previously calculated output voltage [17]. Classical conversion efficiency limit (black line), the potential conversion efficiency (black dots) and its linear fit (red line) are plotted in Fig. 3.9.

The theoretical efficiency limit (Schockley-Queisser) for a classical solar cells of 0.78 eV band gap grows from 24% to 36% at respectively 1 and full concentration. The potential conversion limit of our tested device is already higher than the SQ limit for a 0.78 eV band gap solar cell at 200 suns as the carrier temperature exceeds the room temperature. Therefore, it would reach 48% at 14000 suns still considering the absorbed carriers are fully collected and ESC are perfect.

This study shows the value of this novel optical investigation, which has the ability of evaluating electrical quantities contactless. The set-up is perfectly adapted to our needs as no effective ESC has been able to be implemented on our absorber yet. In that event, we are able to point out the great potential of the structure 2757 with a 50% achievable conversion efficiency at 14000 suns, deduced from local optical measurements.

As HCSC presents similarity with thermoelectric device (low electron-phonon interaction, high electron conductivity) we will now present how our device and optical method could be used in the field of thermoelectricity. It will also lead to a new

point of view on HCSC devices.

3.1.4 Thermoelectric effect in HCSC

In this section, photo-Seebeck coefficient will be calculated and defined from the determination of local temperature of emission and $\Delta\mu$.

Photo-Seebeck coefficient calculation

First, one has to use the reciprocal relations of Onsager taken from a fluid model [82]. The equation system defines the current and power particle fluxes. If one focus on the current flux, each particles current densities are given by:

$$\overrightarrow{J_Q^e} = - L_{qq}^e \overrightarrow{grad}(\eta^e) - L_{qs}^e \overrightarrow{grad}(T^e) \tag{3.10}$$

$$\overrightarrow{J_Q^h} = - L_{qq}^h \overrightarrow{grad}(\eta^h) - L_{qs}^h \overrightarrow{grad}(T^h) \tag{3.11}$$

$$\text{where : } L_{qq}^{e,h} = \frac{\sigma^{e,h}}{e^2} \tag{3.12}$$

$$L_{qs}^{e,h} = \frac{\alpha_H^{e,h}\sigma^{e,h}}{e} \tag{3.13}$$

$$\eta^e = \mu_0^e + k_b T^e \ln(\frac{n}{N_C}) - |e|V \tag{3.14}$$

$$\eta^h = \mu_0^h + k_b T^h \ln(\frac{p}{N_V}) + |e|V \tag{3.15}$$

where L_{qq} and L_{qs} are matrix parameters related to macroscopic material parameters: $\sigma^{e,h}$, $\alpha_H^{e,h}$, $\eta^{e,h}$, $\mu^{e,h}$, which are respectively the conductivity, the Seebeck coefficient, the electrochemical potential, and the chemical potential of electrons and holes. As the temperature measured is a temperature of the electron-hole pair T_{e-h}, one can consider $T_{e-h} = T^e = T^h$. Moreover, as the MQWs region is undoped and the optical excitation generates as much electrons as holes, both carriers diffusion have to be taken into account. Then, no external field is applied, therefore, after their diffusion, carriers will recombine among themselves, meaning $\overrightarrow{J_Q^e} + \overrightarrow{J_Q^h} = 0$. Thus, addition of Eq. (3.10) and Eq. (3.11) gives:

$$L_{qq}^e \overrightarrow{grad}(\eta^e) + L_{qq}^h \overrightarrow{grad}(\eta^h) + (L_{qs}^e + L_{qs}^h)\overrightarrow{grad}(T_{e-h}) = 0 \tag{3.16}$$

Let us remind:

$$\eta^e = E_{fn}$$
$$\eta^h = -E_{fp}$$
$$\Delta\mu = \eta^e + \eta^h$$

where E_{fn} and E_{fp} are the quasi-Fermi levels electrons and holes. As we measure their difference ($\Delta\mu$), one must write out an average matrix term $\bar{L}_{qq}$ and its matching term $\tilde{L}_{qq}$:

$$\bar{L}_{qq} = \frac{L^e_{qq} + L^h_{qq}}{2} \tag{3.17}$$
$$\tilde{L}_{qq} = \frac{L^e_{qq} - L^h_{qq}}{2} \tag{3.18}$$

so $\Delta\mu$ comes out in Eq. (3.16) such as:

$$\bar{L}_{qq}\overrightarrow{grad}(\Delta\mu) + (L^e_{qs} + L^h_{qs})\overrightarrow{grad}(T_{e-h}) + \tilde{L}_{qq}\left[\overrightarrow{grad}(\bar{\eta^e}) - \overrightarrow{grad}(\bar{\eta^h})\right] = 0 \tag{3.19}$$

If one details the right term $\left[\overrightarrow{grad}(\bar{\eta^e}) - \overrightarrow{grad}(\bar{\eta^h})\right]$ according to Eq. (3.14) and Eq. (3.15) knowing that there are no change of material composition along lateral direction $\overrightarrow{grad}(\mu_0^{e,h}) = 0$ and no electric field is $\pm qV = 0$, one gets:

$$\left[\overrightarrow{grad}(\bar{\eta^e}) - \overrightarrow{grad}(\bar{\eta^h})\right] = \overrightarrow{grad}\left[k_b T^e \ln\left(\frac{n}{N_C}\right)\right] - \overrightarrow{grad}\left[k_b T^h \left(\frac{p}{N_V}\right)\right] \tag{3.20}$$

As a reminder $T^e = T^h = T_{e-h}$ and $n \approx p$, thus the equation becomes:

$$\left[\overrightarrow{grad}(\bar{\eta^e}) - \overrightarrow{grad}(\bar{\eta^h})\right] = \overrightarrow{grad}\left[k_b T_{e-h} \ln\left(\frac{N_V}{N_C}\right)\right] \tag{3.21}$$

temperature becomes the only term, which depends on the direction.

Let the reader reminds that in a direct band gap semi-conductor $\frac{N_V}{N_C} = \frac{m_h}{m_\Gamma}$, where m_h is the effective hole mass and m_Γ is the electron mass in the center of the Brillouin zone (Γ), thus:

$$\left[\overrightarrow{grad}(\bar{\eta^e}) - \overrightarrow{grad}(\bar{\eta^h})\right] = \frac{3}{2}k_b \ln(\frac{m_h}{m_\Gamma})\overrightarrow{grad}(T_{e-h}) = C \times \overrightarrow{grad}(T_{e-h}) \tag{3.22}$$

Therefore, the equation Eq. (3.19) writes as:

$$-\frac{\overrightarrow{grad}(\Delta\mu)}{\overrightarrow{grad}(T_{e-h})} = \frac{L^e_{qs} + L^h_{qs} + \tilde{L}_{qq} \times C}{\bar{L}_{qq}} \tag{3.23}$$

At last, if one replaces $\bar{L}_{qq}$ and $\tilde{L}_{qq}$, which write as Eq. (3.17) and Eq. (3.18) by Eq. (3.12) and Eq. (3.13), in Eq. (3.23):

$$-\frac{\overrightarrow{grad}(\Delta\mu)}{\overrightarrow{grad}(T_{e-h})} = 2e\frac{\alpha_H^e\sigma^e + \alpha_H^h\sigma^h}{\sigma^e + \sigma^h} + \frac{\sigma^e - \sigma^h}{\sigma^e + \sigma^h} \times C \tag{3.24}$$

In the equation, one can recognize an intrinsic Seebeck coefficient α_H^i, which writes as:

$$\begin{aligned} \alpha_H^i =& \frac{\alpha_H^e\sigma^e + \alpha_H^h\sigma^h}{\sigma^e + \sigma^h} \\ \text{where}: \sigma^e =& -en\bar{\mu}^e \\ \sigma^h =& en\bar{\mu}^h \end{aligned} \tag{3.25}$$

Here, $\bar{\mu}^{e,h}$ are the electron and hole mobilities, therefore Eq. (3.23) becomes:

$$\begin{aligned} \alpha_H^i &= \bar{\alpha_H^i} - \frac{1}{2e}\frac{\overrightarrow{grad}(\Delta\mu)}{\overrightarrow{grad}(T_{e-h})} \\ \text{where}: \bar{\alpha}_H^i &= \frac{k_b}{e}\left[\frac{3}{4}\ln\left(\frac{m_\Gamma}{m_h}\right)\right] \end{aligned} \tag{3.26}$$

The equation shows the Seebeck coefficient depends on a left hand-side term $\bar{\alpha}_H^i$, which only depends on the material itself (effective) and a right hand-side one, which is dependent on thermodynamic quantities gradients ratio. This result is analogous to Cai and Mahan's calculations, which evidence that the Seebeck coefficient S experimentally measured (phenomenological one) is the sum of an effective Seebeck coefficient $\bar{S}$ (independent on the material doping) and the thermodynamic quantities gradients ratio in [83]. This calculation is valid for an homogeneous doped semiconductor and is written as:

$$\alpha = \bar{\alpha} - \frac{1}{e}\left(\frac{\partial\mu}{\partial T}\right)_n \text{where}: \bar{\alpha} = \frac{k_b}{e}\left(\frac{5}{2} + r - ln\frac{n}{N_c}\right) \tag{3.27}$$

here, only one carrier type is considered thus, the chemical potential is replaced in our formula by $\Delta\mu$ over two.

Photo-Seebeck coefficient description

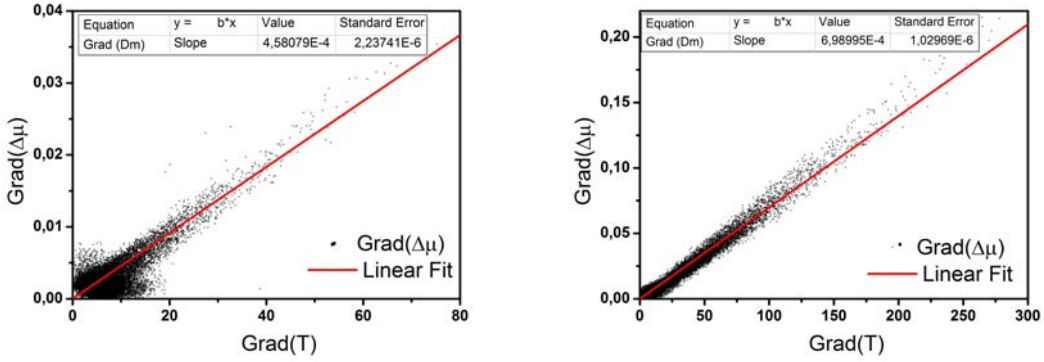
The Seebeck coefficient we probe depends on both temperature of emission and chemical potential of radiation consequently it will be defined as the photo-Seebeck

coefficient. It represents the entropy per electron-hole pair left per unit pair, or the average heat exchange per electron-hole pair divided by the temperature. It differs from the classical Seebeck coefficient, as the temperature considered here, is not the lattice one. However, in samples were the thermal conductivity is low, laser excitation could generates a lattice temperature gradient, and the measurement would be a classical Seebeck coeffient. The characterization is therefore transferable. Indeed, the classical Seebeck coefficient is normally measured by applying a lattice temperature gradient along a bulk material where the resulting electrical potential difference is probed. The main techniques are described in [84]. This review article insists on the measurement complexity, which induces strong Seebeck coefficient differences on a similar compound. The authors explained the requirements for a good Seebeck coefficient determination. In the measurement, four criteria are found to be essential: the temperature and voltage should be spatially synchronous, probes should be in very good thermal and electrical contact, acquisition of low voltage with minimal extra-contributions, at last the thermal gradient should be appropriate so $S_{ab}(T)$ linearity is ensured.
Thus, thanks to our optical determination method of the thermodynamic quantities, we propose an alternative measurement of Seebeck coefficient, which answer to the four requirements. The determination of temperature and voltage are simultaneous and spatially resolved, no contacts are used, the optical method does not interfere with the medium and the Seebeck coefficient can be thermally "resolved". To our knowledge, it is the first time a photo-Seebeck coefficient is measured, locally, contactless and parallel to MQWs plan.

Getting the photo-Seebeck coefficient

In order to extract the coefficient, the gradient of each thermodynamic quantity has been calculated according to Eq. (3.27) from Fig. 3.1e and Fig. 3.1c. Norm of $\Delta\mu$ gradient is plotted as a function of the norm of the emission temperature one in Fig. 3.10 for two different mean absorbed powers 7000 (b) and 22000 suns (a).

Each dot corresponds to a pixel of the maps. One can see the two diagrams are linear, which corresponds to our predictions in Eq. (3.27). Therefore, in order to get the phenomenological intrinsic photo-Seebeck coefficient, one has to calculate the effective Seebeck coefficient $\bar{\alpha}_H^i$. Considering the material is a bulk one, in the direction parallel to the MQWs, the electron and hole mass of the material can be calculated from the matlab code (ZincBlendeIIIV.m) of T. Mei [80]. One gets $m_\Gamma = 0.0510 m_0$ and $m_h = 0.5843 m_0$, therefore $\bar{\alpha} = -158\,\mu V/K$. Photo-Seebeck



(a) (b)

Figure 3.10 – Scatter diagram of the norm of $\Delta\mu$ gradient as a function of the norm of the temperature of emission measured for a mean power of 22000 suns (a) and for 7000 suns (b) on sample 2757, (black dots). A linear fit is also plotted (red line) with the intercept fixed at 0.

coefficients are -507 and -397 $\mu V/K$ for respectively 7000 and 22000 suns. Firstly, one can remark both coefficients are negative, indicating a dominant contribution of the electrons according to the intrinsic Seebeck coefficient definition Eq. (3.25).

Secondly, one can now focus on the absolute calculated values. The only article found on InGaAsP material is Zebarjadi *et al.* work [85]. They found a simulated Seebeck coefficient from Monte Carlo technique in InGaAsP (no information on doping level) increasing from 260 to 310 $\mu V/K$ as the thickness of the layer decreases from 2 μm to 100 nm (at 300K). However, they investigated it for carrier transport perpendicular to the layer. In our case, the carrier transport is parallel to the layer. Hence we should compare our data to the bulk value, keeping in mind that they calculated a Seebeck coefficient resulting from a lattice temperature gradient, whereas our arises from hot carriers. Let us remind the Seebeck coefficient is a measurement of an average heat exchange per carrier. The heat exchange is characterised for classical Seebeck coefficient by electron-phonon energy exchange i.e. entropy loss whereas for hot carriers, the entropy loss is reduced and electron-phonon interactions is limited. Therefore, the heat exchange results from the lateral carriers-carriers kinetic energy exchange. As the carrier-carrier interaction is much faster than the electron-phonon scattering, we expect a higher heat exchange rate and therefore a higher Seebeck coefficient section 1.2.2.

At last, as the Seebeck coefficient is known to change with the temperature range, thus we plotted the photo-Seebeck coefficient map as a function of the temperature of emission map at 22000 suns in Fig. 3.11. Such kind of instantaneous S(T) measurement was already performed in [86]. In order to facilitate the interpretation we

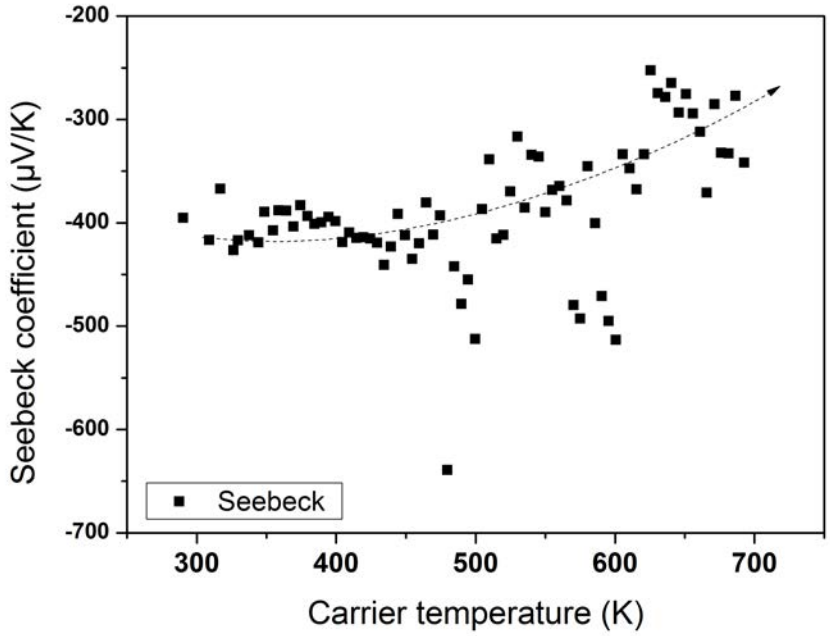


Figure 3.11 – Photo-Seebeck coefficient as a function of temperature of emission extracted from Eq. (3.27). Sample 2757, mean absorbed power of 22000 suns, $\lambda = 975\,nm$.

reduced the noise by making a moving average of the local photo-Seebeck coefficient on a range of 10 K.

One can see, the photo-Seebeck coefficient is constant at -400 $\mu V/K$ from 300 to 450 K. Then, its value increases to -300 $\mu V/K$ as the temperature increases to 670 K. Low temperature photo-Seebeck coefficients are more accurate than low ones as $\Delta\mu$ gradient is stronger in this temperature range. Such a variation has been observed on different materials in the same temperature range (Si-n, InAs-n) in [87, 88]. Further studies on well known thermoelectric material where the literature is wider will be performed soon in our lab.

In this section, we have developed a new way of probing photo-Seebeck coefficient. This measurement was applied on hot carrier population but could be extended to classical thermal gradient. Indeed, PL spectrum changes with the lattice temperature (absorption threshold and black body) and could be measured will applying a thermal gradient. The optical method would measure an intrinsic local material constant without being affected by electrical probes. Here, we measured a photo-Seebeck coefficient between -507 and -397 $\mu V/K$ depending on the carrier density and the measurement could be temperature resolved. Values are quite high as most of Seebeck coefficients ranges between -1000 and 1000 $\mu V/K$.

3.2 Optical evidence of HCSC regime by averaged measurements

In the previous section, it was shown that the hot carrier absorber (MQWs) is no longer the limiting parameter in the HCSC making. Indeed, the output voltage in the ideal case qV_{ESC} could be calculated from $\Delta\mu$ probed in the MQWs. In this section, we will see that we are actually able to measure qV thanks to the access at higher absorbed powers, with the confocal set-up calibrated by HI one. Using the combination of the two set-ups, we will benefit from their own advantages. Thus, firstly, we will focus on the determination of average temperatures of emission. Secondly, the averaged $\Delta\mu$ will be extracted. At last, we will demonstrates that the device work as a HCSC.

3.2.1 Probing emission and lattice temperature by confocal set-up

This subsection presents the simultaneous measurement of lattice temperature and temperature of emission by the confocal set-up. This is an important challenge for the hot carrier community. Indeed, we previously considered the lattice temperature was not changing as there were no spectral displacement of the PL signal but no effective measurement was done at room temperature.

Carriers in barrier are thermalised

We showed it was possible to get hot temperatures of emission in the MQWs by confocal measurement in section 2.2.3. Nevertheless, in that section the values were not commented, as the aim was to calibrate the intensity flux in confocal mode. Carriers in the QWs can reach 1170 K (black squares, Fig. 3.12). These temperatures of emission are very high considering the experimental conditions and the literature (see previous section). But the mean absorbed powers are much higher than the local one in the previous section. Indeed, in the previous section, temperatures reached 670 K at 14000 suns (local absorbed power), whereas here it reaches 400 K at the same power. It shows the interest of the thermalisation rate, which allows to compare the samples, as it takes into account the absorbed powers.

We have seen in the previous chapter through Fig. 2.5 that the spectral range used to extract these data covers PL emission arising from MQWs (Eg=0.78 eV) but also the barriers (Eg=1.05 eV). Therefore, we focus now on the carrier temperature

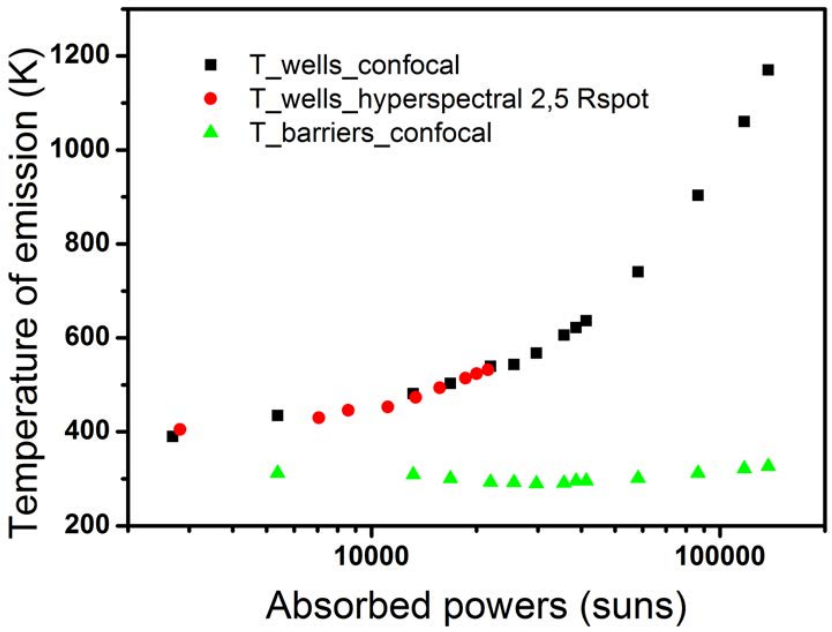


Figure 3.12 – Emission temperature of the MQWs probed by confocal (black squares), by HI (red dots) and emission temperature of the MQWs barrier probed by confocal (green triangles) for different mean absorbed powers on the sample 2757 under laser excitation at 975 nm

in the barrier energy range. The Fig. 3.12 represents the different temperatures of emission of the QWs (black squares) and the barrier (green triangles) measured by confocal and HI (red dots) at different mean absorbed powers. One can see that the temperature of emission of the barriers is close to room temperature. It fluctuates from 300 to 315 K showing that the barrier temperature is in fact much lower than the MQWs one, staying at room temperature.

The barrier acts as a bulk material with a very high thermalisation rate. It means that the temperature of emission in the barrier is in fact the lattice one. The interest of this measurement is high.
First, it enables to know simultaneously the lattice temperature and the temperature of emission of the MQWs. The lattice is definitely cold compared to the emission temperature of the MQWs, which confirms our observation that A(E) is not spectrally shifting. Nonetheless, thanks to this measurement we can probe it without knowing the Varshni's parameters of the MQWs. Our measurements were made possible thanks to the absorbance study in the section 2.4.4.
To continue, both regions (barriers and MQWs) present a distinct temperature. One can deduce that carriers in the barrier and MQWs are not in equilibrium with each

other.

We have shown in this subsection it was possible to determine the temperature of the lattice (thanks to the barrier temperature of emission) and temperature of emission of the MQWs simultaneously. Furthermore, the barriers and MQWs are thermodynamically isolated, which means that the semi-selective contacts can be a first simple solution before the ESC are developed. To finish, the collection area determination will give the possibility to convert the relative averaged $\Delta\mu$ to an absolute one in confocal mode, see section 2.2.3. Thus, $\Delta\mu$, the third thermodynamic quantity will be calculated in the next subsection.

3.2.2 Probing average of $\Delta\mu$ by confocal set-up

It has been seen that the temperature of emission measured by confocal is a spatial average and does not require absolute measurements of the PL spectra. However, $\Delta\mu$ determination, which is linked to the PL spectra intensity, requires absolute measurements. We have described in section 2.2.3 a method to get averaged thermodynamic quantities from HI that we have already used to get the temperature of emission. In this section, we will first extract absolute averaged $\Delta\mu$. Then, we will show that device 2757 works as a hot carrier solar cell.

Getting absolute $\Delta\mu$ in confocal mode

Thanks to the confocal calibration method that we developed in section 2.2.3, we can get the recalibrated $\Delta\mu^{abs}_{conf}$ (black squares) in Fig. 3.13. In order to have a better point of view of the spatial integration area effect on the average $\Delta\mu$, we have added the data from HI (green dotted lines) where the legend indicates the radius of the integration area, in illumination spot radius units. Firstly, one can see that $\Delta\mu^{abs}_{conf}$ ranges between average $\Delta\mu$ of $2R_{spot}$ and $3R_{spot}$. Let us remind the radius of confocal collection area was estimated at 2.5 times the illumination spot one ($2.5R_{spot}$), which is in agreement with the results displayed. Secondly, the average $\Delta\mu$ where the radius worth $1R_spot$ would give an homogeneous-like illumination value, as work a standard solar cell. To that end, the value we get in confocal are slightly underestimated. However, they could be easily translated, as the difference between the HI data at $2.5R_{spot}$ and $1R_{spot}$ is constant (around 30 meV) over the absorbed powers.

Thirdly, we can observe that all $\Delta\mu$ are reaching a maximum value for different radius of integration. As the illumination is not homogeneous with the radius, the local absorbed power at the center is much higher. The saturation is reached at lower

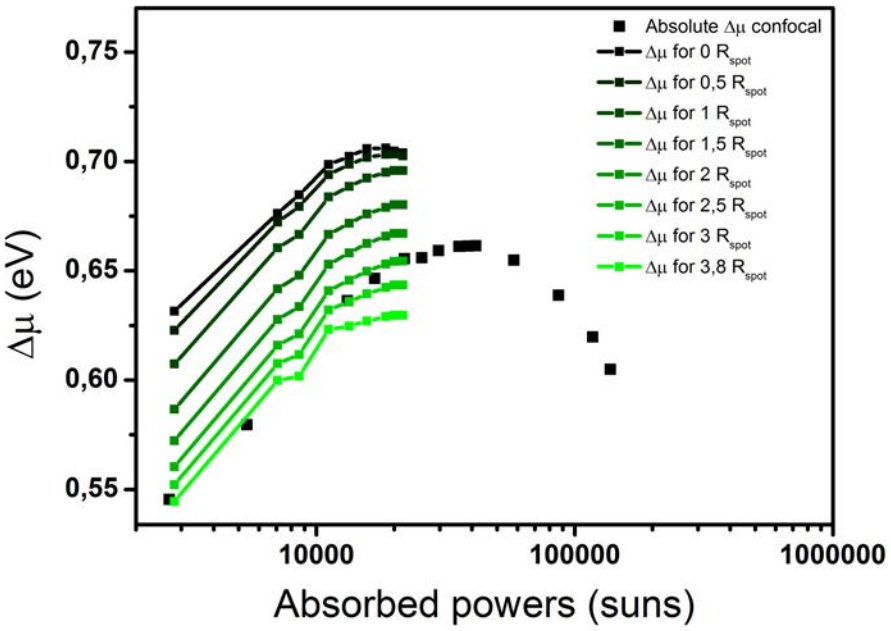


Figure 3.13 – $\Delta\mu$ obtain by HI set-up for different spatial integration (green dotted lines) and the recalibrated confocal measurement (black square). Remark that for each absorbed power, one HI data acquisition was made. Then, the data were integrated spatially. Legend indicates the radius of integration area, in units of illumination radius, which grows from 0 to 3.8 R_spot (black to green)

absorbed powers as we reduce the spatial integration area. Different phenomena could explained this fact:

- Auger/Impact ionization
- Lattice temperature
- Carrier extraction
- Lateral diffusion

The lateral diffusion will not be talked about since it was already discussed in section 3.1.1 and section 3.1.4.

Auger/ Impact Ionization Auger and Impact ionization effects are two processes, which brings into play three carriers, accordingly their effect should be proportional to P_{abs}^3. As $\Delta\mu$ increases with the logarithm of the power in standard conditions, the sudden decrease of $\Delta\mu$ observed in Fig. 3.13 could be attributed to the Auger effect. Indeed Auger effect would decrease $\Delta\mu$ as the power increases contrary to impact ionization. Thus Auger effect should be taken into account. However, these structures are particularly well suited for this study, as radiative recombination is dominant over the Auger effect, even at high injection regime according to [72]. Thus, we can safely suppose Auger recombination is not at stake here.

Lattice temperature The lattice temperature can increase with the incident power if the material thermal conductivity is too low. However, the peak of PL spectra maximum does not change and the lattice temperature measured from the barrier temperature of emission is only 15K above room temperature. Considering a linear impact of lattice temperature on $\Delta\mu$ degradation, $\Delta\mu$ would only decrease by 1%.

Carrier extraction The temperature of emission in the well increases with the absorbed power. Consequently, some hot carriers should escape from the wells to the barrier as the absorbed power increase if these carriers follows the condition $\Delta\mu_{well} > \Delta\mu_{barrier}$. Therefore, $\Delta\mu$ could saturate with the absorbed power. We can quantify the ratio of photo-carrier recombination in the well (η_w^p) or in the barrier (η_b^p) over the total amount of photo-carrier by integrating the PL intensity such as:

$$\eta_w^p = \frac{\int_0^{E_b} I_{PL}\, dE}{\int_0^{\infty} I_{PL}\, dE} \tag{3.28}$$

$$\eta_b^p = \frac{\int_{E_b}^{\infty} I_{PL}\, dE}{\int_0^{\infty} I_{PL}\, dE} \tag{3.29}$$

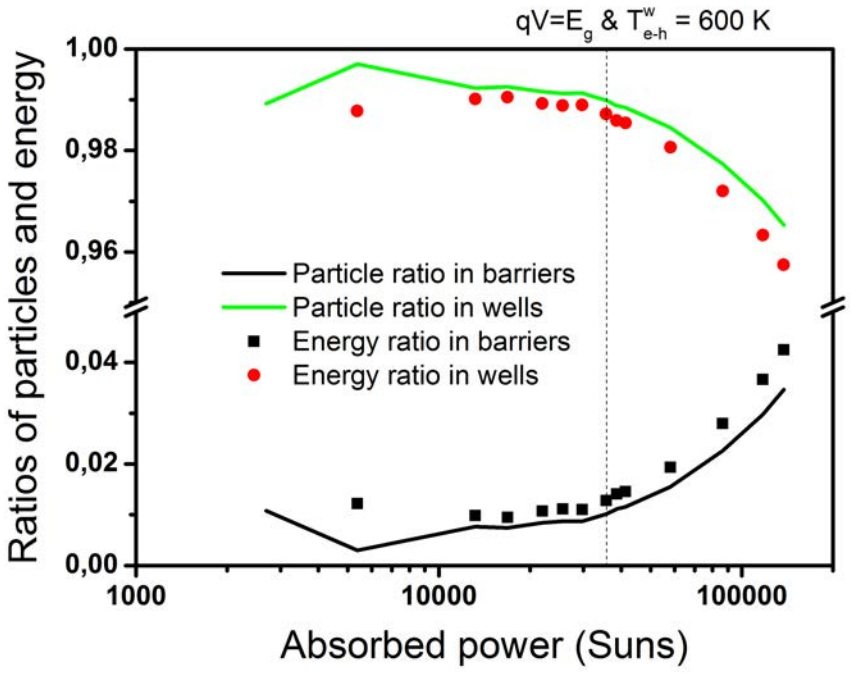


Figure 3.14 – Intensity of PL of QWs and barriers peak normalized by their maximum as function of absorbed power (a). Ratio of MQWs over barrier PL intensity peak (b)

with E_b the band gap of the barrier. The balance can also be done on photo-carriers energy by integrating the product of PL intensity and its energy:

$$\eta_w^e = \frac{\int_0^{E_b} I_{PL} E \, dE}{\int_0^{\infty} I_{PL} E \, dE} \tag{3.30}$$

$$\eta_b^e = \frac{\int_{E_b}^{\infty} I_{PL} E \, dE}{\int_0^{\infty} I_{PL} E \, dE} \tag{3.31}$$

with η_w^e and η_b^e respectively the ratio of energy in the well and in the barrier over the total emitted energy.

This can be done in confocal mode since the barrier and MQWs can be distinguished. One can see in Fig. 3.14 that the ratios of energy and particles radiative recombination are constant from 2000 to 30000 suns. Then, there is an energy and particle transfer from wells to barrier, which increases by 4 points. This transfer is important and could explain $\Delta\mu$ decrease observed in Fig. 3.13 at similar powers. This phenomenon appears to be non negligible.

Hot carrier solar cell regime by optical probing

It was seen in the previous section, we were able to recalibrate confocal data with HI ones. It led to the determination of an absolute averaged $\Delta\mu$ in confocal at higher powers than in HI mode.
The resulting average $\Delta\mu$ are plotted in Fig. 3.15 as a function of the absorbed powers. The triangles represent the HI data, whereas the squares are confocal one. The blue squares represent data calculated for an average $\Delta\mu$ made on the confocal collection area of $2.5R_{spot}$. $\Delta\mu$ in MQWs were already discussed in the previous section. As the intensity coefficient, which links the HI to the confocal set-up was determined, it can also be used to get $\Delta\mu$ of the barrier according to Eq. (2.11). On the same chart, the averaged $\Delta\mu$ of the barrier (green squares) was added. One can see that $\Delta\mu$ in the barrier is much higher than the one in the QWs. It increases with the absorbed powers from 0.65 eV to 0.82 eV and the saturation in the case of QWs $\Delta\mu$ is no longer observable. The $\Delta\mu$ values become even higher than the e1-lh1 transitions (dashed line) at around 40000 suns. Then, one can see the difference between $\Delta\mu$ of the barrier and the QWs increases with the absorbed powers; at low absorbed powers the carriers are cold and $\Delta\mu$ in barrier and QWs are equals. The difference increase originates from the temperature elevation. This result is fundamental because it shows an effective transfer of hot carriers from the QWs to barriers, which plays the role of "cold" electrodes in the hot carrier solar cell definition. This allows the device to get an electrical potential qV, which goes beyond the transition energy. At full concentration i.e. 46000 suns, the maximum $\Delta\mu$ would be slightly beyond the radiative open circuit voltage. This is the first time that such an evidence of hot carrier energy transfer is made. The next question we would like to answer is what we could expect from a theoretical point of view. Does $\Delta\mu$ of barrier really represent the maximum open circuit voltage?

3.3 Simulation of thermodynamic quantities in device 2757

The code developed by A. Le Bris has been introduced in section 2.5.1 through its general principle and architecture. The aim of this section is to get a better understanding of the experimental results thanks to simulation. The choices we made to define our sample 2757 in agreement with the code capabilities will be firstly explained. The simulated thermodynamic quantities as a function of the absorbed powers will be presented and the parameters of influence will be discussed.

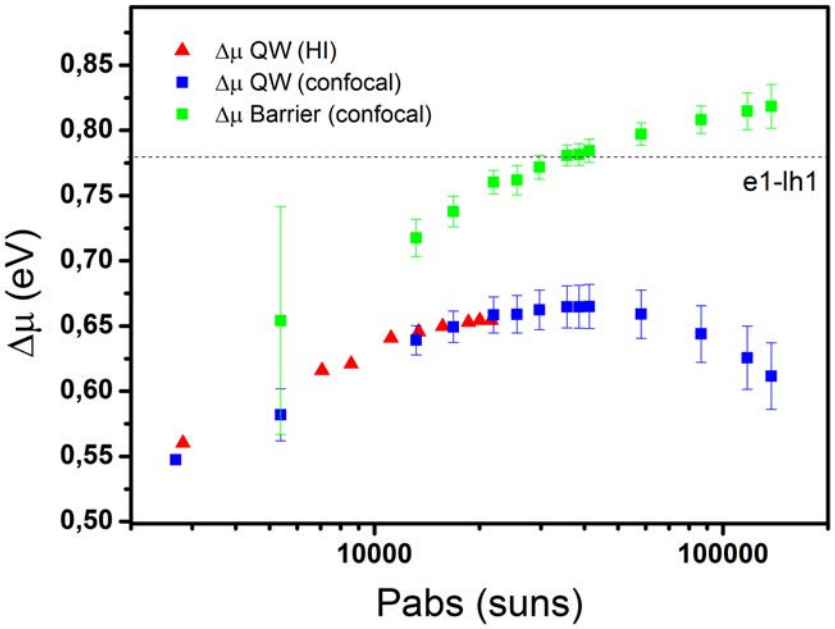


Figure 3.15 – $\Delta\mu$ as a function of the absorbed powers in the barriers (squares black and blue, up) and the wells (squares black and blue, bottom) averaged on different collection area by confocal. The collection area is either the confocal one of a radius equal to 2.5 times the illumination radius ($R = 2.5R_{spot}$, black) or equal to the illumination area ($R = R_{spot}$, blue). $\Delta\mu$ measured by HI are also plotted for the two different collection radius (triangles). Sample 2757, $\lambda = 975nm$.

At last, the simulations will be compared with the experiment.

3.3.1 Input parameters

As it was seen in section 2.5.1 the software initialisation parameters can be separated in three blocks: external, absorber and device parameters. The influence of specific parameters will be studied in the next subsection keeping the general parameters defined as follows.

- External parameters: Experiments were done at ambient temperature (300K) with an incident laser at 975 nm (1.27 eV). However, we have seen the carriers in the barrier were fully thermalised consequently the photo-carriers will be considered to be injected in the well, directly from the barrier energy band gap. Consequently, the absorbed photo-carriers energy will be fixed at 1.05 eV.

- Material parameters: The absorber is defined with a 0.78 eV energy band gap with a heavy-side absorbance where all the incident photons are absorbed. The relaxation of the photo-carriers will only result from electron-LO phonon interaction, with a LO phonon energy at about 350 cm^{-1}, which corresponds to the lowest LO phonon energy of each binaries compounds composing InGaAsP. The thermalisation rate was found to vary between at $4 - 8W/K/cm^2$ therefore we will round it up at 10 $W/K/cm^2$.

- Device parameters: As previous experimental studies are done at open circuit voltage, no carriers are extracted, therefore there should not be any influence of the device parameters (except the extraction energy, this was checked and validated by simulation). Still, as the next study in section 4.2 will be done at different applied bias, we will define the device parameters right here. The extraction energy was set at 1.05 eV, i.e. energy band gap of the barriers. As the software requires the definition of contacts selectivity and the barriers are only a high energy pass filter energy, we set the contacts selectivity at 3 eV, so it has no influence on the results. Indeed, above 1 eV, (see section 1.2.3) the selectivity has no more effect on the performances. We set it at 3 eV as a precaution. Note that A. Le Bris performed a study on selectivity impact and it showed selectivity was not crucial for hot carrier solar cells: semi-selective contacts already improves classical photovoltaic solar cells if the thermalisation factor is low enough [8]. The Fig. 3.16 gathers the main parameters of influence we have set. It represents the band energy diagram the software will simulate.

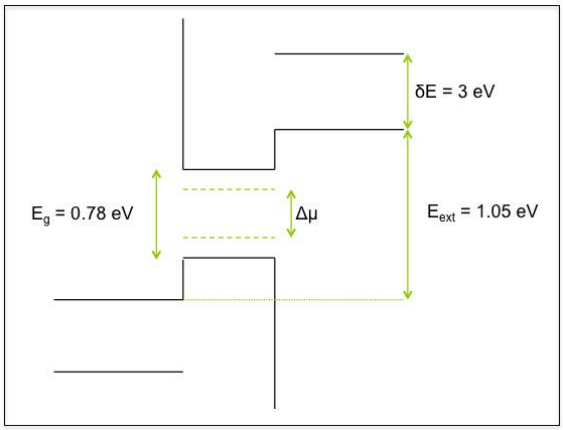


Figure 3.16 – Energy diagram of the simulated device 2757

3.3.2 Results of PL under different absorbed powers

The goal of simulation is to understand the influence of the main parameters of the device definition through the calculation of thermodynamic quantities. Accordingly, we studied two main parameters, which are the thermalisation rate and the extraction energy as a function of the absorbed powers.

Thermalisation rate The thermalisation rate was varied from 1, 10 and 100 $W/K/cm^2$. Its influence on the temperature of emission is obvious as we set it according to Eq. (1.3) in the software. Fig. 3.17a presents the temperature of emission as a function of the absorbed powers at three different thermalisation rates. It corresponds, from green to black, to the decrease of the thermalisation rate. All the curves start from room temperature and reach at full concentration 700, 1200 and 1900 K as thermalisation rate decreases.

We now look at the influence of the thermalisation rate on $\Delta\mu$. Fig. 3.17b exhibits $\Delta\mu$ as a function of the absorbed powers at different thermalisation rates. One can obviously see that as the thermalisation rate is high (100 $W/K/cm^2$), the $\Delta\mu$ curve follows the standard behaviour of the radiative open circuit voltage in a classical photovoltaic solar cell already discussed in section 3.1.3 (logarithm dependence on absorbed power). This result is important as the simulation validates our expectation when the thermalisation is fast. As the thermalisation rate decreases, one can see the beginning of the derivative change (beginning of curves sub-logarithm behaviour) is reached at lower absorbed powers, respectively 2000, 200 and 20 suns. If one observes once again the 3.17a, which plots the temperature of emission, we can correlate the change of derivative we observed to the strong increase of the temperature, which can be seen at 2000, 200 and 20 suns. It points out the ther-

malisation rate has not only an effect on the temperature but also on the "hot" $\Delta\mu$, which changes shape and decreases. Indeed, whatever the thermalisation rate, $\Delta\mu$ does not exceed the band gap of 0.78 eV and as the thermalisation rate becomes lower (1 $W/K/cm^2$) $\Delta\mu$ even decreases to 0.75 eV at full concentration.

The impact of thermalisation rate on the open circuit voltage is plotted in Fig. 3.17c. Remind that contrary to "classical solar cells", the open circuit voltage do not follow $\Delta\mu$ in hot carrier solar cell. The output voltage is a function of temperature of emission, extraction energy and $\Delta\mu$. It writes as Eq. (3.8) in isentropic ESC. Similarly to the previous results, one can observe the open circuit voltage as a function of the absorbed powers for three different thermalisation rate. The color palette is analogous. All the curves starts from 0.58 V at 1 sun. Then open circuit voltage increases linearly with a stronger slope as the thermalisation rate decreases. A change of slope appears at the same absorbed power than $\Delta\mu$ one at 20, 200 and 2000 suns, which corresponds to the strong temperature increase. The curves reaches at full concentration 0.95, 1.02 and 1.03 eV as the thermalisation rate decreases. For the lowest thermalisation rate, one can even see a plateau. This plateau is due to the extraction energy, which is fixed at 1.05 eV. As a consequence, even if the mean hot carrier energy is higher than the extraction energy, the output potential will not change as the carriers will be fully thermalised in the contacts.

Extraction energy We studied the influence of the extraction energy on the thermodynamic quantities by changing it at 0.78, 1.05 and 1.35 eV. It respectively corresponds to the band gap energies of the absorber, the barriers of the MQWs and the claddings (InP) of the sample 2757. The other parameters were fixed following the hypothesis in previous section, as a reminder : Q=$10W/K/cm^2$, δE=3 eV, E_g=0.78 eV. We found the extraction energy has no impact on the temperature of emission and on $\Delta\mu$ in the absorber in open circuit regime as no carriers are extracted. However, it has a strong impact on the open circuit voltage. Thus, we plotted the open circuit voltage as a function of absorbed powers for the different extraction energy in 3.17d. The curves at extraction energies of 0.78 (black), 1.05 (dark green) and 1.35 eV (light green) start from 0.58 V, which is the radiative open circuit voltage at 1 sun and grow linearly until 200 suns, then the hot carrier effect impacts the open circuit slope. All the curves approach their respective extraction energies.

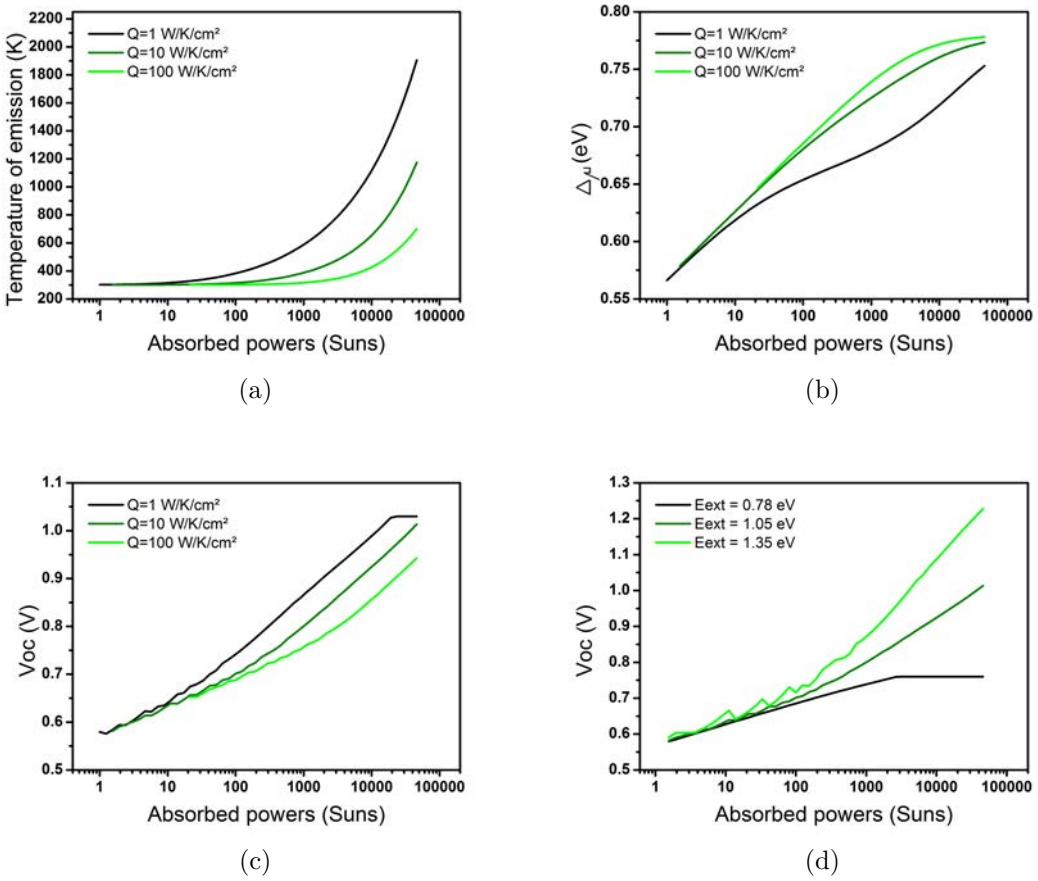


Figure 3.17 – Simulation of temperature of emission (a), $\Delta\mu$ (b), V_{oc} (c) as a function of the absorbed power for various thermalisation rate Q=1 (black), 10 (dark green), 100 $W/K/cm^2$ (light green). Open circuit voltage is also plotted as a function of the absorbed power for different extraction energy (d) $E_{ext} = 0.78$ (black), $E_{ext} = 1.05$ (dark green), $E_{ext} = 1.35eV$ (light green).

Short summary - In order to understand the impact of the light concentration on the samples thermodynamic quantities, we have simulated its performances according to a detailed model based on balance equations. Furthermore, we simulated predicted PL spectrum in order to understand the impact of the thermodynamic quantities on the spectrum. This simulation fixes ideas on the crucial parameters that will be measured in a global point of view and in a local one considering spatial dimensions. Two techniques are interesting because one provides an integrated quantities point of view close to a solar cell regime, whereas the other details spatial inhomogeneities. We have shown the barriers of the MQWs are fully thermalised and at room temperature whatever the absorbed power, which is an important result. Then, thermodynamic quantities in the barriers and the MQWs are separated showing independent reservoirs. Thanks to a local measurement, we could link optical $\Delta\mu$ to the electrical open circuit voltage. At last, local measurements indicated an underestimation of the thermodynamic quantities induced by photo-carriers diffusion. As the carrier diffuses laterally, the gradient of thermodynamic quantities highlights the first photo-Seebeck measurement. In this part, power have been studied, however, as the device present very good performances, we focused our interest on hot carrier distribution evolution according to light-bias solicitations.

CHAPTER 4

Optoelectronic characterisations

The device 2757 presented in section 2.3.4 has shown excellent properties in the previous chapter indicating a great potential to be used as a HCSC absorber. As the device is bipolar (pin diode) a study on electrical performances will be performed. In the first section, it will be shown that one can observe the exchange of hot carriers to a cold reservoir by applying an electrical bias. Then a simulation will be made in order to better interpret the experimental results in section 4.2.

4.1 Controlling thermodynamic quantities through PL under bias

It was seen that one could get thermodynamic quantities thanks to PL spectra measurement in the previous chapter. Acquiring PL spectra and applying a bias simultaneously will allow us to analyse thermodynamic quantities variations under bias: T(V), $\Delta\mu$(V).
The experiments of luminescence under electrical bias were done on confocal set-up in the same conditions than previous experiments: laser, collection area, spot size, partial calibration described in section 2.2.2 and in section 2.2.1. Current and PL spectra were extracted at each bias as explained in the section 2.3.4.

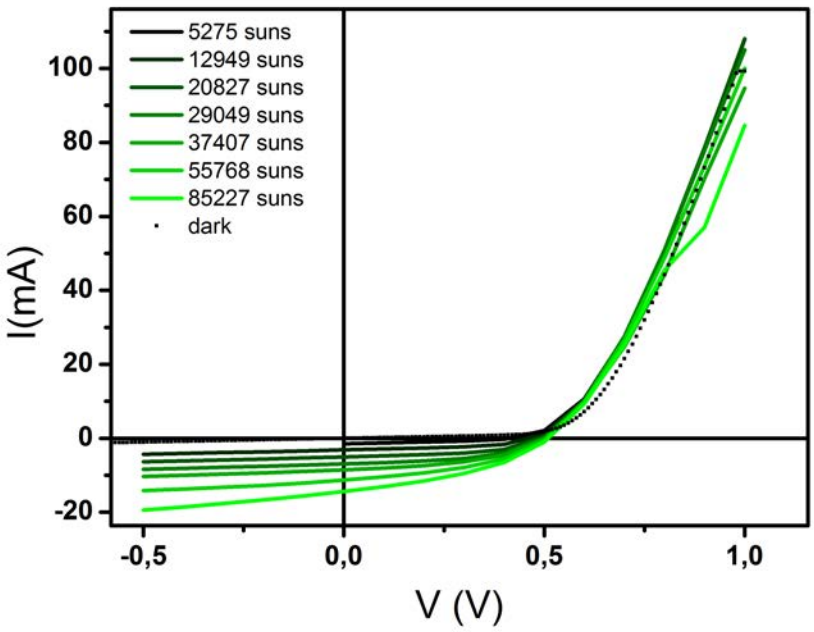


Figure 4.1 – IV characteristics for different absorbed powers. $\lambda = 975nm$, sample 2757

4.1.1 Current-Voltage (IV) curves

The IV characteristics are presented in Fig. 4.1 for different absorbed powers from 5000 to 85000 suns (from black to green lines) and in the dark (black squares). All the curves present a classical diode behaviour under illumination. Here, the analysis of the IV curves will be split, first in the case of negative current, then in the case of positive ones.

Firstly, at negative current, one can see that the slope increases with the absorbed powers. A high slope usually comes from either shunt resistance or degradation of the collection factor. As the dark diode presents a weak shunt resistance, the slope increase with the absorbed powers is attributed to the degradation of the collection factor [89, 90]. This phenomenon can be observed if one plots the short circuit current (V=0) as a function of the absorbed power (Fig. 4.2, top, black squares).

Indeed, a linear curve is expected if there is no degradation of collection. One can see this is no longer true, for last two powers (black squares), which correspond to 55000 and 85000 suns equivalent. This degradation is induced by three different phenomenon: bias dependent collection factor (also called bias dependent resistances) [91], screening of the internal electric field by high injection regime [92, 93], or inhomogeneous illumination [94].

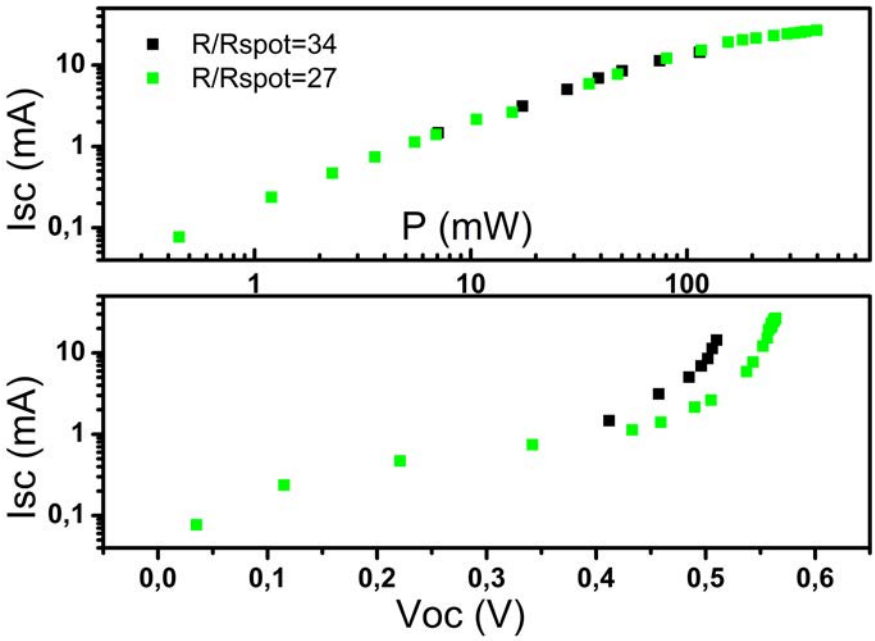


Figure 4.2 – Short circuit current as a function of the total absorbed powers (top) for different ratio of R_d/R_{spot} (R_d/R_{spot} = 27 green,R_d/R_{spot} = 34 black). Open circuit voltage as a function of the corresponding short circuit current (Bottom). Sample 2757, $\lambda = 975nm$.

- Bias dependent collection factor might occur in this device, as the band diagram presents barriers of potential (at well/barrier and barrier/InP interfaces), which could increases with the bias.
- Screening of the internal electric field is caused by strong $\Delta\mu$ resulting from the high injection regime. This phenomenon is even more pronounced, as the diode is dominated by the drift component of $\Delta\mu$, such as in pin diodes, where the space charge region is wide and the role of electrical field is essential. As this device is a pin diode, therefore it also might occur.
- Inhomogeneous illumination can degrade the collection factor through lattice temperature gradient or lateral $\Delta\mu$ gradient. Once again, this situation is encountered. Indeed, high carrier concentration is a requirement to generate hot carriers. Therefore, focusing the light on small areas is needed to reach these concentration levels. However, our bipolar device diameter is very large compared to the illumination spot one (diameters respectively 1200 μm and 35 μm).

Therefore, supplementary studies are required in order to distinguish the phenomena influencing the IV curves. For instance, a study in homogeneous illumination regime for different diode diameters, or for different band gap offsets at the previously mentioned interfaces, could be performed. Meanwhile, a study at open circuit voltage will be done in the next paragraph where there are neither series resistance nor carrier collection. In this case, the contribution of inhomogeneous illumination can be treated independently.
Secondly, at positive current, in the ideal case, the shifting approximation (or superposition principle) says the photo-current is constant and equal to the difference between the dark diode and illuminated diode [95]:

$$I_{tot} = I_d - I_{sc} \tag{4.1}$$

$$\text{where} : I_d = I_0 \left(\exp(qV/nk_bT) - 1\right) \tag{4.2}$$

where I, I_d, I_{sc}, I_0, n are respectively the total current, the dark diode current, the dark current (also called saturation current) and the ideality factor, the latter will be set as $n = 1$ in order to simplify the rest of the discussion. One can see in the figure that the dark diode superimposes with the illuminated curves in Fig. 4.1, meaning the shifting approximation does not hold. It can be shown that it may result from the inhomogeneous illumination regime by studying the open circuit

voltage evolution. If $I_{tot} = 0$, open circuit voltage is written as:

$$V_{oc} = k_B T_l \ln(I_{sc}/I_0 + 1) \tag{4.3}$$

However, under high illumination regime, I_{sc} becomes dominant, thus the equation simplifies as:

$$V_{oc} \approx k_B T_l \ln(I_{sc}/I_0) \tag{4.4}$$

Then, if we take into account the areas of illuminated diode S_{spot} and dark diode S_d, we can write the open circuit voltage resulting from inhomogeneous illumination V_{oc}^{inhom} as:

$$\begin{aligned} V_{oc}^{inhom} &\approx k_B T_l \ln(J_{sc}/J_0) - 2k_B T_l ln(R_d/R_{spot}) \\ \text{where : } I_{sc} &= J_{sc} \times \pi R_{spot}^2 \\ I_d &= J_d \times \pi R_d^2 \end{aligned} \tag{4.5}$$

Consequently, the electrical measurement of the open circuit voltage V_{oc}^{inhom} will be lowered as the radii ratio in dark and under illumination R_d/R_{spot} increases. To confirm that, an experiment of changing the fraction of illuminated diode area over the dark diode area was made. One can see (Fig. 4.2, bottom) the open circuit voltage decreases as R_d/R_{spot} increases from 27 (green dots) to 34 (black dots). Therefore, on the one hand, the influence of the inhomogeneous illumination on the open circuit voltage will be studied in the next subsection. On the other hand the link between the electrical measurement the V_{oc}^{inhom} to the optical $\Delta\mu$ will be established.

4.1.2 Comparison between electrical open circuit and optical $\Delta\mu$

It was seen a spatial average $\Delta\mu$ in the QWs could be extracted thanks to HI set-up in section 2.2.3. Therefore, one can plot it as a function of the radii ratio R_d/R_{spot} for different absorbed powers (from green to black) in Fig. 4.3. For all different powers, $\Delta\mu$ is nearly constant under $R_d/R_{spot} = 1$, then it decreases logarithmically as the ratio increases. Therefore, one can use Eq. (4.5) in order to fit $\Delta\mu$ of the wells as a function of the radii ratio, as, far from the illumination center, the temperature of emission in well is equal to the lattice temperature. Therefore, the right hand side term of the equation is constant, and the left hand side one is fitted (red lines). The fit is extended to the ratio $R_d/R_{spot} = R_{diode}/R_{spot} = 34$

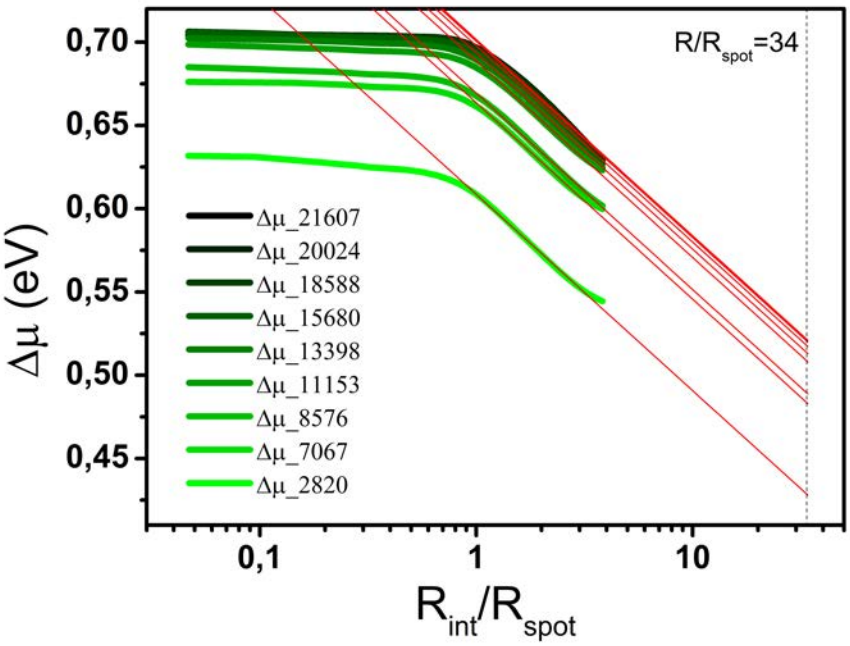


Figure 4.3 – Open circuit voltage probed from average $\Delta\mu$ (green) for different absorbed powers. A linear fit of the average $\Delta\mu$ with the logarithm of the radius is made to get the open circuit voltage

(vertical dashed line). The intersection between the fits and the vertical dash line corresponds to the maximum V_{oc}^{inhom} for different absorbed powers.

The values were plotted as a function of the absorbed powers in Fig. 4.4 (black squares). Open circuit voltages measured electrically were added (red dots). There is an important difference between the two, therefore the electrical open circuit voltage was also measured close to the electrical contact (blue star). The value becomes much closer to the average $\Delta\mu$. It means the open circuit voltage measured at the center is lowered by the sheet resistance. Such a phenomenon is not supposed to appear in open circuit voltage, as the current should not flow in the device and consequently no sheet resistance should be observed. However, in the case of an inhomogeneous illumination, there is a lateral current flowing, meaning the sheet resistance impacts the measurement. In the case of $\Delta\mu$ value, where the device is also illuminated at the center, remind that $\Delta\mu$ is not affected by resistances thus it reaches approximatively the same value than the one, close to the contact.

As a conclusion, the electrical device performances are strongly affected by the dark current and the sheet resistance. Therefore, an electrical study has to be performed on both smaller device and in homogeneous illumination regime to overcome these device limitations.

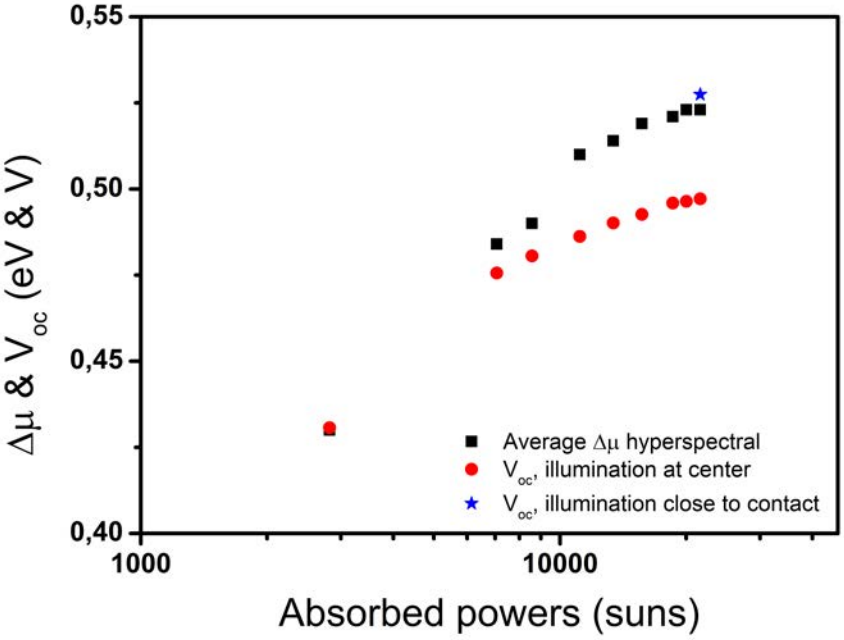


Figure 4.4 – Open circuit voltage measured optically and electrically. Optical open circuit voltage is extracted from from averaged $\Delta\mu$ over an effective radius see Fig. 4.3, (black square). Electrically probed open circuit voltage are measured with a centred illumination (red dots) and with an illumination close to the contact (blue star). $\lambda = 975nm$, $P_{abs} = 22000suns$, sample 2757.

4.1.3 Temperature of emission under electrical bias

As PL spectra were acquired at each bias, one can plot the temperature of emission of the QWs as a function of the bias in Fig. 4.5a. It was done for different absorbed powers from 5000 to 85000 suns (respectively from black to green). All the curves increase before reaching a plateau. Moreover, one can see at negative bias the slopes increase as the absorbed power increases. To better interpret the data, temperature as a function of the current was plotted in Fig. 4.5b. Indeed, current should be representative of the temperature evolution, as it is linked to the carrier extraction.
At positive current, carriers are electrically injected. However, carriers will be spread on all the diode area contrary to the photo-carriers, which result from an inhomogeneous illumination. If the maximum electrical power flux flowing in the diode is calculated from the IV product over the diode area, at 1V the electrical power will only correspond to 100 suns. This is much less than the optical power therefore the impact on PL spectra will be definitely negligible. All these observations can be seen in Fig. 4.5b for current satisfying the condition I(V>0.5V), the temperature stays constant. At last, the temperature of the barriers were also extracted for different bias however it did not show any variation, staying around 300K.
At negative current, first the temperature slope increases as the absorbed power increases, meaning that current extraction is "easier" as the temperature of emission increases. Then, the slope equals zero at lower currents as the absorbed power increase. The slope dT/dI is in fact proportional to the electrical energy extraction per carrier as, the kinetic energy is proportional to the temperature ($\propto nk_bT$) and the current to the carrier number. The result is plotted in Fig. 4.5c as a function of the bias.

One can see all the curves at different powers show a similar behaviour. Electrical extraction energy increases, then reaches a maximum, and at last the approaches zero. The only differences come from the increase of the maximum extraction energy, which shifts to lower bias, as the absorbed power increases. If one only looks at the maxima as the absorbed power increase, it seems the maximum saturates. These observations will be explained in the last section of this thesis as it requires the quantification $\Delta\mu$ as a function of the bias.

4.1.4 $\Delta\mu$ under electrical bias

Similarly, $\Delta\mu$ of the QWs as a function of the applied bias can be calculated from the PL spectra. It is plotted in Fig. 4.6a for different absorbed powers from 5000

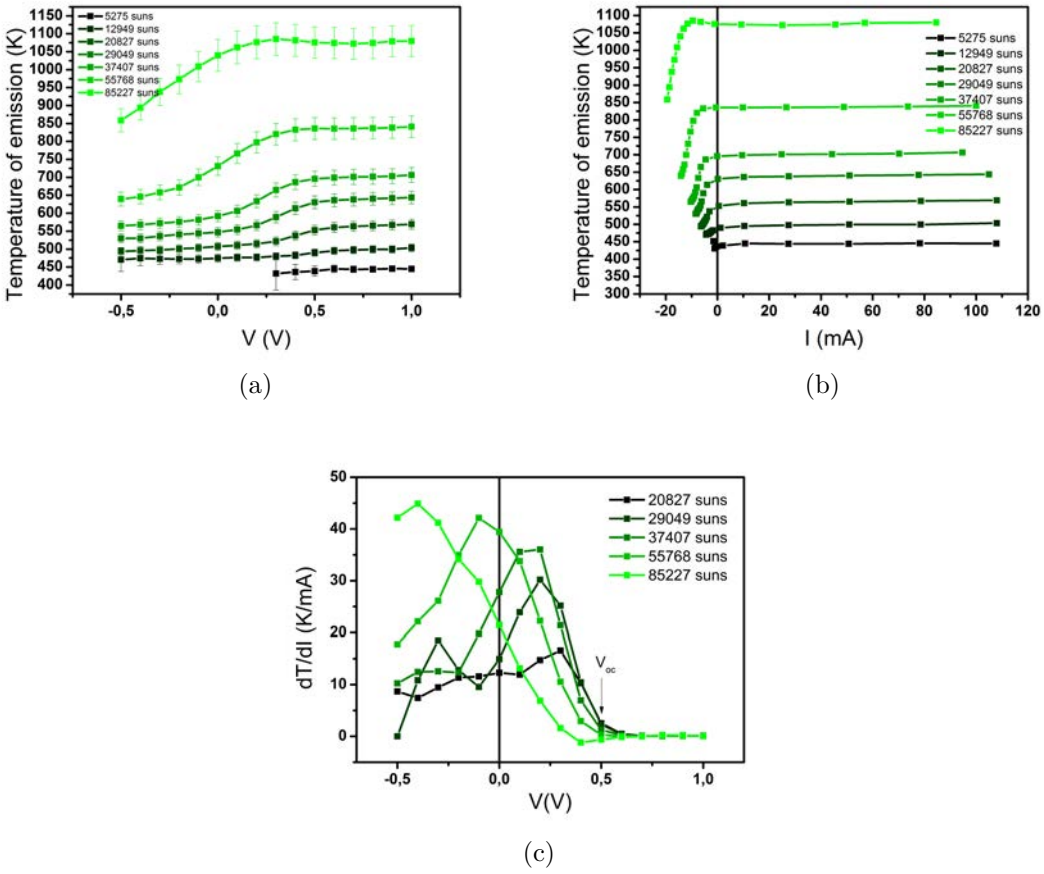


Figure 4.5 – Temperature of emission of the QWs as a function of the applied bias (a) or the current (b) for different illumination powers. Derivative of emission temperature in the wells as a function of the current (c).$\lambda = 975nm$, sample 2757

to 85000 suns (from black to green). All $\Delta\mu$ (except the highest power) increases as the bias increases before reaching a plateau. For the highest absorbed power, it decreases before increasing and then it also reaches a plateau. One can also note as the absorbed power increases up to 37000 suns, $\Delta\mu$ shows a saturation and then decreases at the two highest powers.
The current can be plotted as a function of $\Delta\mu$, which is similar to a classical IV curves. In fact, $\Delta\mu$ will represent the maximum open circuit voltage so it is not affected by series resistances 4.6b. As the absorbed power increases up to 37000 suns, both the open circuit voltage and the photo-current increases. At higher powers the equivalent "open circuit voltage" decreases. This behaviour is not expected unless the cell heats up, but it was shown in section 3.2.1 the device is close to ambient temperature. However, this behaviour can be explained thanks to the determination of $\Delta\mu$ in the barriers.

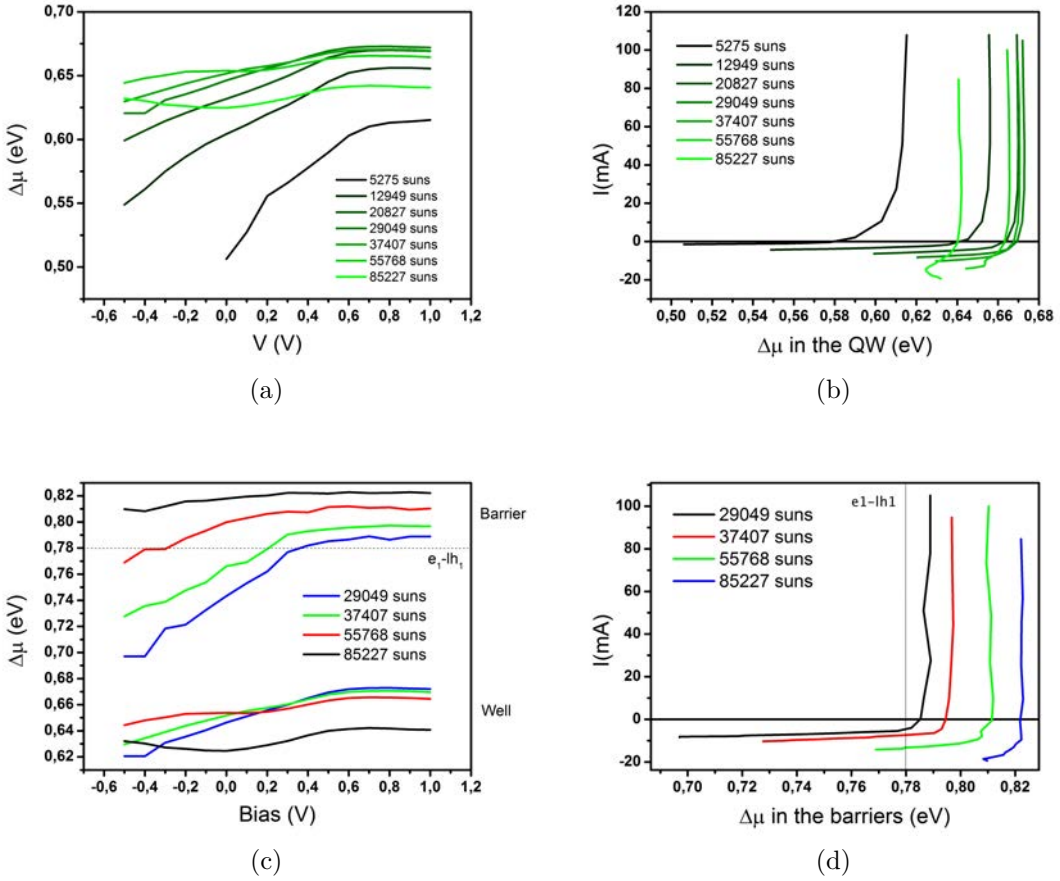
Indeed, it was seen in the previous chapter $\Delta\mu$ of the barriers could be also determined. $\Delta\mu$(V) and I($\Delta\mu$) of the barriers were plotted in Fig. 4.6c and Fig. 4.6d for the four highest powers, as the PL intensity of the barriers is too low to be detected at lower powers.
In Fig. 4.6c, $\Delta\mu$, which were saturating within the QWs at high powers are no longer saturating in the barriers. It indicates an effective transfer of hot carriers from the hot (QWs) to the cold (barriers) reservoir. If one focus on I($\Delta\mu$) curves in Fig. 4.6d, one can see the area under the curve at negative current increases with the absorbed power, which was not true in the QWs for similar powers. It means there is an increase of the power delivered by the cell with the absorbed powers. For that matter, the internal conversion efficiency was calculated from the following equation:

$$\eta_I = \eta/A = I\Delta\mu_b/(P_{inc}S_{spot}A) \tag{4.6}$$

where A is the absorbance taken from EQE at 0.26 for $\lambda = 975nm$, η the conversion efficiency, P_{inc} the incident power, S_{spot} the illumination area. Remark that $\Delta\mu_b$ was used instead of the electrical bias V in the internal efficiency formula in order to overcome artefact due to the inhomogeneous illumination.

The difference between the internal conversion efficiency and the conversion efficiency is that the incident power is replaced by the absorbed power. The aim is to have a better idea of the efficiency we would get if we were not limited by the material absorbance, reflection or interferences which can be solved a posteriori by light management.

Thus, one can see the internal efficiency as function of the bias for different powers in Fig. 4.7. All the curves shows a decrease of the efficiency as a function



(a) (b)

(c) (d)

Figure 4.6 – $\Delta\mu$ of the QWs as a function of the applied bias for different illumination powers (a). Corresponding current as function of $\Delta\mu$ of the QWs (b). $\Delta\mu$ of the QWs and the barriers as a function of the applied bias for different illumination powers (c). Corresponding current as function of $\Delta\mu$ of the barriers (d). $\lambda = 975\,nm$, sample 2757.

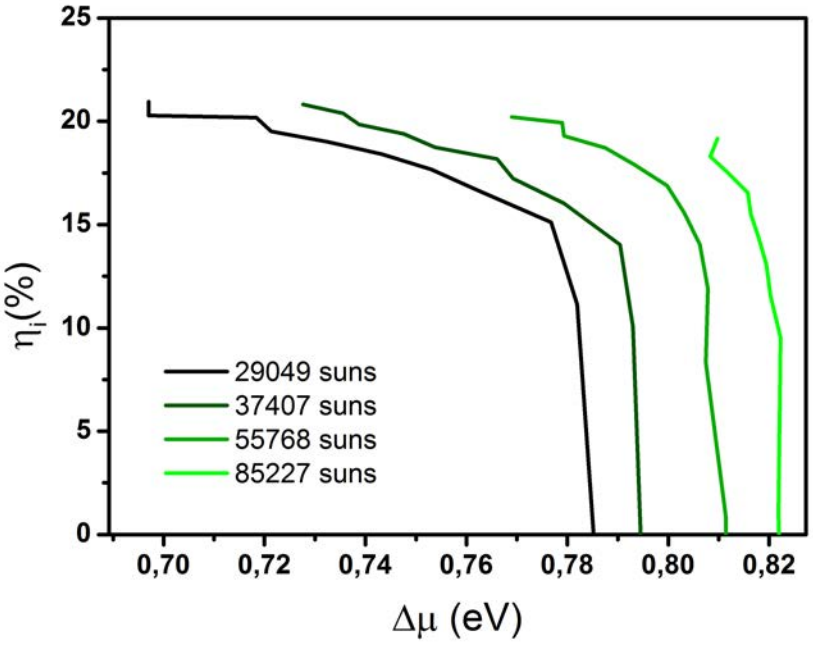


Figure 4.7 – Internal conversion efficiency as a function of $\Delta\mu$ of the barriers as the absorbed powers increases (from black to green. These curves are obtained from optical measurements on confocal set-up calibrated thanks to the hyperspectral.

of $\Delta\mu$ in the barriers. These curves can be compared to the efficiency curves as a function of the concentration in logarithmic scale, seen in Fig. 1.13, where a maximum output power point can be found. As the slopes are all decreasing, it means the maximum working point were not acquired, and might be found at lower $\Delta\mu$; except for the curve at 29000 suns, which saturates at 20%. Therefore, the internal conversion efficiency would range between 20% to 25% as absorbed power increases from 29000 to 85000 suns. Minimum internal conversion efficiencies were calculated thanks to optoelectronic measurements. Values are minimum ones, as $\Delta\mu$ and the temperature were determined from confocal collection area, which was shown to underestimated the performances, see section 3.1.2.

This is a very interesting result as it shows the HCSC made of semi-selective contacts in a pin diode is effective. However some questions need to be answered. Can we predict the behaviour we observed thanks to the simulation? Why the IV curves are so different from the I($\Delta\mu$) of the barriers. We will propose first explanations in the next sections.

4.2 Simulation of thermodynamic quantities under electrical bias

The simulation aims to better understand the experimental results on the thermodynamic quantities under electrical bias. Those quantities in the QWs were simulated as a function of the electrical bias from -0.5 V to 1.1 V. Simulations were done for different absorbed powers ranging from 26000 to 70000 suns (respectively from green to black) so that it corresponds to the experimental results were $\Delta\mu$ in the barrier could be measured. Indeed, as seen in the previous section, $\Delta\mu$ in the barrier is representative of an effective electrical bias without being affected by collection degradation effects. Firstly, the temperature of emission in the QWs will be simulated as function of the electrical bias and compared to the experiments. Secondly, an analogous simulation of $\Delta\mu$ in the QWs will performed discussed.

4.2.1 Comparison between simulated and experimental temperatures

It was introduced in the model definition section 2.5.1 that the only adjustable parameter is the conductance, meaning that all the others parameters are known or probed (gap, excitation energy, extraction energy, thermalisation rate...). As a consequence, conductance was varied on a wide range starting from $1\times10^5\,\Omega^{-1}.cm^{-2}$ to $1\times10^{20}\,\Omega^{-1}.cm^{-2}$. Only the simulation performed at $2\times10^{14}\,\Omega^{-1}.cm^{-2}$ will be represented in Fig. 4.8a, as it best matches the temperature under electrical bias experiments. At low electrical biases $V<0.8V$, temperatures increase from 460 K to 600 K with the absorbed powers. This is a classical trend that is seen experimentally and discuss in chapter 3. Then, all the curves show a threshold at around 0.9 V. Probed temperatures shows the same behaviour in Fig. 4.8b with increasing $\Delta\mu_b$. The temperature increase is correlated to the I-V (I-$\Delta\mu_b$) behaviour. In fact, as the voltage ($\Delta\mu_b$) increases above 0.9V (0.78 eV) the extracted current diminishes. It arises a reduction of the exchange between the absorber and the cold reservoir which, induce a temperature of emission increase.

The main difference between simulations and experiments is the lower threshold value at 0.78 eV in the experiments instead of 0.9 V in the simulation. This difference can also be found on the IV characteristics: simulated open circuit voltage is higher than the experimental one, as the simulation is performed under ideal conditions, i.e. absences of Auger/Impact ionization, non radiative recombination. Consequently, the experimental temperature threshold is shifted to lower bias com-

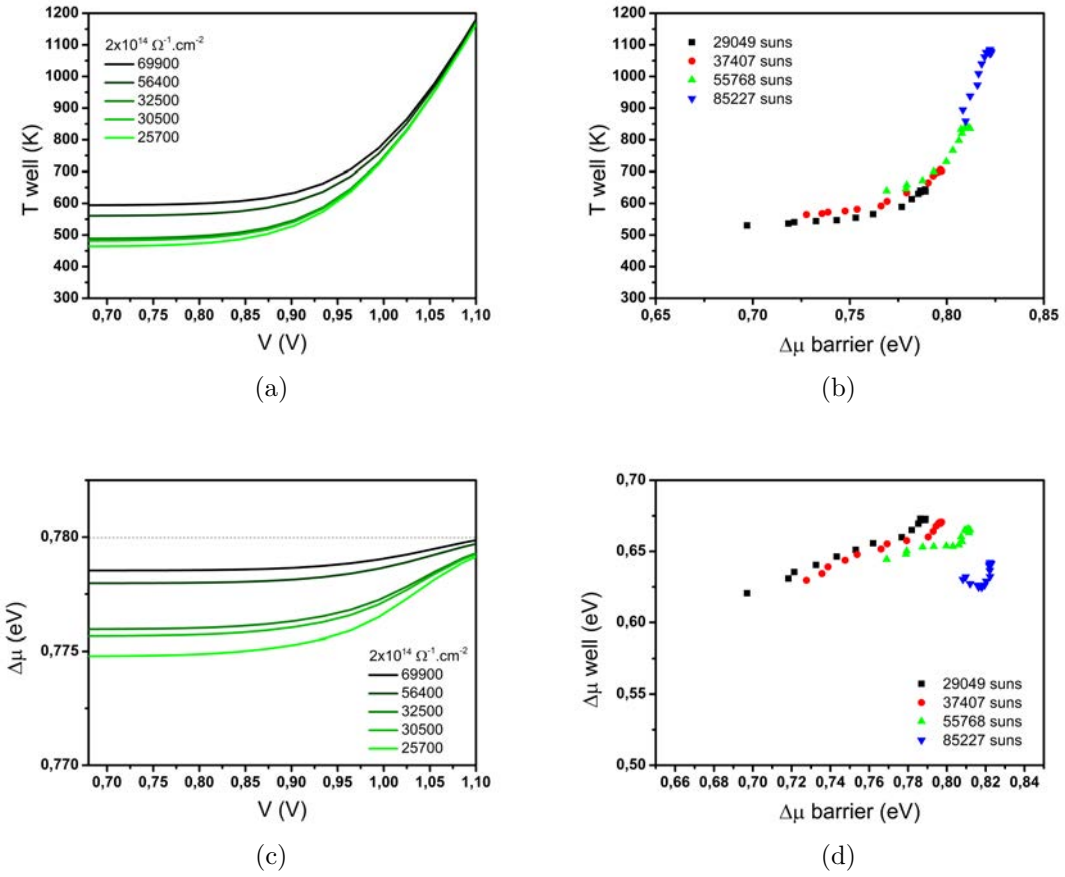


Figure 4.8 – Simulated (a,c) and experimental (b,d) temperatures of emission and $\Delta\mu$ of the QWs as a function of the electrical bias for different absorbed powers. Sample 2757, excitation wavelength 975 nm.

pared to the simulation. Another explanation could come from the fact that $\Delta\mu_b$ is used instead of V. The equality $\Delta\mu_b = qV$ could not hold anymore [96], for example if QWs/barrier interaction is taken into account.

Other similar simulations were performed by changing the conductance values and have shown the following trends. Below $1\times10^{10}\Omega^{-1}.cm^{-2}$, there was no variation of the temperature whatever the powers and electrical biases. Then, beyond $1 \times 10^{15}\,\Omega^{-1}.cm^{-2}$, the temperature in the absorber become close to room temperature whatever the electrical biases and powers. If the conductance is lower than $1 \times 10^{10}\,\Omega^{-1}.cm^{-2}$ the carriers are almost not extracted (short circuit currents are 2 at 3 order of magnitude lower than at a conductance of $2 \times 10^{14}\,\Omega^{-1}.cm^{-2}$) in the electrical bias range of simulation. Then, beyond $1 \times 10^{15}\,\Omega^{-1}.cm^{-2}$ the carriers are extracted so fast that most of them thermalise in the contacts. Thus, due to a very low carrier density in the wells, the temperature in the well becomes close to room temperature. In the intermediate range of conductance, carriers exchanges between the absorber and the contacts are allowed and the temperature variations can be correlated to the current variation.

4.2.2 Comparison between simulated and experimental $\Delta\mu$

Similarly, $\Delta\mu$ in the well are simulated and plotted as a function of the electrical bias in Fig. 4.8c (experimental data are displayed in Fig. 4.8d). The conductance value was set at $2 \times 10^{14}\,\Omega^{-1}.cm^{-2}$ according to the previous simulations on the temperature. Similarly, $\Delta\mu$ in the absorber is unvarying in the range where the temperature was constant. Then, $\Delta\mu$ increases with the bias after the same threshold value, found in previous section. Note that $\Delta\mu$ variation is very low according to the absorbed power range considered here (from 26000 to 70000 suns). Then, the more $\Delta\mu$ increases the less $\Delta\mu$ varies as a function of the electrical bias i.e. $\Delta\mu$ saturates to a value close to V_{oc}^{rad} (0.78 eV). One can see the variations between simulated $\Delta\mu$ and temperatures are strongly correlated. This can be explained, as $\Delta\mu$ and temperature of emission dependences to the absorbed power are respectively linear (Eq. (1.3) if exponential term is neglected; valid at high temperature of emission) and logarithmic (Eq. (3.1)). Let us remark that assuming $qV = \Delta\mu_b$ is a strong assumption that needs to be substantiated.

To conclude, behaviour between simulation and experiments is obviously different. The model that was used for the simulation becomes too simplistic to describe these evolutions and requires the definition of a new model, which would take into account interactions between both $\Delta\mu$ in the QWs and the barriers.

In this chapter, it was seen that the classical IV curves made on that hot carrier device suffer from collection degradation. In order to overcome these issues in the performances determination, a study on V_{oc} was proposed. It has established that the inhomogeneous illumination which, is required to reach high concentrations, induces a V_{oc} drop (dark current contribution).

Then, it was shown that the acquisition of thermodynamic quantities as a function of the electrical bias could be obtained thanks to the absolute PL spectra measurements. Interpretations of these curves were strongly limited by the collection degradation, which were overcome through the use of $\Delta\mu$ in the barrier instead of the electrical bias. It allowed to quantify internal conversion efficiencies of the device.

At last, in order to better understand the experiments, the thermodynamic quantities were simulated and it was shown that general trends could be obtained. Still, the simplistic model and the non trivial assumption $qV = \Delta\mu_b$ limits the interpretation. A new model should be developed.

Electrical characterisation are still complex and it shows the usefulness of optical characterisation, which are not limited by device issues. In the future, there is a necessity to reduce hot carrier device areas so that, from an optical point of view, the homogeneous and concentrated illumination would be easily achievable. From an electrical point of view, not only it will reduce sheet resistance effects and facilitate electrical management but it will also limit the residual lattice heating (not supposed to happen in an efficient HCSC) [97]. The next step in the making of the HCSC is the development of efficient semi-selective contacts or selective contacts, as it was highlighted in this thesis that the thermalisation rate is no longer the limiting parameter.

Short summary - In this chapter, it was seen that it is possible to control the thermodynamic quantities as a function of the electrical bias thanks to the simultaneous acquisition of PL spectra. The evolution of these fundamental thermodynamic quantities under relevant working conditions for solar cells was done for the first time. It allowed to propose first explanations of such a hot carrier device. Preliminary results of simulation allowed to partially understand the device behaviour under an applied bias and pointed out the limits of the model that was used. In this regards, the latter should be refined so the interaction between wells and barriers can be treated correctly. Secondly, the effect of the device size on the performances has shown to strongly affect the performances and should be considered in the future device design.

Conclusion

Main results

The centre of the manuscript focused on opto-electronic characterisation of hot carrier absorbers in operating solar cell relevant conditions. First of all, hot carriers were spatially resolved through the determination of thermodynamic quantities governing the current and power balance equations.
Not only, the thermodynamic quantities were evaluated but strong thermalisation reduction was demonstrated in InGaAsP MQWs absorbers: thermalisation rate decreased to 4 $W/K/cm^2$ and temperature of emission reached 670 K at only 14000 suns equivalent.
Through a wide study on various InGaAsP structures, a statistic analysis not only confirmed the linear dependence of the thermalisation rate to the absorber thickness (even in MQWs device), but attested not to be depend on material parameters and only on geometrical ones. It is the first time that such a wide sample study is performed.
Then, it was demonstrated the absorber thermalisation is no longer the limiting parameter in the establishment of a hot carrier solar cell, by estimating a potential output voltage under 14000 suns at 0.9 V in a 0.78 eV band gap absorber, corresponding to a 50% potential conversion efficiency (isentropic condition). Contactless measurement overcame the lack of ESC, which allows to understand that the research effort shall continue in their development. Indeed, the effective transfer of hot carriers from the MQWs absorber to the barrier was evidenced. Thereafter, optical IV curves presented internal conversion efficiencies close to 25%.

Perspectives

Potential explanation of the latter performances could be done, thanks to optoelectronic measurement and has shown the device size should be considerably downsized so the proof of concept may be made. Thereafter, measuring a photo-Seebeck coefficient locally was an innovative approach. It brings closer the photovoltaics field from the thermoelectric one, and it demonstrates its full interest, in the determination of absorber/ESC entropies exchange.

Bibliography

[1] J. Wu and Z. M. Wang, *Quantum Dot Solar Cells*. New York: Springer-Verlag New York Inc., Sept. 2013.

[2] IRENA, "Renewable energy technologies: cost analysis series," June 2012.

[3] G. Masson, S. Orlandi, and M. Rekinger, "Global market outlook for photovoltaics 2014-2018," 2014.

[4] "PV innovations: Emerging and innovative approches in photovoltaics," June 2014.

[5] D. Feldman, G. Barbose, R. Wiser, N. Darghouth, and A. Goodrich, "Photovoltaic pricing trends: historical, recent, and near-term projections," Tech. Rep. DOE/GO-102012-3839, National Renewable Energy Laboratory, 15013 Denver West Parkway Golden, CO 80401 303-275-3000, Nov. 2012.

[6] L. C. Hirst and N. J. Ekins-Daukes, "Fundamental losses in solar cells," *Progress in Photovoltaics: Research and Applications*, vol. 19, pp. 286–293, May 2011.

[7] A. Martí and G. L. Araújo, "Limiting efficiencies for photovoltaic energy conversion in multigap systems," *Solar Energy Materials and Solar Cells*, vol. 43, pp. 203–222, Sept. 1996.

[8] A. L. Bris, *Étude de faisabilité d'un dispositif photovoltaïque à porteurs chauds*. PhD thesis, Ecole Centrale Paris, Sept. 2011.

[9] D. König, D. Hiller, M. Zacharias, S. Michard, and C. Flynn, "Static hot carrier populations as a function of optical excitation energy detected through energy selective contacts by optically assisted IV," *Progress in Photovoltaics: Research and Applications*, vol. 2367, 2013.

[10] S. Yagi and Y. Okada, "Fabrication of resonant tunneling structures for selective energy contact of hot carrier solar cell based on III-v semiconductors," in *2010 35th IEEE Photovoltaic Specialists Conference (PVSC)*, pp. 001213–001216, June 2010.

[11] A. L. Bris, L. Lombez, S. Laribi, G. Boissier, P. Christol, and J.-F. Guillemoles, "Thermalisation rate study of GaSb-based heterostructures by continuous wave photoluminescence and their potential as hot carrier solar cell absorbers," *Energy & Environmental Science*, vol. 5, pp. 6225–6232, Mar. 2012.

[12] V. Smil, *Energy: A Beginner's Guide*. Oxford: Oneworld Publications, May 2006.

[13] L'énerGeek, "Comment l'allemagne a produit la moitié de son électricité avec du solaire | l'ENERGEEK : l'énergie facile en quelques clics !."

[14] Fraunhofer, "Photovoltaics report," tech. rep., Dec. 2012.

[15] Semprius, "Semprius - semprius' 35.5 percent efficiency sets new record for commercially available solar modules," Sept. 2013.

[16] P. Würfel, "Solar energy conversion with hot electrons from impact ionisation," *Solar Energy Materials and Solar Cells*, vol. 46, pp. 43–52, Apr. 1997.

[17] R. T. Ross and A. J. Nozik, "Efficiency of hot-carrier solar energy converters," *Journal of Applied Physics*, vol. 53, pp. 3813–3818, May 1982.

[18] Enerdata, "Research on energy efficiency, CO2 emissions, energy consumption, forecast.."

[19] EU-JRC, "Photovoltaic geographical information system," 2012.

[20] P. Wurfel, "The chemical potential of radiation," *Journal of Physics C: Solid State Physics*, vol. 15, pp. 3967–3985, June 1982.

[21] M. A. Green, *Third Generation Photovoltaics: Advanced Solar Energy Conversion*. Springer-Verlag Berlin and Heidelberg GmbH & Co. K, Aug. 2005.

[22] W. Shockley and H. J. Queisser, "Detailed balance limit of efficiency of p-n junction solar cells," *Journal of Applied Physics*, vol. 32, no. 3, pp. 510–519, 1961.

[23] P. Würfel, *Physics of Solar Cells: From Basic Principles to Advanced Concepts*. Weinheim: Wiley VCH, edition : 2 upd exp ed., Feb. 2009.

[24] P. Würfel, "Thermodynamic limitations to solar energy conversion," *Physica E: Low-dimensional Systems and Nanostructures*, vol. 14, pp. 18–26, Apr. 2002.

[25] E. D. Jackson, "Areas for improvement of the semiconductor solar energy converter," in *Transactions of the Conference on the Use of Solar Energy*, vol. 5, pp. 122–126, 1955.

[26] R. L. Moon, L. W. James, H. A. Vander Plas, T. O. Yep, G. A. Antypas, and Y. Chai, "Multigap solar cell requirements and the performance of AlGaAs and si cells in concentrated sunlight," in *13th Photovoltaic Specialists Conference*, vol. 1, pp. 859–867, 1978.

[27] T. Adachi, Y. Hamakawa, Y. Nitta, and H. Okamoto, "Photovoltaic device," June 1981. US Patent 4,271,328.

[28] M. A. Green, K. Emery, Y. Hishikawa, W. Warta, and E. D. Dunlop, "Solar cell efficiency tables (version 43)," *Progress in Photovoltaics: Research and Applications*, vol. 22, pp. 1–9, Jan. 2014.

[29] F. Dimroth, M. Grave, P. Beutel, U. Fiedeler, C. Karcher, T. N. D. Tibbits, E. Oliva, G. Siefer, M. Schachtner, A. Wekkeli, A. W. Bett, R. Krause, M. Piccin, N. Blanc, C. Drazek, E. Guiot, B. Ghyselen, T. Salvetat, A. Tauzin, T. Signamarcheix, A. Dobrich, T. Hannappel, and K. Schwarzburg, "Wafer bonded four-junction GaInP/GaAs/GaInAsP/GaInAs concentrator solar cells with 44.7% efficiency," *Progress in Photovoltaics: Research and Applications*, vol. 22, pp. 277–282, Mar. 2014.

[30] P. Faine, S. R. Kurtz, C. Riordan, and J. M. Olson, "The influence of spectral solar irradiance variations on the performance of selected single-junction and multijunction solar cells," *Solar Cells*, vol. 31, pp. 259–278, June 1991.

[31] D. N. Mirlin, I. J. Karlik, L. P. Nikitin, I. I. Reshina, and V. F. Sapega, "Hot electron photoluminescence in GaAs crystals," *Solid State Communications*, vol. 37, pp. 757–760, Mar. 1981.

[32] C. L. Collins and P. Y. Yu, "Generation of nonequilibrium optical phonons in GaAs and their application in studying intervalley electron-phonon scattering," *Physical Review B*, vol. 30, pp. 4501–4515, Oct. 1984.

[33] A. Othonos, "Probing ultrafast carrier and phonon dynamics in semiconductors," *Journal of Applied Physics*, vol. 83, pp. 1789–1830, Feb. 1998.

[34] P. G. Klemens, "Anharmonic decay of optical phonons," *Physical Review*, vol. 148, pp. 845–848, Aug. 1966.

[35] G. J. Conibeer, R. Patterson, P. Aliberti, H. Xia, S. Huang, D. König, B. Puthen Veettil, S. Shrestha, and M. A. Green, "Hot carrier solar cells: Choice of materials for efficiency and abundance," *26th European Photovoltaic Solar Energy Conference and Exhibition*, pp. 28 – 32, 2011.

[36] A. Debernardi, "Phonon linewidth in III-v semiconductors from density-functional perturbation theory," *Physical Review B*, vol. 57, pp. 12847–12858, May 1998.

[37] H. Levard, S. Laribi, and J.-F. Guillemoles, "Optical phonon decay in cubic semiconductors: a hot carrier solar cell picture," *Proc. SPIE8981*, pp. 89810H–89810H–8, 2014.

[38] Z. Y. Xu and C. L. Tang, "Picosecond relaxation of hot carriers in highly photoexcited bulk GaAs and GaAs-AlGaAs multiple quantum wells," *Applied Physics Letters*, vol. 44, pp. 692–694, Apr. 1984.

[39] J. F. Ryan, R. A. Taylor, A. J. Turberfield, A. Maciel, J. M. Worlock, A. C. Gossard, and W. Wiegmann, "Time-resolved photoluminescence of two-dimensional hot carriers in GaAs-AlGaAs heterostructures," *Physical Review Letters*, vol. 53, pp. 1841–1844, Nov. 1984.

[40] J. Shah, A. Pinczuk, A. C. Gossard, and W. Wiegmann, "Energy-loss rates for hot electrons and holes in GaAs quantum wells," *Physical Review Letters*, vol. 54, pp. 2045–2048, May 1985.

[41] K. Leo, W. W. Rühle, H. J. Queisser, and K. Ploog, "Reduced dimensionality of hot-carrier relaxation in GaAs quantum wells," *Physical Review B*, vol. 37, pp. 7121–7124, Apr. 1988.

[42] K. Leo, W. W. Rühle, and K. Ploog, "Hot-carrier energy-loss rates in GaAs/AlxGa1-xAs quantum wells," *Physical Review B*, vol. 38, pp. 1947–1957, July 1988.

[43] B. K. Ridley, "Electron scattering by confined LO polar phonons in a quantum well," *Physical Review B*, vol. 39, pp. 5282–5286, Mar. 1989.

[44] J. K. Jain and S. Das Sarma, "Role of discrete slab phonons in carrier relaxation in semiconductor quantum wells," *Physical Review Letters*, vol. 62, pp. 2305–2308, May 1989.

[45] P. Lugli and S. M. Goodnick, "Nonequilibrium longitudinal-optical phonon effects in GaAs-AlGaAs quantum wells," *Physical Review Letters*, vol. 59, pp. 716–719, Aug. 1987.

[46] W. S. Pelouch, R. J. Ellingson, P. E. Powers, C. L. Tang, D. M. Szmyd, and A. J. Nozik, "Comparison of hot-carrier relaxation in quantum wells and bulk GaAs at high carrier densities," *Physical Review B*, vol. 45, pp. 1450–1453, Jan. 1992.

[47] Y. Rosenwaks, M. C. Hanna, D. H. Levi, D. M. Szmyd, R. K. Ahrenkiel, and A. J. Nozik, "Hot-carrier cooling in GaAs: Quantum wells versus bulk," *Physical Review B*, vol. 48, pp. 14675–14678, Nov. 1993.

[48] D. J. Westland, J. F. Ryan, M. D. Scott, J. I. Davies, and J. R. Riffat, "Hot carrier energy loss rates in GaInAs/InP quantum wells," *Solid-State Electronics*, vol. 31, pp. 431–434, Mar. 1988.

[49] A. V. Akimov, S. A. Cavill, A. J. Kent, N. M. Stanton, T. Wang, and S. Sakai, "Phonon emission by photoexcited carriers in InGaN/GaN multiple quantum wells," *Journal of Physics: Condensed Matter*, vol. 14, p. 3445, Apr. 2002.

[50] G. J. Conibeer, D. König, M. A. Green, and J. F. Guillemoles, "Slowing of carrier cooling in hot carrier solar cells," *Thin Solid Films*, vol. 516, pp. 6948–6953, Aug. 2008.

[51] R. Patterson, M. Kirkengen, B. Puthen Veettil, D. Konig, M. Green, and G. Conibeer, "Phonon lifetimes in model quantum dot superlattice systems with applications to the hot carrier solar cell," *Solar Energy Materials and Solar Cells*, vol. 94, pp. 1931–1935, Nov. 2010.

[52] D. Sun, G. Aivazian, A. M. Jones, J. S. Ross, W. Yao, D. Cobden, and X. Xu, "Ultrafast hot-carrier-dominated photocurrent in graphene," *Nat Nano*, vol. advance online publication, Jan. 2012.

[53] K. J. Tielrooij, J. C. W. Song, S. A. Jensen, A. Centeno, A. Pesquera, A. Zurutuza Elorza, M. Bonn, L. S. Levitov, and F. H. L. Koppens, "Photoexcitation cascade and multiple hot-carrier generation in graphene," *Nature Physics*, vol. advance online publication, Feb. 2013.

[54] J. F. Guillemoles, G. Conibeer, and M. Green, "Phononic engineering with nanostructures for hot carrier solar cells," in *arXiv:cond-mat/0611045*, (Shangai), 2005. arXiv: cond-mat/0611045.

[55] D. J. Farrell, Y. Takeda, K. Nishikawa, T. Nagashima, T. Motohiro, and N. J. Ekins-Daukes, "A hot-carrier solar cell with optical energy selective contacts," *Applied Physics Letters*, vol. 99, p. 111102, Sept. 2011.

[56] W. A. Tisdale, K. J. Williams, B. A. Timp, D. J. Norris, E. S. Aydil, and X.-Y. Zhu, "Hot-electron transfer from semiconductor nanocrystals," *Science*, vol. 328, pp. 1543–1547, June 2010.

[57] G. J. Conibeer, C. W. Jiang, D. König, S. Shrestha, T. Walsh, and M. A. Green, "Selective energy contacts for hot carrier solar cells," *Thin Solid Films*, vol. 516, pp. 6968–6973, Aug. 2008.

[58] D. König, D. Hiller, M. Zacharias, S. Michard, and C. Flynn, "Static hot carrier populations as a function of optical excitation energy detected through energy selective contacts by optically assisted IV," *Progress in Photovoltaics: Research and Applications*, vol. 2367, 2013.

[59] J. A. R. Dimmock, S. Day, M. Kauer, K. Smith, and J. Heffernan, "Demonstration of a hot-carrier photovoltaic cell," *Progress in Photovoltaics: Research and Applications*, no. 2444, 2013.

[60] A. Le Bris and J. F. Guillemoles, "Hot carrier solar cell efficiency simulation with carrier extraction through non ideal selective contacts," in *2010 35th IEEE Photovoltaic Specialists Conference (PVSC)*, pp. 000061–000064, IEEE, June 2010.

[61] P. Würfel, A. S. Brown, T. E. Humphrey, and M. A. Green, "Particle conservation in the hot-carrier solar cell," *Progress in Photovoltaics: Research and Applications*, vol. 13, pp. 277–285, June 2005.

[62] Y. P. Varshni, "Temperature dependence of the energy gap in semiconductors," *Physica*, vol. 34, no. 1, pp. 149–154, 1967.

[63] A. Delamarre, L. Lombez, and J.-F. Guillemoles, "Contactless mapping of saturation currents of solar cells by photoluminescence," *Applied Physics Letters*, vol. 100, pp. 131108–131108–3, Mar. 2012.

[64] S. M. Sze and K. K. Ng, *Physics of Semiconductor Devices*. Hoboken, N.J: Wiley-Blackwell, 3rd edition edition ed., Nov. 2006.

[65] S. A. Lyon, "Spectroscopy of hot carriers in semiconductors," *Journal of luminescence*, vol. 35, no. 3, pp. 121–154, 1986.

[66] W. Zhao, S. Kim, J. Zhang, and I. Adesida, "Thermally stable ge/ag/ni ohmic contact for InAlAs/InGaAs/InP HEMTs," *IEEE Electron Device Letters*, vol. 27, no. 1, pp. 4–6, 2006.

[67] C. D. Matos, A. L. Corre, H. L'Haridon, S. Gosselin, and B. Lambert, "Fe-doped InGaAs/InGaAsP photorefractive multiple quantum well devices operating at 1.55 μm," *Applied Physics Letters*, vol. 70, pp. 3591–3593, June 1997.

[68] A. Marceaux, S. Loualiche, O. Dehaese, and B. Lambert, "High-speed 1.55 μm fe-doped multiple-quantum-well saturable absorber on InP," *Applied Physics Letters*, vol. 78, pp. 4065–4067, June 2001.

[69] C. Levallois, V. Verbrugge, L. Dupont, J.-L. de Bougrenet de la Tocnaye, B. Caillaud, A. Le Corre, O. Dehaese, H. Folliot, and S. Loualiche, "1.55-μm optically pumped tunable VCSEL based on a nano-polymer dispersive liquid crystal phase modulator," vol. 6185, pp. 61850W–61850W–9, 2006.

[70] C. Levallois, A. L. Corre, O. Dehaese, H. Folliot, C. Paranthoen, C. Labbé, and S. Loualiche, "Design and fabrication of GaInAsP/InP VCSEL with two a-si/a-SiN x bragg reflectors," *Optical and Quantum Electronics*, vol. 38, pp. 281–291, Mar. 2006.

[71] J. Stark, "Beobachtungen über den effekt des elektrischen feldes auf spektrallinien. i. quereffekt," *Annalen der Physik*, vol. 348, no. 7, pp. 965–982, 1914.

[72] L. C. Chiu and A. Yariv, "Auger recombination in quantum-well InGaAsP heterostructure lasers," *IEEE Journal of Quantum Electronics*, vol. 18, no. 10, pp. 1406–1409, 1982.

[73] "JMP logiciel de découverte statistique de SAS."

[74] A. Le Bris, L. Lombez, S. Laribi, J. Guillemoles, C. Colin, S. Collin, J. Pelouard, M. Laroche, R. Esteban, J.-J. Greffet, G. Boissier, and P. Christol, "Hot carrier solar cells: Controlling thermalization in ultra thin devices," in *2011 37th IEEE Photovoltaic Specialists Conference (PVSC)*, pp. 001913–001913, 2011.

[75] A. Le Bris, J. Rodiere, C. Colin, S. Collin, J.-L. Pelouard, R. Esteban, M. Laroche, J.-J. Greffet, and J.-F. Guillemoles, "Hot carrier solar cells: Controlling thermalization in ultrathin devices," *IEEE Journal of Photovoltaics*, vol. 2, no. 4, pp. 506–511, 2012.

[76] M. Bass, V. N. Mahajan, E. W. Van Stryland, G. Li, C. A. MacDonald, C. DeCusatis, and Optical Society of America, *Handbook of optics*. New York: McGraw-Hill, 2010.

[77] M. Muñoz, T. M. Holden, F. H. Pollak, M. Kahn, D. Ritter, L. Kronik, and G. M. Cohen, "Optical constants of in0.53ga0.47as/InP: Experiment and modeling," *Journal of Applied Physics*, vol. 92, pp. 5878–5885, Oct. 2002.

[78] S. Adachi, "Optical properties of InGaAsP alloys," *Physical Review B*, vol. 39, pp. 12612–12621, June 1989.

[79] S. Adachi, "Optical dispersion relations for GaP, GaAs, GaSb, InP, InAs, InSb, AlxGa1-xAs, and in1-xGaxAsyP1-y," *Journal of Applied Physics*, vol. 66, pp. 6030–6040, Dec. 1989.

[80] T. Mei, "Interpolation of quaternary III-v alloy parameters with surface bowing estimations," *Journal of Applied Physics*, vol. 101, p. 013520, Jan. 2007.

[81] P. W\ürfel, *Physics of solar cells*. Wiley Online Library, 2005.

[82] L. Onsager, "Reciprocal relations in irreversible processes. i.," *Physical Review*, vol. 37, no. 4, p. 405, 1931.

[83] J. Cai and G. D. Mahan, "Effective seebeck coefficient for semiconductors," *Physical Review B*, vol. 74, p. 075201, Aug. 2006.

[84] J. Martin, T. Tritt, and C. Uher, "High temperature seebeck coefficient metrology," *Journal of Applied Physics*, vol. 108, pp. 121101–121101–12, Dec. 2010.

[85] M. Zebarjadi, A. Shakouri, and K. Esfarjani, "Thermoelectric transport perpendicular to thin-film heterostructures calculated using the monte carlo technique," *Physical Review B*, vol. 74, p. 195331, Nov. 2006.

[86] C. Wood, D. Zoltan, and G. Stapfer, "Measurement of seebeck coefficient using a light pulse," *Review of Scientific Instruments*, vol. 56, pp. 719–722, May 1985.

[87] A. Ibragimov, "Semi-analytical model for the seebeck coefficient in semiconductors with isotropic DOS given by a power function," *The European Physical Journal B*, vol. 85, pp. 1–11, Nov. 2012.

[88] K. Seeger, *Semiconductor Physics: An Introduction*. Berlin ; New York: Springer, 9th edition ed., June 2004.

[89] R. Scheer, *Chalcogenide Photovoltaics: Physics, Technologies, and Thin Film Devices*. Weinheim, Germany: Wiley-VCH, 1 edition ed., Mar. 2011.

[90] J. Nelson, *The Physics of Solar Cells*. Imperial College Press, Jan. 2003.

[91] S. R. Dhariwal, S. Mittal, and R. K. Mathur, "Theory for voltage dependent series resistance in silicon solar cells," *Solid-State Electronics*, vol. 27, pp. 267–273, Mar. 1984.

[92] V. L. Malevich, "Dynamics of photoinduced field screening; THz-pulse and second harmonic generation from semiconductor surface," *Surface Science*, vol. 454–456, pp. 1074–1078, May 2000.

[93] T. H. Wood, J. Z. Pastalan, C. A. B. Jr, B. C. Johnson, B. I. Miller, J. L. deMiguel, U. Koren, and M. G. Young, "Electric field screening by photogenerated holes in multiple quantum wells: A new mechanism for absorption saturation," *Applied Physics Letters*, vol. 57, pp. 1081–1083, Sept. 1990.

[94] A. Luque, G. Sala, and J. C. Arboiro, "Electric and thermal model for non-uniformly illuminated concentration cells," *Solar Energy Materials and Solar Cells*, vol. 51, pp. 269–290, Feb. 1998.

[95] U. Rau, D. Abou-Ras, and T. Kirchartz, *Advanced Characterization Techniques for Thin Film Solar Cells*. John Wiley & Sons, May 2011.

[96] A. Delamarre, M. Paire, J.-F. Guillemoles, and L. Lombez, "Quantitative luminescence mapping of cu(in,ga)se2 thin films solar cells (in press)," *Progress in Photovoltaics: Research and Applications*.

[97] M. Paire, L. Lombez, N. Péré-Laperne, S. Collin, J.-L. Pelouard, D. Lincot, and J.-F. Guillemoles, "Microscale solar cells for high concentration on polycrystalline cu(in,ga)se2 thin films," *Applied Physics Letters*, vol. 98, p. 264102, June 2011.

APPENDIX A

Possibility of deducing internal radiative efficiency and photo-doping density

In order to check the validity of the data treatment, one can extract the non radiative and radiative efficiencies. It requires to write the particle balance equation Eq. (A).

$$J_{abs} = \alpha J_{laser} = J_{el} + J_r + J_{nr} \simeq J_r + \eta_{nr} J_{abs} \tag{A.1}$$
$$\text{with } \eta_{nr} = 1 - \eta_r = 1 - J_r/J_{abs} = 1 - \eta_{ext} J_{rout}/J_{abs}$$

As the sample was grown by molecular beam epitaxy and the luminescence comes from an intrinsic material, according to M.M Tashima *et.al* we expect a dominant non radiative efficiency.The experiment was perform at open circuit voltage so the electrical particle flux J_{el} can be eliminated. Thus the particle balance equation gets really simple and a internal radiative efficiency can be extracted. However, the ratio of the spatially and spectrally integrated PL over absorbed photons would give the external radiative efficiency. If one wants to get the radiative efficiency we need to take into account the emission geometry i.e. output efficiency. Indeed, as the set-up measures a Lambertian emission (solid angle of the objective already corrected by full calibration, see section 2.2.2) which results from an isotrope emission of photons inside the sample limited by an output solid angle. This output solid angle of hallf angle a/2 is given by the total reflection condition. This geometry is summed up in Fig. A.1. The external efficiency is given by the solid angle ratio in first

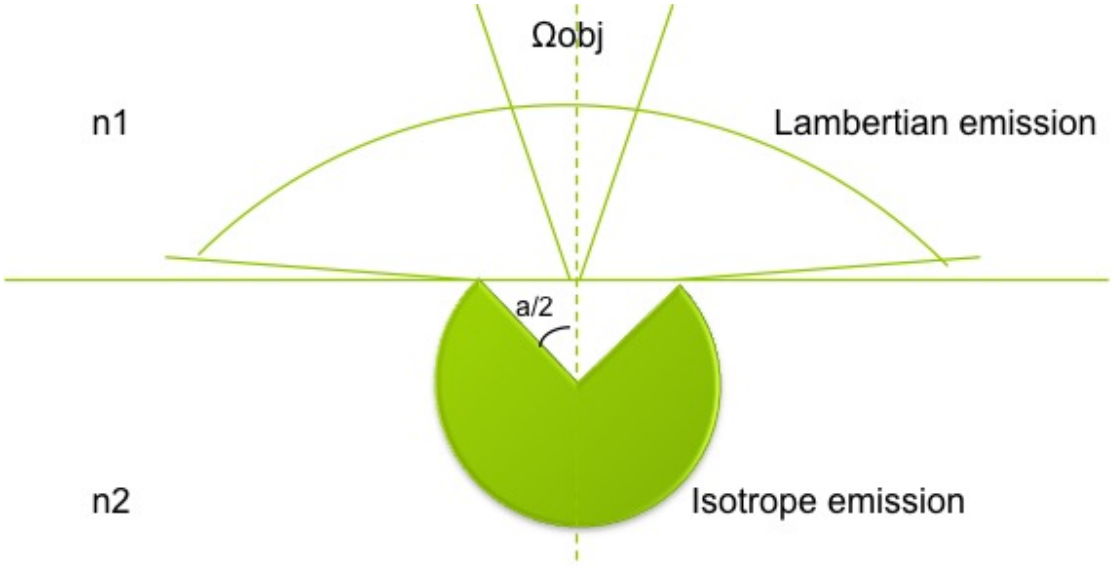


Figure A.1 – Geometric representation of the emitted PL signal from material n2 to the air n1

approximation. Then it follows A.

$$\eta_{rext} = \Omega_{out}/\Omega_{tot} = \frac{2\pi(1 - cos(a/2))}{4\pi} \quad \text{with } a/2 = \arcsin\left(\frac{n_1}{n_2}\right) \tag{A.2}$$

As the material refractive index fluctuates from 3 to 3.5 (see section 2.4.1) the output efficiency fluctuates between : 2 and 3%. The resulting internal radiative efficiency for different absorbed powers and a refractive index of 3 is plotted in Fig. A.2. Thus we get a quasi-linear growth with the power. Its value grows from 1 to 5% at high powers. The radiative efficiency seems relatively low, however the emission geometry approximation is a first approximation calculation which do not takes into account interferences and multilayer reflection. We can also extract the photo-doping concentration from the integrated PL intensity and the bimolecular recombination parameter, if we neglect the quantum effect in the wells and we consider all the photo-carriers recombines in the wells. Then we can write :

$$Bn^2 = \frac{\eta_{rext}}{t} \int I_{PL} d\lambda \tag{A.3}$$

With t the thickness of the recombinaison layer, n the carrier density and B the bimolecular recombination constant. Taking the maximum value obtained on the PL map in Fig. 3.1a of 5e22 $N_{ph}/s/m^2$, a 37 nm thickness, an output efficiency of

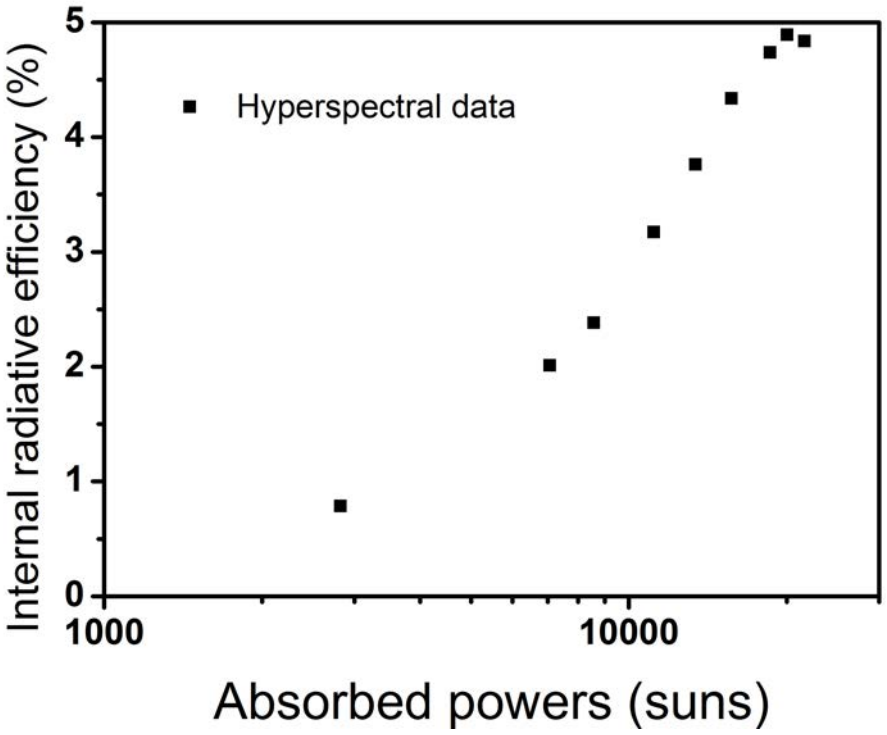


Figure A.2 – Internal radiative efficiency of the sample 2757 as function of absorbed powers

2% and a bimolecular recombination parameter of 2e16 m^3/s we get a maximum photo-carrier value of 6e17 cm^{-3}. The bimolecular constant is calculated for a bulk material considering the InGaAsP material. This value ensures that the population we study is not degenerated even considering one order of magnitude error. This section enables us to check the validity of the PL data treatment and to get order of magnitudes of photo-doping of 6e17 cm^{-3}, output efficiency of 2%-3% and a radiative efficiency with an absolute error of 0.5. Once we get the PL intensity data, we can extract the thermodynamic quantities.

APPENDIX B

Maximum local carrier temperature in the confocal system

If we want to get the central value of the temperature of emission instead of the average one i.e. illumination radius equal to collection radius, one can use in first approximation an empirical linear relation:

$$T_{local} = T_{conf} + C \times P_{abs} \tag{B.1}$$

using a constant value of 0.0025. Therefore, we get a calibrated centred temperature of emission Fig. B.1. As HI measurement are done at lower powers, one must be careful that the use of this relation is done considering a temperature dependence on power following its trend at higher powers. One can see the local temperature of emission gets very high reaching 1500 K at 130000 suns.

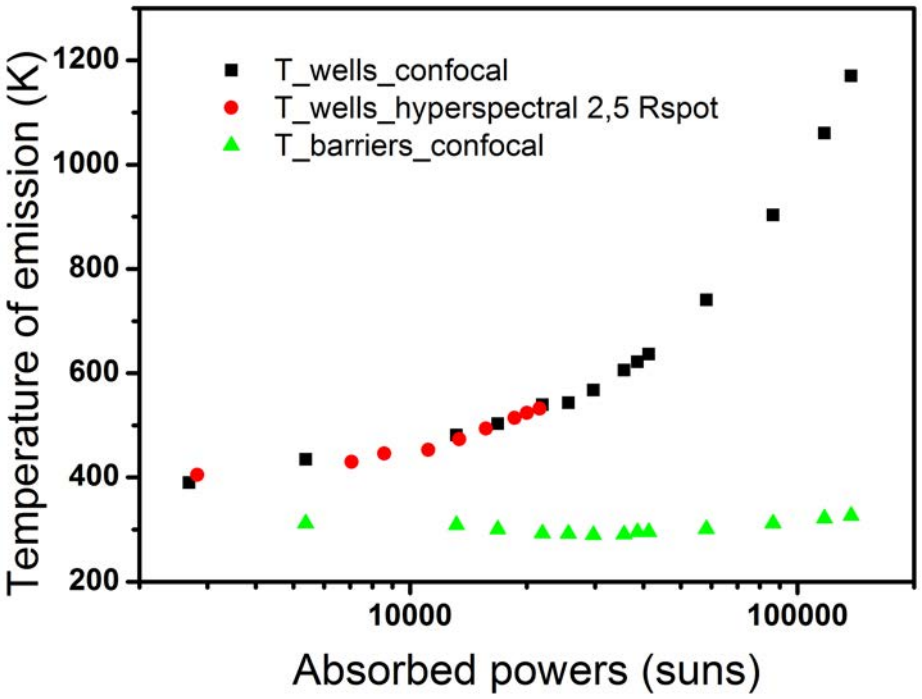


Figure B.1 – Local temperature of emission

APPENDIX C

Uncertainty calculation

In order to study the standard errors on the calculation of the thermodynamic quantities, we have developed a uncertainty calculation method based on differential analysis combined with composed relative uncertainties. As a reminder, standard errors are defined as the absolute error which includes 50% of the probed values surrounding the average value.

Differential analysis The first step is to write the equations of the thermodynamic quantities. Using Eq. (2.5) we can rewrite the temperature and the dm as following:

$$\Delta\mu = k_b T \left(ln(I_{PL}) - ln(A) - ln(E^2) \right) \tag{C.1}$$

$$T = \frac{\Delta\mu}{k_b ln\left(I_{PL}/(AE^2)\right)} \tag{C.2}$$

Using these equations, the measurement differentials will write as:

$$d\Delta\mu_m = \frac{\partial\Delta\mu}{\partial T}dT + \frac{\partial\Delta\mu}{\partial I_{PL}}dI_{PL} + \frac{\partial\Delta\mu}{\partial A}dA + \frac{\partial\Delta\mu}{\partial E}dE \tag{C.3}$$

$$dT_m = \frac{\partial T}{\partial\Delta\mu}d\Delta\mu + \frac{\partial T}{\partial I_{PL}}dI_{PL} + \frac{\partial T}{\partial A}dA + \frac{\partial T}{\partial E}dE \tag{C.4}$$

$$\tag{C.5}$$

The calculation of the differentials gives :

$$d\Delta\mu_m = k_b \left[ln\left(\frac{I_{PL}}{AE^2}\right) dT + T\left(\frac{dI_{PL}}{I_{PL}} - \frac{dA}{A} - \frac{2dE}{E}\right)\right] + dE \tag{C.6}$$

$$dT_m = \frac{1}{k_b ln(\frac{I_{PL}}{AE^2})}\left[d\Delta\mu - dE + \frac{(\Delta\mu - E)}{ln(\frac{I_{PL}}{AE^2})}\left[2\frac{dE}{E} + \left(\frac{dA}{A} - \frac{dI_{PL}}{I_{PL}}\right)\right]\right] \tag{C.7}$$

As the most important difference will be given by the sum of all the previous term, the equations become:

$$d\Delta\mu_m = k_b \left[ln\left(\frac{I_{PL}}{AE^2}\right) dT + T\left(\frac{dI_{PL}}{I_{PL}} + \frac{dA}{A} + \frac{2dE}{E}\right)\right] + dE \tag{C.8}$$

$$dT_m = \frac{1}{k_b ln(\frac{I_{PL}}{AE^2})}\left[d\Delta\mu + dE + \frac{(\Delta\mu + E)}{ln(\frac{I_{PL}}{AE^2})}\left[2\frac{dE}{E} + \left(\frac{dA}{A} + \frac{dI_{PL}}{I_{PL}}\right)\right]\right] \tag{C.9}$$

We have seen each quantity are fitted thanks to the Eq. (2.5) and all fitting tools (Matlab, Origin) gives the standard errors of the calculated coefficients (da and db). However, we want to get the standard errors of the thermodynamic quantity therefore using the same differential analysis we get:

$$dT = d(-\frac{1}{k_b a}) = -\frac{1}{k_b}\frac{\partial T}{\partial a}da = \frac{1}{k_b a^2}da \tag{C.10}$$

$$d\Delta\mu = k_b d(T \times b) = k_b(\frac{\partial \Delta\mu}{\partial T}dT + \frac{\partial \Delta\mu}{\partial b}db = k_b(bdT + Tdb) \tag{C.11}$$

Each fitting standard errors above will be reintroduced in Eq. (C.9) in order to calculate the measurement errors. All the other quantities such as E, I_PL, A are averaged on the fitting range. The relative uncertainty dI_{PL}/I_{PL}, and dA/A are taken as 5% and 50%.

Relative composed uncertainty The next step is to get the global relative uncertainty of each quantities including both measurements and fitting errors. Therefore we can used the composed uncertainty u_c which writes as:

$$u_c(\Delta\mu) = \sqrt{u_m^2 + u_f^2} = \sqrt{(\frac{d\Delta\mu_m}{\Delta\mu_m}^2) + (\frac{d\Delta\mu}{\Delta\mu})^2} \tag{C.12}$$

$$u_c(T) = \sqrt{u_m^2 + u_f^2} = \sqrt{(\frac{dT_m}{T_m}^2) + (\frac{dT}{T}^2)} \tag{C.13}$$

At last, error bars are just the product of the thermodynamic quantities and its composed uncertainty. One as too keep in mind the differential analysis is a pessimist case as all the errors are added. However, it makes sure of the reliability of the measurements.

Abstracts

Résumé

La cellule photovoltaïque à porteurs chauds est un dispositif de conversion de l'énergie solaire en énergie électrique dont les rendements théoriques approchent les 86%. Additionnellement à une cellule photovoltaïque standard, ce dispositif permet de convertir l'excédent d'énergie cinétique des porteurs photogénérés, en énergie électrique. Pour cela, le phénomène de thermalisation doit être réduit et des contacts électriques sélectifs en énergie ajoutés.

Afin de déterminer les performances potentielles des absorbeurs, tout en surmontant le défi de fabrication des contacts électriques sélectifs, un montage et une méthode de cartographie d'intensité absolue de photoluminescence résolue spectralement ont été utilisés. Ceci a permis d'obtenir la température d'émission et la séparation des quasi-niveaux de Fermi, les deux grandeurs thermodynamiques caractéristiques de la performance des absorbeurs. Dans cette étude, des absorbeurs à base de puits quantiques d'InGaAsP sur substrat d'InP sont utilisés.

Les grandeurs thermodynamiques sont estimées et la technique de caractérisation utilisée permet l'accès à des grandeurs tel que le facteur de thermalisation mais aussi un coefficient thermoélectrique, appelé photo-Seebeck. L'analyse quantitative de porteurs chauds dans des conditions pertinentes pour le photovoltaïque est une première ; le dispositif étudié permettrait de dépasser la limite de Schockley-Queisser.

Enfin, le dispositif étant muni de contacts des caractérisations électriques sont faites et comparé aux mesures optiques. Afin de mieux comprendre l'évolution des grandeurs thermodynamiques étudiées, une première simulation est proposée.

Mots-clefs

Effet photovoltaïque, Porteurs chauds, Luminescence, Imageur hyperspectral, Quasi-niveaux de Fermi, Effet Seebeck

Abstract

The hot carrier solar cell is an energy conversion device where theoretical conversion efficiencies reach almost 86%. Additionally to a standard photovoltaic cell, the device allows the conversion of kinetic energy excess of photogenerated carriers into electrical energy. To achieve this, the thermalisation process must be limited and electrical energy selective contacts added.
In order to determine potential absorber performances and overcome the fabrication challenge of energy selective contacts, a set-up and the related method of mapping absolute photoluminescence spectra were used. This technique allows getting quasi-Fermi levels splitting and temperature of emission, both thermodynamic quantities characteristic of the performance of the absorbers. In this study, absorbers based on InGaAsP multi-quantum wells on InP substrate were used.
The thermodynamic quantities are determined and allow to access at quantities such as thermalisation rate but also a thermoelectric coefficient, so-called Photo-Seebeck. The quantitative analysis of the hot carriers regime, in relevant conditions for photovoltaic is a first: the analysed device indicates a potential photovoltaic conversion over the Schockley-Queisser limit.
At last, as the device is supplied with electrical contacts, electrical characterization are made and compared to optical measurements. A first simulation is proposed to better understand the thermodynamic quantities evolution as a function of the electrical bias.

Keywords

Photovoltaic effect, Hot carrier, Luminescence, Hyperspectral imager, Quasi-Fermi levels, Seebeck effect